THE ASTROPHYSICAL JOURNAL SUPPLEMENT SERIES, 127:79–124, 2000 March

A BATSE EARTH-OCCULTATION CATALOG OF 0.03–1.8 MeV GAMMA-RAY SOURCE SPECTRA AND LIGHT CURVES FOR PHASES 1–3 (1991–1994)

J. C. LING,[1] WM. A. WHEATON,[2] P. WALLYN,[3] R. T. SKELTON,[4] WM. A. MAHONEY, R. G. RADOCINSKI, J. L. CALLAS, N. F. LING,[5] AND E. TUMER[6]
Jet Propulsion Laboratory, California Institute of Technology, Pasadena, CA 91109

AND

R. SHUBERT
Institute for Fundamental Sciences, Irvine, CA
Received 1997 March 7; accepted 1999 September 17

ABSTRACT

Using the powerful Earth-occultation technique, long-term, nearly continuous monitoring of the entire low-energy gamma-ray sky is now possible with the advent of BATSE, the Burst and Transient Source Experiment on board the *Compton Gamma Ray Observatory* (*CGRO*). In this paper, we present a catalog of 34 moderately strong gamma-ray sources measured by BATSE. It consists of 0.03–1.8 MeV photon spectra averaged over weeks and months, and light curves of the 35–200 keV flux, with 1 day resolution, covering the first three phases of the *CGRO* mission (1991 May through 1994 October). These results have been obtained using the JPL Enhanced BATSE Occultation Package (EBOP) developed under the *CGRO* Guest Investigator Program. The EBOP concept and approach are also described in some depth. This paper presents highlights extracted from a large EBOP database which has now been archived at the Compton Observatory Science Support Center (COSSC). This database contains a complete record of ~1200 daily source count rates in 14 energy channels along with the corresponding Poisson and systematic errors for 64 sources, including 30 not described here. An interface to XSPEC is included in the archive allowing conversion from count rates to photon fluxes. This paper therefore serves also as a reference and entree into the archive and provides an index and guide for those investigators using the EBOP system and database for their respective scientific investigations.

Subject headings: catalogs — gamma rays: observations

1. INTRODUCTION

Since the birth of low-energy gamma-ray astronomy (10 keV–10 MeV) in the mid 1960s, the field has advanced from an exploratory science to one of the prominent branches of astrophysics. Today we know the gamma-ray sky is highly variable, featuring a wide variety of phenomena such as gamma-ray bursts, solar flares, as well as episodic variations from known sources. We have now seen a fairly large population of cosmic X-ray and gamma-ray sources (Fichtel et al. 1994; Schönfelder et al. 1999; Macomb & Gehrels 1999), including pulsars, black hole (BH) candidates, accreting binary neutron stars, as well as active galactic nuclei (AGNs), showing complex spectral and flux variability that are not well understood. Because of the ubiquitous irregular behavior of gamma-ray sources in general, many of the interesting results obtained in the past have either not been confirmed or have been misinterpreted in the context of a long-term overview of their behavior when only spotty and isolated observations can be made. In order to break this impasse, a sensitive continuous all-sky monitoring capability is needed to guide the search and to provide a continuous homogeneous record of variability. Such a capability did not exist prior to the launch of the *Compton Gamma Ray Observatory* (*CGRO*). There was also no uniform sky survey of gamma-ray sources at a flux level much below 10% of that of Crab and Cygnus X-1 at 100 keV. The most complete hard X-ray catalog based on data from a single experiment to date is the *HEAO 1* A-4 catalog (Levine et al. 1984). It contains 75 sources in the 13–180 keV region, in four broad energy bands. In the highest energy 80–180 keV channel, however, only 14 sources were detected, due to relatively thin (3.8 mm NaI) detectors. Furthermore, data included were limited to only fluxes sampled every 6 months with little information on variability on a shorter timescale.

The eight Large Area Detectors (LADs) of the Burst and Transient Source Experiment (BATSE) (Fishman et al. 1989) are ideally suited for sensitive and nearly uninterrupted monitoring of cosmic sources in the 35 keV–1.8 MeV range using Earth as an occulter for modulating the source signals. From 1992 to 1997, the Jet Propulsion Laboratory (JPL) High Energy Astrophysics Group was supported under the *CGRO* Guest Investigator Program, in collaboration with the BATSE team at the Marshall Space Flight Center (MSFC), for the development of an end-to-end Enhanced BATSE Occultation Package (EBOP) (Ling et al. 1996) for monitoring the 64 gamma-ray sources in the EBOP input catalog (see Table 1). We have now completed the processing of ~1200 days of data using EBOP covering the first three phases of the mission between 1991 May 17 [TJD 8393 where TJD (Truncated Julian Day) = JD (Julian Day) −2,440,000.5] and 1994 October 3 (TJD 9628). Daily

[1] Present Address: Code SR, NASA Headquarters, Washington, DC 20546.
[2] Present Address: Infrared Processing and Analysis Center, Caltech, 100-22, Pasadena, CA 91125.
[3] Present Address: 39 Rue de L'Hotel de Ville 59240, Dunkerque, France.
[4] Present Address: University of California-San Diego, CASS, 0111, 9500 Gilman Drive, La Jolla, CA 92093-0111.
[5] Present Address: Freddie Mac, McLean, VA 22102.
[6] Present Address: Physics Department, University of California San Diego, La Jolla, CA 92093-0111.

TABLE 1

A List of Sources Presently Included in the EBOP Input Source Catalog

Number	Source	R.A.	Decl.	SI[a]	Number	Source	R.A.	Decl.	SI[a]
1	1E 1024−57	156.49	−57.81	W†	33	GRS 1009−45	153.40	−45.08	W**
2	1E 1740−29	265.98	−29.72	I	34	GRS 1758−258	270.30	25.74	W*
3	2CG 135+18	37.81	61.20	W†	35	GRS 1915+105	288.82	10.97	I
4	3C 273	187.28	2.05	W**	36	GS 2023+338	306.02	33.87	W†
5	3C 279	194.05	−5.79	H†	37	GX 1+4	263.01	−24.75	W**
6	4U 0115+634	19.63	63.74	W†	38	GX 301−2	186.66	62.77	W**
7	4U 1145−61	176.99	−62.21	W†	39	GX 312−1	215.30	−62.70	W**
8	4U 1543−45	236.79	−47.67	W**	40	GX 339−4	255.71	48.79	W*
9	4U 1608−522	243.18	−52.42	W*	41	GX 354+0	263.00	33.84	W*
10	4U 1627−673	248.07	−67.46	W†	42	HD 32918	74.58	−75.28	W†
11	4U 1700−37	255.99	−37.84	I	43	Her X-1	254.46	35.34	W**
12	A0535+262	84.73	26.32	W†	44	HR 1099	54.20	0.59	W**
13	A0620−00	95.69	−0.35	W†	45	M51	202.47	47.20	W†
14	A1118−616	170.24	−61.92	W†	46	M82	148.97	69.68	W†
15	Aquila X-1	287.82	0.58	W*	47	MCG 8-11-11	88.72	46.43	H†
16	ARLACERT	332.17	45.74	W†	48	MRK 421	166.11	38.21	W†
17	ASM 2000+25	300.53	25.14	W†	49	NGC 1275	49.95	41.51	W**
18	Cen_A	201.47	−42.97	I	50	NGC 253	11.88	−25.29	W†
19	Cen X-3	170.31	−60.62	W†	51	NGC 4151	182.60	39.51	W**
20	Cir X-1	230.17	−57.17	W**	52	NGC 5548	214.50	25.13	W†
21	CRAB	83.63	22.01	S	53	NOVA CYG	307.63	52.63	W†
22	Cyg X-1	299.59	35.20	S	54	NOVA MUSCAE	171.61	−68.68	W†
23	Cyg X-2	326.17	38.32	W†	55	NOVA SAG	272.74	−32.22	W**
24	Cyg X-3	308.11	40.96	W*	56	OAO 1657−415	255.20	−41.67	W*
25	EXO 1846−31	282.30	−3.10	W**	57	PKS 2155−30	329.72	−30.23	W†
26	EXO 2030+375	308.06	37.64	W†	58	PSR 1259−63	195.70	−63.84	W**
27	GEMINGA	98.48	17.77	H†	59	PSR 1509−58	228.48	−59.14	W**
28	GRO J0422+32	65.43	32.91	I	60	SCO X-1	244.98	−15.64	W*
29	GRO J1008−57	152.44	−58.27	W†	61	SCT X-1	279.18	−7.58	W*
30	GRO J1655−40	253.50	−39.85	W†	62	SMC X-1	19.27	−73.44	W†
31	GRO J1719−24	259.93	−25.01	W*	63	Vela X-1	135.53	−40.55	I
32	GRS 0834−430	129.16	−43.26	W**	64	WR 140	305.12	43.85	W†

[a] Source Index (SI): W = weak sources. W* = 35–200 keV flux is between 50 and 90 mCrab averaged over 1200 day period. W** = 35–200 keV flux is between 20 and 50 mCrab averaged over 1200 day period. W† = 35–200 keV flux is less than 20 mCrab averaged over 1200 day period. (Note: 1 Crab unit of the 35–200 keV flux = 1×10^{-3} photons cm^{-2} s^{-1} keV^{-1}.) I = intermediate sources: 35–200 keV flux is between 90 and 500 mCrab averaged over 1200 day period. S = strong sources: 35–200 keV flux is greater than 500 mCrab averaged over 1200 day period. H† = high-energy sources. The 35–200 keV flux, however, is less than 20 mCrab averaged over 1200 day period.

count rates of the 64 sources in 14 energy channels and their Poisson and systematic uncertainties measured typically by 2–4 LADs per source, representing a total of ∼150,000 spectra, are now archived at the Compton Observatory Science Support Center (COSSC) at the Goddard Space Flight Center (GSFC), as well as at MSFC and JPL, making them available to the community.

This BATSE catalog significantly extends the source information presented in the *HEAO 1* A-4 catalog (Levine et al. 1984) by focusing on 34 of the stronger sources (indicated as either W*, W**, I, or S in Table 1) which have an average 35–200 keV flux over the 1200 day period of ≥20 mCrab. Thirty-three of 34 sources have shown positive flux (>80 keV), compared to 14 observed by *HEAO 1* A-4. Fluxes up to 1 MeV have also been detected in 17 of the 34 sources. This catalog is also the first to present high-resolution light curves (1 day) along with 14 channel spectra, that span more than 3 years. The primary objectives for producing such a catalog are to: (1) release these results to the community in a format which is useful to support a wide variety of research, (2) serve as an entree to the larger JPL EBOP database, (3) serve as a reference for comparison with results obtained by different instruments, and (4) provide a detailed description of the end-to-end EBOP analysis method. The latter will allow users to independently process the BATSE Earth-occultation data and to assess the EBOP approach. Because there has been a general lack of detailed publications on analysis methods for different gamma-ray experiments in the past, it has often been difficult to assess the quality of these results.

Section 2 describes the BATSE instrument and details the JPL EBOP method. The main results in § 3 are divided into two subsections: (a) light curves of the 35–200 keV flux for each of the 34 sources covering the 1200 day period between 1991 May and 1994 October, and (b) spectra for each of the 34 sources averaged over three separate 400 day periods, as well as shorter averages for selected sources.

2. BATSE EARTH-OCCULTATION OBSERVATIONS AND ANALYSIS

In this section we describe the details of the methods used to produce results in this catalog. Experiments in the low-energy gamma-ray region are plagued by numerous well-known difficulties, with which observers have struggled for many years. Above ∼10 keV the optical elements, lenses, and mirrors available in most astronomy cease to be effective, yet below a few tens of MeV the event identification techniques of high-energy physics (based, for example, on multidetector coincidences and event topology, such as the "V" events due to pair-production in spark chambers)

become progressively more problematic. At the same time, source fluxes almost invariably decrease rapidly with increasing energy, while the background is large, complex, and variable (cf. Fig. 1).

As Figure 1 suggests, the background in low-Earth orbit includes at the least: components due to the true cosmic diffuse background; components due to prompt effects related to cosmic ray interactions in the spacecraft, instrument, and Earth's atmosphere; components due to prompt and long-term activation of numerous species, both from cosmic rays and from passages through the South Atlantic anomaly; and components due to the effects of cosmic sources, constant and variable, known and undiscovered, point and diffuse. Because the response properties of gamma-ray telescopes are generally far from ideal, even for shielded instruments, there are important effects from, e.g., Compton scattering of source fluxes in the instrument, spacecraft, and atmosphere, the finite transmission of shields, and the like. Almost all these effects vary importantly with time, instrument orientation in space, spacecraft position in orbit, and the visibility and temporal behavior of strong sources. Experience has shown that in these circumstances many attractive shortcuts and simplifications, which one might reasonably attempt, lead to problems in the end which limit the sensitivity of the analysis well short of what ought to be the ultimate statistically possible.

From 1980 to 1997, the JPL group has developed a characteristic approach to dealing with these issues, originally motivated by the analysis problems encountered in the *HEAO 3* High-Resolution Spectroscopy experiment (Mahoney, Ling, & Jacobson 1981; Wheaton et al. 1995). The central idea of the methodology is based on the fact that, whatever their complexities or limitations, low-energy gamma-ray instruments, operating as they do one count at a time, are at least highly linear devices in the sense that their output count rates are normally sums of the independent effects of their input flux components, however numerous and complex those components may be. If an instrument is to effectively separate cosmic sources of astronomical interest from the other effects contributing to its total count rate, it must clearly respond in a distinctly different way to each. These characteristic "ways of responding" are mathematically vectors, and the analysis problem, in the JPL approach, then becomes a question of, first, computing response vectors for astronomical sources and for background effects accurately and efficiently, and second, effectively separating them by the techniques of linear algebra, particularly the linear least squares methodology of classical statistics, adapted to the peculiar requirements of the Poisson statistics.

This general approach (described by Mahoney et al. 1984, Wheaton et al. 1989, and Wheaton et al. 1995), though

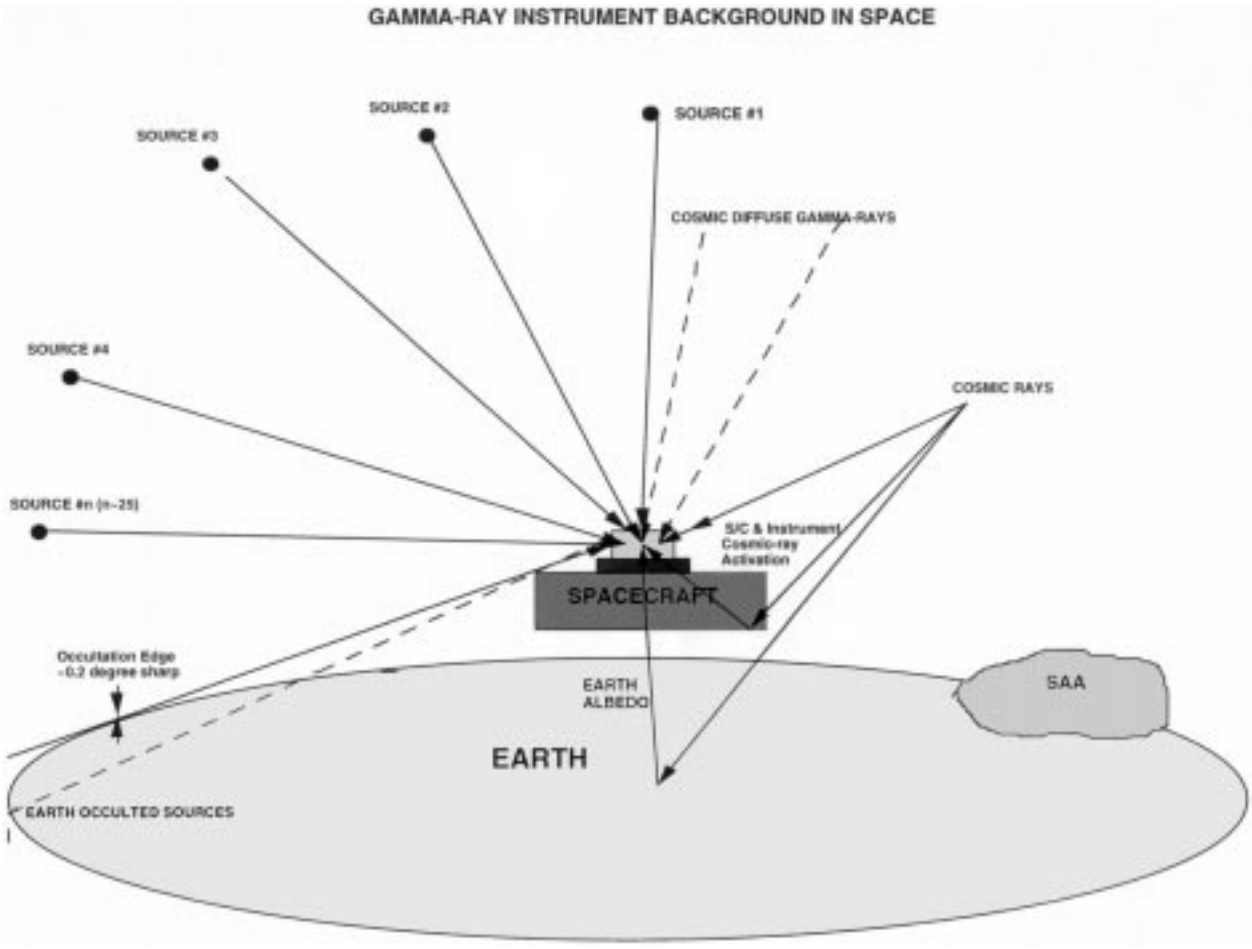

FIG. 1.—Complexity of low-energy gamma-ray measurements. The effective background for each source includes substantial effects due to numerous other cosmic sources and backgrounds. The combination of strong source and background variability, and the absence of any truly adequate means of chopping low-energy gamma-rays, implies the ultimate necessity of self-consistently decomposing the total count rate, and of detailed physical modeling of its components, which comprise the core of EBOP.

somewhat limited by the capabilities of the computers available at the time of the *HEAO 3* analysis, still allowed the discovery of ^{26}Al in the interstellar medium (Mahoney et al. 1984), and more recently a high-resolution observation of the spectrum of the cosmic background (Wheaton et al. 1996). With the advent of modern workstations and software for numerical linear algebra, least squares Poisson estimation can be used effectively for problems of a size and complexity unthinkable a few years earlier. The overall success of the JPL EBOP method is indicated by the general consistency of cosmic source fluxes measured by the various LADs, as discussed in § 2.6, and the consistency of source spectra integrated over several 400 day periods as shown by the averaged spectra in § 3 (e.g., Fig. 8, panel 11).

There remain the details of computing responses to cosmic sources and the various background contributions. The fact that gamma rays are highly penetrating means that in general instrument responses really need to be known, at least approximately, even far off the nominal viewing axis, and the aggregate contribution of point and diffuse sources is an important component of the background, even for collimated instruments. Because the background is so large (often 100 times the sources of interest) and complex, we are always forced to use approximate models that are normalized component-by-component to fit the data as well as possible. Nevertheless, it is our opinion that it is worthwhile to incorporate as much of the background and detector physics as we can into the response vectors, for reasons discussed in § 2.3.

Section 2.1 describes the BATSE instrument and data, § 2.2 discusses the Earth-occultation method in general, § 2.3 details the linear Earth-occultation model, § 2.4 discusses systematic errors, § 2.5 describes the estimation of physical fluxes from count rates using the standard spectral analysis program XSPEC, § 2.6 discusses the LADs consistency test, and § 2.7 gives a description of the data products now archived at the COSSC.

2.1. *The BATSE Experiment*

BATSE (Fishman et al. 1989) includes eight Large Area NaI scintillator Detectors (LADs), each 50.8 cm diameter × 1.25 cm thick (∼2025 cm^2 geometrical area) operating in the energy range 0.02–1.8 MeV. The eight LADs look out from the corners of the spacecraft such that their surfaces are in the faces of a regular octahedron, providing a near-isotropic response to the ∼2/3 of the sky that is not occulted by Earth at any moment. Each LAD has a plastic scintillator anticoincidence shield for reducing the background due to charged particle events. Results presented in this catalog are based on the "CONT" (continuous) data (Harmon et al. 1992, 1996) in which counts from each LAD are accumulated in 16 broad energy channels and read out every 2.048 s, independent of gamma-ray burst triggers. Energy edges of the CONT channels are determined, first, by the gain of the LADs, their linear electronics, and the analog-to-digital (A/D) converters that make up the 128-channel pulse height analyzer (PHA) systems; and second, by the mapping from the PHAs to CONT channels. This mapping is defined in a table aboard the experiment and is subject to occasional commanded changes. The analysis also makes use of data from the BATSE Spectroscopy Detectors (SDs), eight unshielded 12.7 cm diameter × 7.62 cm thick NaI crystals, located near the LADs, to monitor the local cosmic-ray (CR) environment, as described in § 2.3 below. For most of the period of interest here, the oppositely pointed SDs were operated in pairs with matching gains. The gain of one pair was set low, so that the upper level discriminators (ULDs) were approximately 55 MeV. A second pair had its ULDs set at ∼22 MeV, and the two remaining pairs were set to high gain, so that their ULDs were ∼5.5 MeV.

2.2. *The Earth-Occultation Method*

The Earth-occultation method is conceptually simple. The Earth is entirely opaque to gamma rays. The limb of the Earth is fairly sharp, nearly independent of energy. The *e*-fold in air mass is about 7.5 km in graze height, or 0.°2 in angle at the distance from BATSE to the horizon. When a strong source sets, it will drop from full brightness to zero within a few seconds, producing a downward step in the count rate history clearly distinguishable from background variations (Fig. 2). Similarly, an upward step appears when the source rises. For an experiment in low Earth orbit (LEO), there are typically 16 orbits per day, or a total of 32 potentially observable steps for a given source. The count rate associated with a source is derived from the step amplitude. (In principle the position of the source can also be derived from the times of the rising and falling steps, although we have not done that in the analysis reported here.) Note that usually the projection of the limb of the Earth, as the source rises, traces a different arc on the sky than it does when the source sets. During the course of one orbit, Earth from LEO subtends a half angle of about 70°, and therefore at any given time, sources within about 20° of the normal to the orbital plane will not be occulted. However, as the orbit plane precesses, with a ∼50 day period for the *CGRO* orbit, the regions in the sky that are not occulted slowly circle the celestial poles, such that the entire sky can be observed during each cycle. BATSE is thus the first truly effective gamma-ray all sky monitor flown in space.

The JPL Earth-Occultation Analysis system (Skelton et al. 1994; Ling et al. 1996) consists of two large parts, (a) the linear Earth-occultation model analysis (detailed in § 2.3), which estimates count rates and uncertainties for cosmic sources in each LAD and each energy channel, and (b) the spectral analysis section, including the interface to XSPEC (which converts from instrument units [count rates] to physical units [photon fluxes] using the LAD response

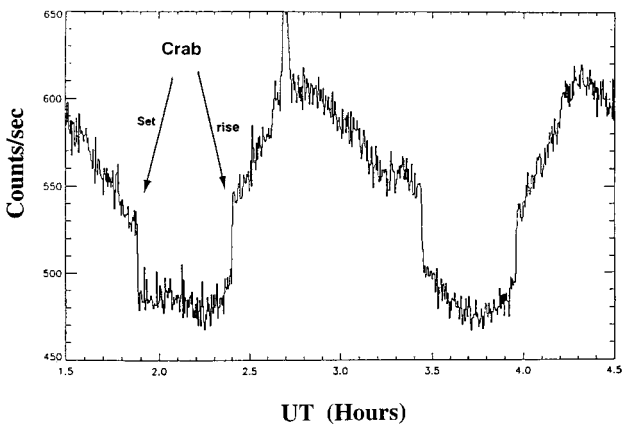

FIG. 2.—When a strong source is occulted by the Earth, it will drop from full brightness to zero within a few seconds, producing a downward step in the count rate history clearly distinguishable from the background variations. Similarly, an upward step appears when the source rises.

matrix; Pendleton et al. 1995), XSPEC itself, and MULPLOT, a package for displaying and manipulating the output. Figure 3 shows a flow diagram of the EBOP system (Ling et al. 1996). First, a magnetic tape containing the raw count data in the 16 CONT energy channels from each of the eight LADs and also in four high-energy discriminators from each of the eight SDs, all with 2.048 s resolution, plus housekeeping and quality data files, was sent to us by the Principal Investigator team at MSFC (step 1). These data were then merged and reformatted (Step 2) to 16.384 s resolution for subsequent processing. The P. I. team also provided us with a program to compute the response matrix for each of the eight LADs as a function of energy and angle with respect to the look axis of the detector. BATSE Earth-occultation data were organized by *CGRO* viewing period (VP, nominally 14 days), during which the spacecraft's orientation in inertial space was held fixed. For each VP, the detector's response matrix to the cosmic source was first computed (step 3) and then converted to a format compatible with XSPEC (step 9). The heart of the EBOP system is step 4, which fits 1 day stretches of data to a physical model, linear in the (typically 45–75) unknowns, independently for each CONT energy channel and each LAD. Of these unknowns, 10–35 are count rates due to cosmic point sources, and the remainder (typically ~ 35) are due to background terms in the model. The results obtained are daily count rates and uncertainties, for each cosmic source (and background term), for each energy, and for each detector. The remainder of the EBOP system includes procedures to estimate the systematic uncertainties associated with the source count rates (step 6); routines associated with the spectral analysis program XSPEC, which converts source count rates to photon fluxes (steps 7, 8 10, and 11); and utility programs to display and manipulate results, leading to flux histories and time-average spectra such as those shown in this catalog (steps 12 and 13).

2.3. *Linear Model Analysis*

Earth-occultation analysis may be approached in various ways. An important distinction is between methods (sometimes called "superposition") which accumulate the data first and then subtract the background, and alternative methods which operate in essentially the reverse order. The former accumulate many orbits of data into a data array modulo the orbital period, so as to align the source rise/set edges, until sufficient data are superposed to give significant results. They then subtract the background, e.g., by a polynomial fit. The latter methods subtract the background first (again typically by a model fit) and then accumulate the net (i.e., background-subtracted) source count rate estimates (which may be individually of very low statistical significance) to build up significant results. The first class of methods seems natural and attractive and was historically used by early experimenters with the occultation method, but we have previously given compelling reasons for preferring the second approach (Wheaton et al. 1989; Wheaton et al. 1995). The reason that the accumulate and subtract operations do not commute is essentially that, for small signals riding on top of a large and strongly variable background, the gaps and data cuts that are always present and necessary in real data will introduce into the accumulations a very large source of noise that typically swamps the signal, unless the processing order is as described. Both our EBOP system and the "Mission Operations" (MOPS; Harmon et al. 1992) system developed by the P. I. team at MSFC are of this same general type.

There are, however, important differences between the EBOP and the MOPS systems. First, the JPL system does a separate fit to each LAD. Since the *CGRO* maintains a fixed orientation in inertial space during each VP, the count rate for a given source with a constant flux generally differs from LAD to LAD, but remains constant during a VP. In the EBOP analysis, count rate estimates are made for any given source independently, for each LAD that has a significant response to it. The differing count rates are later combined to estimate a single physical photon flux for the source using XSPEC (Arnaud 1996), with the response matrices appropriate for each LAD in the direction of the source. The MOPS system, which was especially designed to allow near real-time monitoring of source flaring and variability, by contrast takes a weighted sum of the counts from different LADs, with weights chosen according to the expected response to a particular source, and then performs a single fit to the sum. The EBOP approach is intended to give improved results for the analysis of spectra and the calculation of source fluxes. (A second occultation analysis system was later developed at MSFC to fit the individual

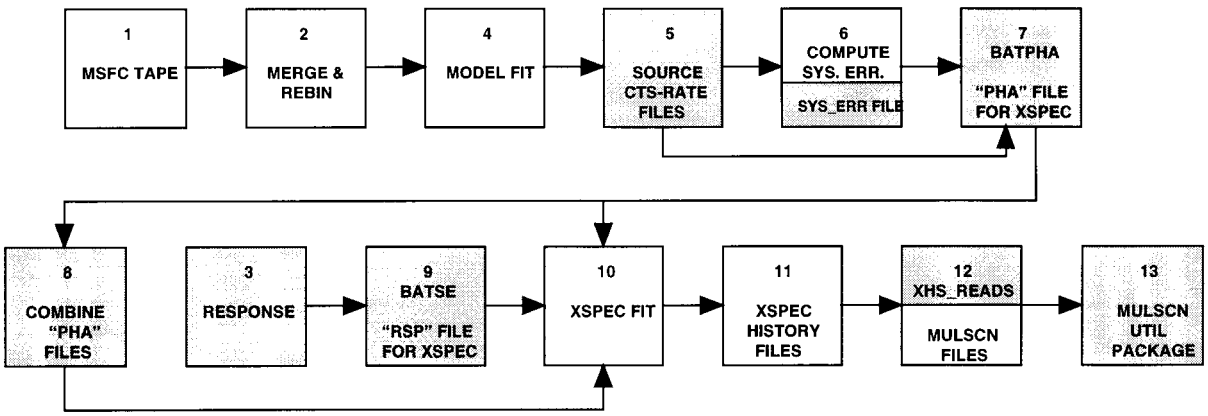

FIG. 3—An end-to-end flow diagram of the EBOP system developed by the JPL team. The shaded boxes correspond to data files and programs delivered to the Compton Observatory Science Support Center and MSFC.

LADs separately, more similar in this regard to EBOP; A. Harmon et al. 1996, private communication). An advantage of EBOP's separate fits to each LAD is that it is possible to compare results from different LADs for consistency with a unique physical source flux and thus detect certain kinds of internal problems in the analysis.

A second difference is that EBOP uses a fairly elaborate multiparameter physical model for the detector background, allowing fits to a longer stretch of data (currently 1 day) whereas the MOPS system uses a simple quadratic model for the background and fits to a much shorter interval, about 2 minutes on each side of the source rise or set. Each approach has its own advantages and disadvantages.

Of course a physical model for the noncosmic background yields a more accurate background subtraction for a given number of terms, if the model is reasonably accurate. The more important consideration for EBOP was that it achieves this accuracy without the associated loss of statistical sensitivity that approximation of the background by an expansion in a mathematically complete set of basis functions necessarily incurs as terms are added, thereby making it practical to use many more terms. The reason is that, since a complete basis can fit any reasonable function, it can model not only the detector background variations, but the cosmic source templates as well. As additional terms are added to the background model, the mathematical overlap with the source templates becomes larger and larger, leading to an unlimited loss of sensitivity. More precisely, since the space $\{I_b\}$ of the physical background data is linearly independent of the space $\{I_c\}$ of possible count rates due to the numbers of discrete cosmic sources of interest here, (notice that if this fact were not true in practice, any method of Earth-occultation analysis would be doomed to fail), an accurate physical model will be able to approximate the background very well without such a serious loss of sensitivity for cosmic sources.

A second, related, advantage is that an accurate detector background model enables us to fit to intervals of data long enough that it is possible to treat both the rise and set edges of each source in one fit. Analyzing occultation edges one-at-a-time effectively projects the two-dimensional distribution of sources in the sky onto the one-dimensional limb of the Earth. Since the fundamental spatial resolution of the occultation method (given by the $\sim 0.^{\circ}2$ sharpness of the limb of the Earth) and the associated statistical errors permit a very large number (ultimately hundreds, we believe) of sources to be considered, preserving the second dimension by analyzing both rise and set edges together is an important strategic consideration. Since unmodeled point sources are one of the major causes of systematic error, the inclusion of weaker sources in the model is essential for high-accuracy measurements; yet this cannot be done if source confusion is too severe. Fortunately, sources that are confused at either a rise or a set are not likely to be confused at both. Thus, we are able to analyze sources effectively in confused regions such as the Galactic center as long as they are not aligned simultaneously along rise and set edges for that day.

2.3.1. *Approach*

The data analysis approach is based on multiparameter linear least squares (LLSQ) fits to remove variable background effects from accumulations of data. A linear model for the observed counts n_i in time bins $i = 1, \ldots, I$ is developed with J terms, including both cosmic sources and uninteresting background effects. The analysis follows the general LLSQ scheme described, e.g., by Wheaton et al. (1995), whose terminology and notation we follow here. The expected counts $\tilde{n}_i$ in each time bin i, are ascribed to a sum of J terms

$$\tilde{n}_i = \sum_j A_{ij} r_j ,$$

where $j = 1, \ldots, J$, some of which are associated with various background mechanisms, and some of which are due to cosmic sources. Each term j includes a known function $A_j(t_i) \equiv A_{ij}$, or template which describes the relative behavior of that term in time, and an unknown factor r_j, estimated from the fit, which gives the amplitude of the given template in the observed data n_i. The template vector A_j is the jth column of the LLSQ matrix A_{ij}. For example, the template for a given cosmic gamma-ray source would be 1.0 when the source is well above the horizon, 0.0 when it is fully blocked, and would change in a few seconds between 0 and 1 at rises or sets, following the atmospheric absorption near the limb.

For the present results with a bin size of 16.384 s per bin, we have a maximum of 5274 bins per day (typically $I \sim 4300$, accounting for gaps), with $J = \sim 45$ to 72 unknowns. Thus, we solve a LLSQ problem of around (4300 × 70) for each energy channel $k = 0, \ldots, 15$ and each LAD $n = 0, \ldots, 7$ for each day of BATSE data. Figure 4 shows a ~ 2 hr stretch of data with the best-fit model overlaid.

2.3.2. *Source Model*

Because of the large size of the LADs, an error of even 1–2 s in the position of the source edge produces a significant effect in just a single rise or set for a strong source such as the Crab.

Thus, for the cosmic source template A_c, the calculation of the limb profile takes account of the oblateness of Earth, and also of the variation in its effective size with energy E:

$$A_c(i) = \exp\left[-\mu(E_i)x_i\right] ,$$

x_i being the air mass (g cm^{-2}) in bin i, and $\mu(E_i)$ the gamma-ray absorption coefficient at energy E_i. As most of the

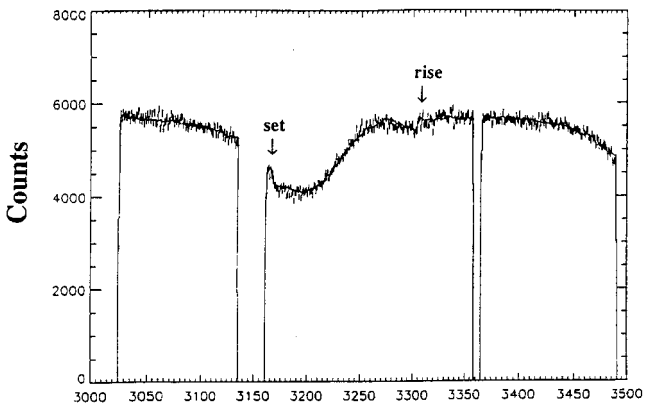

FIG. 4.—Overlay of model (*solid histogram*) and data (*error bars*) for the $k = 6$th (94–120 keV) energy channel. Note set and rise of the Crab Nebula at ~ 3165 and ~ 3305, respectively.

change in A_c occurs in a single 16 s time bin, we compute the bin average atmospheric transmission by integrating $A_c(t)$ over the bin.

Because the calibration of the LADs is not accurately known for large angles ϑ from the LAD look-axis, it is not now possible to convert from count rates to fluxes reliably for sources with $\cos(\vartheta) < 0.4$, and therefore count rate estimates for such sources are not included in the data now archived at the COSSC. The weakest sources we assume to produce negligible effect on the backgrounds under other sources as they rise and set unless they are favorably located in the LAD field of view to give maximum response. Such sources (denoted "W" in Table 1 are not included in the model unless $\cos(\vartheta) > 0.3$. Other sources ("I," intermediate, in Table 1) produce a significant effect on the count rates and are included in the model to a larger ϑ limit, even though their estimated rates are not used for science analysis. We include strong sources ("S" in Table 1) such as Crab Nebula and Cygnus X-1 in the model for every LAD, unless they are almost directly behind the instrument and viewed through the full thickness of the spacecraft. This is done because these sources are so strong that they produce a large change in count rate no matter where they lie in the LAD field of view. A fourth category of likely high-energy sources ("H") is treated like the ("I") category because, although they are weak or absent at lower energies, the LAD response becomes more nearly isotropic at high energy as NaI becomes transparent and total LAD volume is the main factor determining response to a given flux.

2.3.3. *Background Model*

The background model is one of the most critical parts of the analysis system, since it determines the accuracy of the background subtraction, which is the most important component of the systematic error. The model used is a semi-empirical one. Some effort has been expended to make it as physical as possible, as discussed earlier in this section, without attempting the apparently hopelessly complex task of ab initio calculation to the required absolute accuracy. The model currently in use has six general types of terms: (a) a constant rate, due to, e.g., long-term activation of the LADs and components of the spacecraft, (b) terms due to *prompt* effects of cosmic rays (CRs), (c) terms due to activation (Gruber, Jung, & Matteson 1989) of the LADs and spacecraft from passages through the trapped radiation belts (mainly in the South Atlantic Anomaly, SAA), with half-lives in the intermediate range (2 minutes $\ll \tau_{1/2} \ll 1$ day), (d) terms due to the activation of the LADs and spacecraft by CRs, from the same activation species as those considered in (c), (e) a term due to the time-variable blockage of the diffuse cosmic γ-ray background by Earth, and (f) terms due to gamma-rays from Earth's atmosphere, which are themselves prompt secondaries from CRs striking Earth causing electromagnetic showers in Earth's atmosphere (since the atmosphere is effectively not radioactive).

The templates for these terms range from trivial (the template for the constant background is 1.0 everywhere) to fairly complex. Wheaton et al. (1992) have discussed the use of the SDs to monitor the prompt CR component (term "b"). The energies of the SD ULD thresholds were set larger than most long-lived activation energies, but much lower than the energies of cosmic-ray primaries, which are more than 4 GeV for the *CGRO* orbit. Thus, these discriminators count mostly shower secondaries and are a good monitor of the general high-energy radiation environment. Because the CRs are anisotropic and the eight SDs are differently located and oriented, their ULD rates differ and are in fact substantially linearly independent. We use all eight, U_n, $n = 0, \ldots, 7$. The prompt CR model is therefore

$$R_{\rm CR} = \sum_n B_n U_n ,$$

where B_n are eight constants determined from the fit. The same authors (Wheaton et al. 1992) describe the modeling of the activation associated with passes through the SAA (term "c"). Each SAA passage induces a term in the model for each activation species. The template is 0 before the passage, and a unit exponential decay function, of the appropriate lifetime, following the passage. The fitted constant is the increase in activity for the species in question due to that SAA pass. Currently only ^{128}I (half-life 25 minutes) and ^{24}Na (15 hr) are used. Activation due to CRs (term "d") is modeled by convolving the unit decay functions of the type described above with a CR monitor, currently the ULD rate of the SD adjacent to the LAD in question. Inclusion of more SDs would improve the accuracy, at the expense of additional terms in the model.

We adopt a model for the count rate R due to CR-induced atmospheric γ-ray "albedo" of the form

$$R_\oplus = A_\oplus T_\oplus + \left[\sum_n (B_\oplus)_n U_n\right] T'_\oplus \quad n = 0, \ldots, 7 ,$$

where U_n represents a SD ULD monitor for the CRs, as above. Here the "Earth response function" $T_\oplus(\phi', \vartheta', E)$ is the response of the LAD (viewed through the spacecraft) to a uniform disk source of unit intensity, with the diameter of Earth, centered at spacecraft coordinates (ϕ', ϑ') at energy E. In practice, $T_\oplus$ is evaluated by integration of the instrument response over angles in a preliminary calculation used to construct a look-up table for the production processing. Since the atmosphere is essentially not radioactive, we might expect $A_\oplus$ to be zero. However, blockage of the cosmic diffuse γ-ray background by the Earth (term "e") introduces an effect which is formally indistinguishable from atmospheric radioactivity, but negative. The A term is the dominant source of variability in the BATSE LADs at low energy. The $B_\oplus$ terms are caused by gamma-ray secondaries from CRs striking Earth (term "f"), in the approximation that the SD ULDs, U_n, are a good monitor of the CR flux on the local atmosphere below the Observatory. The function $T'_\oplus$ is analogous to $T_\oplus$, except a limb-darkened disk source of unit central intensity is used. The profile for $T'_\oplus$ was adopted from Mahoney et al. (1981), measured by *HEAO 3* for the atmospheric 511 keV line, which we assumed to be applicable over a fairly wide range of energies.

2.3.4. *Singular Value Decomposition*

With the evaluation of the source and background templates, we can form the $I \times J$ matrix equation

$$\boldsymbol{n} = \boldsymbol{A}\boldsymbol{r} ,$$

where $\boldsymbol{A}$ is the matrix whose columns are the J templates times the LAD live time, $(t_{\rm L})_i$, $\boldsymbol{n}$ is the $\boldsymbol{I}$-vector of counts $\{n_i\}$, and $\boldsymbol{r}$ is the vector of unknown rates. In principle we can then solve by standard LLSQ methods for estimates of all the rates and their uncertainties. This is straightforward except for one detail that results from effects of finite-precision arithmetic.

Given the fairly large number unknowns, it may happen that the columns of $\boldsymbol{A}$ are nearly or exactly linearly dependent. This situation is made more likely when gaps in the data reduce the number of available equations. Usually, such linear dependence affects only a small subset of the columns of $\boldsymbol{A}$, so that the rates associated with those columns are either poorly determined (if the linear dependence is only approximate) or completely ambiguous (if it is exact). In either case, the rates of the remaining unknowns are likely to be completely well determined, mathematically, by the data. However, if we simply form the normal equations and solve the LLSQ problem by inversion of the normal matrix, we will find either a serious loss of numerical precision (in the nearly dependent case) or total failure due to a singular matrix (in the exact case). Then even the information in those unknowns, which are mathematically well determined, is degraded or lost. One could in principle solve this problem case-by-case, by examining each nearly singular fit and removing the ill-determined unknowns from the problem. However, because of the large number of fits required in the production data analysis, an automatic equivalent to such a manual procedure is essential.

Thus, we have adopted for the system a singular value decomposition algorithm, as described by Press et al. (1986). The method has the great advantage of being stable even for singular or nearly singular matrices, so that the unknowns for those columns of $\boldsymbol{A}$, which are uninvolved in the linear dependence among some subset of other columns, suffer no loss of precision thereby.

2.3.5. *Removal of Outliers*

Because of the presence of transient effects (e.g., gamma-ray bursts, solar flares, and particle precipitation events) that are not included in the model and not readily predictable, we find that there are occasional intervals where the model significantly departs from the data. Evidently, we have no basis for modeling the data in such regions, as the hypothesized linear model is inapplicable, and they must simply be excluded from the fit.

This is a somewhat delicate question, however, for the following reason. As has been stressed by many authors, recently Wheaton et al. (1995) and Wheaton et al. (1996), in a weighted averaging situation, with data x_i and weights w_i (usually but not necessarily chosen so that $w_i = 1/\sigma_i^2$), it is generally dangerous and often seriously in error to choose the weight w_i as a function of its corresponding data value x_i. Since exclusion of a datum x_i corresponds to setting $w_i = 0$, rejection based on the value of x_i falls into this category. However, if the rejection threshold is set sufficiently high, so that the probability of the data occurring according to the linear model hypothesis is negligible, then such rejection should introduce only negligible bias into the results, because no data for which the model is valid should be excluded.

The algorithm proceeds by first removing data that are too large to be reasonable within the context of the model. We then perform a preliminary fit to identify outliers, currently defined as points, which are more than 5 σ away from the model. Since the probability of a 5 σ datum arising in one bin under the model is approximately 1 in 16,000,000, such a point should occur statistically only about once per month in the entire experiment, even with 4000 data bins per fit. These data are therefore removed from the data set. In order to insure completely removing broad transients with a peak above 5 σ, we also remove adjacent data points on either side of positive outliers until the data return to the level of the model. A second final fit limited to the remaining data then yields the estimated rates used for analysis.

Although the number of counts in each 16.384 s bin is fairly large (hundreds), as a matter of good practice we avoid weighting the equations by $1/n_i$ for reasons discussed by Wheaton et al. (1995). As shown therein, the expectation of the results of the fit are not affected by inaccuracies in the weighting, so long as the weight w_i for each datum is independent of the corresponding data value n_i. The root mean square (rms) uncertainties in the fitted answers attain their minimum values if the weighting is exact, but in practice the errors are very insensitive to moderate inaccuracies in the weights. In the context of the iterative fit described above, we use no weighting for the preliminary fit and then use the model from the preliminary fit to determine the weights for the final fit.

2.4. *Systematic Error and Sensitivity*

In the reduction of the total uncertainty in the analysis to a minimum, a design trade-off between systematic and statistical errors is unavoidable, and comes about as follows.

Suppose we analyze an occultation experiment in the simplest possible way, taking a window $\pm\tau$ on each side of the occultation edge of a known source. We evaluate the count rate when the source is up, on one side of the edge, and the background, when the source is down, on the other. Subtracting the two, we estimate the net source rate. The statistical error in the estimation clearly diminishes as τ is increased, as the square root of τ if the source is weak.

It is obvious that if there were no systematic errors, one would simply take τ as large as possible, thus minimizing the Poisson error. However, if τ is too large, the background under the source may not be well represented by the resulting count rate when the source is down, because the background may vary due to other sources and numerous other causes.

Evidently, we minimize this systematic effect by taking τ as small as possible. It is obvious that either extreme, τ very large or τ very small, is untenable in a useful estimation procedure. In this simple form of the analysis, it is clear that some intermediate value of τ minimizes the total uncertainty in the estimate of the source count rate.

It is our experience and belief that even in more sophisticated forms of the analysis, such as the linear multisource, parameterized background least squares analysis we have used in EBOP, an equivalent trade-off always arises. Because the precise nature and extent of the background variability responsible for the systematic errors noted above is not known in advance, the optimum point for the tradeoff cannot be determined a priori, but must be set iteratively. In our early experience with modeling BATSE data, the linear background model was much more successful than we had initially expected, and as a result we performed the analysis reported here on a relatively long, 1 day basis, considerably simplifying the handling of various operational problems (effects of gaps, reduction in data volume, etc.). A modification of the analysis to permit a more flexible treatment of the time variability of the background is under consideration as a possible future improvement, which would make it simpler to optimize the estimation.

As is evident from the preceding discussion, the analysis of Earth-occultation data inevitably requires estimates of

both statistical and systematic errors in assessing the total uncertainties in the results. It is clear that systematic errors are present, and important in some parts of this catalog.

2.4.1. *Types of Systematic Error*

It is useful to divide systematic errors into two distinct categories. The distinction is closely related to that traditionally described between the accuracy and precision of measurement. They may also be regarded as roughly multiplicative and additive, respectively.

2.4.2. *Transducer Errors*

The first we may call "transducer errors": in our context they are typified by errors due to uncertainty or inaccuracy in converting the observed source count rates into physical fluxes. Such errors are commonly proportional to the measured quantity, and for EBOP will typically be a fraction of the source flux, roughly independent of the background. They are therefore most evident for stronger sources. Uncertainties of this type clearly depend on the accuracy of the prelaunch calibrations and also on the very extensive Monte Carlo modeling (Pendleton et al. 1995) which has been carried out by the MSFC group to fill in the details of the instrument response matrices, on which all our conversions are based. Historically in gamma-ray astronomy, typical errors in the measurement of absolute fluxes have been in roughly the 10%–30% range, although larger errors have clearly occurred more frequently than has been recognized at the time. In any case, we believe that $\pm 15\%$–20% is a fair overall estimate for the accuracy of BATSE Earth-occultation observations. Based largely on the agreement of the spectral index of the Crab Nebula with results published in the literature, it appears that spectral slope accuracy is substantially better than this, except perhaps at the highest energies. Note that errors of this type are almost irrelevant in determining source detection sensitivity, for which only count rates are necessary.

2.4.3. *Model Errors*

Errors in the second category are similar to Poisson errors in that they are small variable count rates which appear as additive noise at a level independent of source strength; they are clearly of greatest concern for the weakest sources and may determine the effective sensitivity of the analysis. In general we attribute them to "model errors": terms in the true LAD count rates which have no counterpart in the linear model used for the analysis, or for which the model templates are computed inaccurately. Such errors are of paramount interest for characterizing the flux, spectrum, and variability of weaker sources, as they may exceed the Poisson error σ_P and, for EBOP, are never negligible in comparison to σ_P for data accumulations of a day or more.

Much of the effort at JPL has been devoted to suppressing such errors. Nevertheless, omissions and shortcomings in the model, particularly in the background portion, certainly account for much of the residual systematic error. A number of known or likely sources of model error remain. The most important of these are believed to be the following:

1. Unmodeled sources: EBOP is fundamentally limited in that it merely measures count rates due to known sources, but, especially at higher energy (>500 keV), our knowledge of the sky is quite incomplete. A further complication is the large number of transient and flaring sources, which are not known a priori.

2. Extended sources: Strong effects due to the Galaxy were not anticipated and have not been included in the present model. Especially for the Galactic 511 keV emission, this has turned out to be a significant contribution.

3. Atmospheric Compton scattering of source fluxes: In the low-energy gamma-ray region Earth is a rather good diffuse reflector, due to Compton scattering. The reflected flux from strong sources like Cygnus X-1 and the Crab Nebula is likely to be an important contribution to the count rate, but we have neglected it to date. We believe that the effect is small near the rise and set of the reflected source, when the portion of Earth illuminated by the source appears as a thin crescent. It can be shown that the rate estimate for a given source is mainly determined by data near its rise or set. For this reason the associated error in the results for Cygnus X-1, the Crab, and other strong sources themselves, seems likely to be small. (Note that such effects, proportional to source flux, would be classed as transducer errors in the terminology above.) However, the count rate due to reflection from strong sources will in general affect the fitted rates obtained for other, weaker sources.

4. Incomplete activation model: Computational limitations also forced us to truncate the model at only two activation species, ^{128}I and ^{24}Na for the data analysis reported here.

5. Variability of strong sources: Vela X-1 (a strong slow HX pulsator) and Cygnus X-1 (episodic strong flickering), in particular, have a significant effect on the χ^2 obtained in the analysis of the LADs viewing them.

It appears that effective approaches exist for improving the model to largely remove all the above effects, and for obtaining useful measurements on those of astrophysical interest, such as variability of strong sources and mapping the Galactic diffuse emission.

In the absence of a more satisfactory method, we give a phenomenological characterization of the systematic errors by two somewhat different methods, in order to provide some semiquantitative guidance to the user of the data. Although the estimation of statistical uncertainties we use is straightforward and useful, no truly satisfactory method of evaluating systematic errors is known to us. The first method applies to individual scans and detectors but is averaged over sources. The second is carried through for 1 day averages over all detectors, for the Crab Nebula only.

2.4.4. *Single-Scan Errors*

In this analysis we suppose the total error σ_T is the sum of two components, systematic (σ_S) and statistical (Poisson, σ_P), and assume that they can be added in quadrature:

$$\sigma_T^2 = \sigma_P^2 + \sigma_S^2 \, . \tag{1}$$

So long as the expectation of the errors ε_s and ε_P are both zero, the validity of this assumption depends only on the two terms in the total variance, statistical and systematic, being uncorrelated. The Poisson error ε_P has zero expected value and is guaranteed to be independent of all other sources of error. Hence, the value of this approach in practice depends on the extent to which ε_s is small.

We find that systematic errors depend on both energy band k and LAD n. The dependence on LAD may be due to the effects of different fields of view and responses of LADs to cosmic sources, as well as different background measured by LADs. Since so many plausible types of model errors

depend on detector orientation in space, and this is constant within a VP, we analyze σ_S separately for each VP. If we construct a histogram of the count rate estimates, lumping together all the sources seen by a given LAD in a given energy channel, we obtain a distribution which is the result of convolving the different source rates, and any source variability, with the total error. The distribution has a pronounced asymmetry and a tail to positive count rates, due to the presence of real cosmic γ-ray sources. Removing the known stronger sources, we can construct a "weak source" histogram (Fig. 5) which is much more nearly normal in form. If we conservatively suppose all these sources have negligible count rates, the rms width is due to the combined effect of statistical and systematic errors. We take the rms width of this distribution as representative of the total uncertainty in a given rate estimate.

If we divide the estimated rate for each source by its statistical error σ_P to obtain the significance, we may construct an analogous histogram of the significance of weak sources. In the absence of systematic error or real γ-ray sources, the rms width of this histogram would be 1.0, being due to statistical noises alone. In fact (see Fig. 5) its width is always greater than 1.0, due to the combined effect of weak sources and σ_S. Neglecting the former, we suppose it is conservative to assign the entire excess to the effects σ_S. With this assumption we can calculate the relative sizes of σ_T, σ_P, and σ_S. Then returning to the estimate of σ_T obtained from the rate histograms, we can assess σ_S. The total error σ_T is then converted from the count-rate space to photon space through XSPEC (see § 2.3) and propagated through the rest of the EBOP system.

These estimated total uncertainties, computed as the sum in quadrature of the Poisson and systematic uncertainties, have been used consistently in Figures 7 and 8 and Table 3. Note that this analysis, since it is based on histograms of data in source count rates (rather than fluxes), takes no account of that part of the systematic error due to errors in the detector response matrices and spectral fitting. Because it operates on smaller chunks of data, namely individual scans and detectors, than the method described below based on the variability of the Crab, statistical errors are relatively larger and systematic errors less evident.

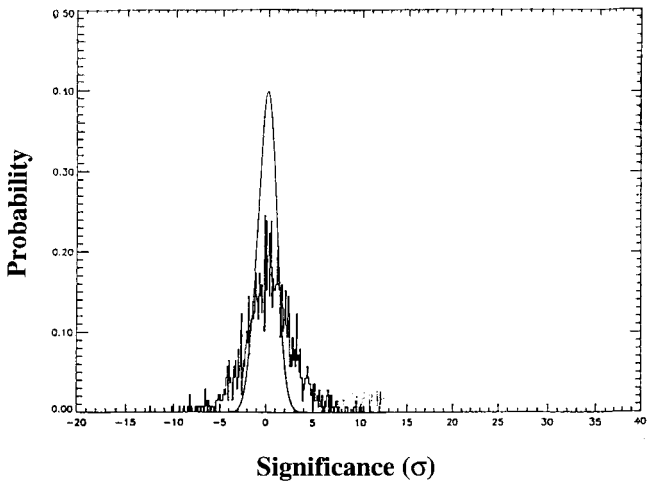

FIG. 5.—Count rate histogram for weak sources. The rms width of the distribution, which is wider than that for the Poisson distribution, is used to represent the total uncertainty in the given rate estimate.

2.4.5. *1 Day Average Systematic Error, Based on Apparent Crab Variability*

In addition to the above analysis, we also performed an assessment of the residual systematic error based on the variability of the 1 day average Crab fluxes obtained by EBOP, averaged over all detectors. In this approach we assume that the Crab Nebula flux is truly constant and attribute any significant observed changes to systematic error, of whatever sort. Since statistical variations are expected, in principle we need to subtract them; which we have attempted to do by the following procedure.

Consider a data set of the form $\{F_i, \sigma_i\}$ where F_i are measured estimates of the physical source flux F and σ_i are the corresponding rms measurement uncertainties, with $i = 1, \ldots, I$. If all the F_i were drawn from a population with a single underlying mean F_{mean}, we could use the usual weighted average formulas to estimate F_{mean} and its uncertainty. This is correct even if the F_i-values are not normally distributed, so long as the σ_i^2-values are the variances of the measurements, and the F_i-values are drawn from a population with a single unique mean. However, the χ^2 test with $n = I - 1$ degrees of freedom shows that the data are not consistent (here the assumption of normality is necessary) with the given σ_i and F_{mean} as the unique mean, evaluated by the standard formula. Therefore, we consider the possibility that the measured quantity F might vary as a function of other unobserved and uncontrolled "hidden" parameters in the measurement, the source of systematic error. We assume that the σ_i correctly describe the portion of the measurement error that would be observed if the hidden parameters could be held fixed, but that the distribution of the observed F_i results from a convolution of the distribution of the given measurement uncertainties σ_i with the unknown distribution of the systematic error.

An example of such a situation, very closely related to that here, would be a set of observations $\{F_i, \sigma_i\}$ of a physical count rate varying randomly with time according to some unknown underlying pdf (probability density function) $P(F)$ but observed in the presence of known Poisson uncertainties. We wish to characterize the underlying physical count rate and its true variability, taking into account the effects of the Poisson noise. Thus, we would like to estimate from the data the parameters of the underlying pdf P for F, especially its mean and rms width $\sum_F$, along with their uncertainties. In taking this approach we are implicitly assuming that F is stationary and that the measurements are uncorrelated with the unknown parameters that are causing F to vary. If the σ_i were all equal, we could use the unweighted mean of the F-values and the rule for the "mean of the square minus the square of the mean," unbiased as usual by factor $I/(I-1)$, to estimate the rms width of the distribution P.

A simple generalization of the same rule to the case of variable uncertainties is

$$\sum_F^2 = \left(\frac{I}{I-1}\right) \times \left\{\sum_j (F_i/\sigma_i)^2 \Big/ \sum_j (1/\sigma_i^2) - \left[\sum_j (F_i/\sigma_i^2) \Big/ \sum_j (1/\sigma_i^2)\right]^2\right\}. \quad (2)$$

This form is obtained by substituting the usual weighted average for the mean, and recalling that a weight of I corresponds to I repetitions of the same sample in the sum. Thus, we try to replace I by $\sum_j (1/\sigma_i^2)$, subject to the constraint of

dimensional correctness. This formula reduces to the standard one when all σ_i are equal and gives sensible answers in the cases we have examined. Given this expression for $\sum_F$, the distribution of the measurements should be given by the convolution of the *pdf* of the measurement process itself with $P(F)$, and the total variance, for a single measurement I, would be $(\sum_F^2 + \sigma_i^2)$. In applying this approach to estimate the systematic error in EBOP measurements of the Crab flux, we take $\{F_i, \sigma_i\}$ to be the $I \sim 612$ daily flux estimates in a given energy channel and use equation (1) to obtain an estimate $\sum_F$, of the systematic error which must then be added in quadrature to each uncertainly σ_i. We finally go back to the weighted averaging procedure, using this revised expression for the uncertainty of each measurement, to get a mean for F and a measure of its uncertainty.

Carrying through this procedure for each of the 14 energy channels in turn gives the final Crab spectrum shown in Figure 6 as a histogram, and its total 1 σ standard error shown by the dashed line (see also Table 2). Subject to the assumption that the observed apparent variability of the Crab can be used to estimate systematic errors for other sources, the latter is a measure of effective sensitivity.

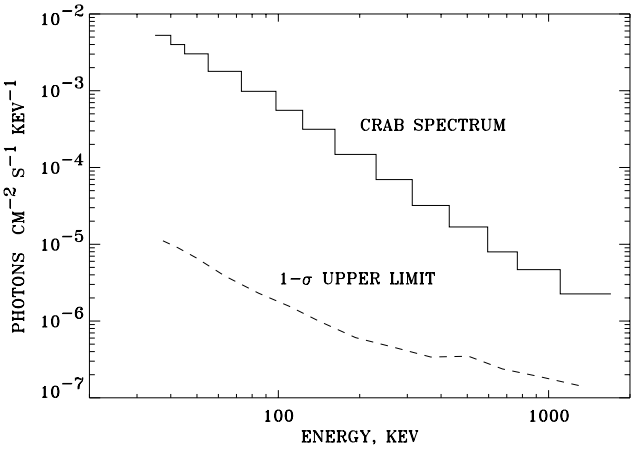

FIG. 6.—Estimated effective 1 σ uncertainty (*dashed line*) in the total flux for EBOP over the 1200 day period ($\sim$612 days included), with residual systematic effects, evaluated by attributing the apparent flux variability of the Crab entirely to systematic error. The corresponding EBOP estimate of the total flux (*histogram*) from the Crab Nebula and pulsar is shown for comparison.

2.5. *XSPEC Spectral Fit*

The count rates obtained from the occultation analysis were converted into flux estimates using the XSPEC (Arnaud 1996) spectral analysis program (step 10 in Fig. 3). Because of uncertainties in the effective band edges and the efficiencies at high and low energy, only the middle 14 of the 16 CONT energy bands were converted to photon fluxes; their energies appear in Table 2. In this step we fit the data from all LADs with a good view of the source (defined by the criterion that cos $(\vartheta) > 0.4$ where ϑ is the angle between the LAD normal and the source) to a single spectral model. For sources of moderate strength, in time intervals of one VP, a simple power-law model was adequate to describe the spectra. Each LAD included in the fit had its own detector response matrix (step 9 in Fig. 3), computed from the aspect during the VP and the source position. XSPEC was used to fit the daily spectra for each source as well as the VP spectra. For the VP spectra, the available daily count rates were combined by weighted averaging for each channel for each LAD and the results used as input to XSPEC for determining the photon fluxes in each of the 14 bands.

Results of the fit are put in a XSPEC formatted history (.xhs) file which contains count-rate spectra (in counts cm^{-2} s^{-1} keV^{-1}) and photon spectra (in photons cm^{-2} s^{-1} keV^{-1}) for each of the LADs as well as the best-fit model spectrum.

In summary, the steps required for the XSPEC analysis leading to the final display of spectra and light curves shown in this catalog are as follows:

1. A program, BATPHA (step 7 in Fig. 3), which reads the ASCII SOURCE files with count rate estimates together

TABLE 2

LIST OF 1 σ SENSITIVITY BASED ON 612 DAYS OF OBSERVATIONS

ENERGY RANGE (keV)	CRAB FLUX (photons cm^{-2} s^{-1} keV^{-1})	1 σ SENSITIVITY ($\sim$612 days)	
		(photons cm^{-2} s^{-1} keV^{-1})	(mCrab)
35–40	0.005271	1.1E−05	2.1
40–45	0.003996	9.0E−06	2.3
45–55	0.003025	6.6E−06	2.2
55–73	0.001788	3.9E−06	2.2
73–98	0.0009827	2.3E−06	2.3
98–123	0.0005560	1.6E−06	2.8
123–162	0.0003148	1.0E−06	3.2
162–230	0.0001480	6.1E−07	4.1
230–313	6.964E−05	4.5E−07	6.5
313–429	3.201E−05	3.4E−07	10.6
429–595	1.682E−05	3.5E−07	20.7
595–766	7.962E−06	2.4E−07	29.8
766–1104	4.673E−06	1.9E−07	40.6
1104–1700	2.258E−06	1.4E−07	61.1

NOTES.—List of 1 σ sensitivity based on 612 days of observations, expressed in photons cm^{-2} s^{-1} keV^{-1} and mCrab units, respectively, in 14 energy channels, and the Crab fluxes derived by EBOP.

with the systematic error files, computes the total uncertainties, and generates instrument data (.pha) files which can be read by XSPEC.

2. A program, BATSERSP (step 9), which creates LAD response (.rsp) file compatible with XSPEC. Input for this program comes in turn from a FORTRAN program incorporating a LAD model provided by the BATSE P. I. team at MSFC.

3. XSPEC itself (step 10), which fits the data to a specified model, using the LAD response matrix. The output is written to XSPEC history (.xhs) files (step 11).

4. A program, XHS_READ3 (step 12), which reads XSPEC history files and puts the data into a two-dimensional time/energy array format spectral or time-history files.

5. A package MULSCN (step 13) of IDL-callable procedures which allow the user to read, print, plot, or further manipulate spectra or time series.

2.6. *LAD Consistency Test*

Since the *CGRO* maintains a fixed orientation in inertial space during each VP, and the LADs are oriented differently, the count rate for a given source generally differs from LAD to LAD. Consequently, consistency of fluxes measured by the different LADs is an important check on the results. We assess the consistency among detectors of all the daily spectra as part of our routine data analysis procedure (Ling et al. 1996). We first compute for each of the 14 energy bands k, the weighted-average flux f_k, for each LAD n, where $n = 1, \ldots, N$, and N is the number of LADs (typically 2 to 4) exposed to the source for the VP, such that the cosine of the angle between source and the look-axis (i.e., normal to the LAD) vector of the detector is greater than 0.4. We take as inputs for each k the individual fitted photon fluxes f_{nk} from the XSPEC model fit. Then $\chi^2 = \sum_k \chi_k^2$, where $\chi_k^2 = \sum_n (f_{nk} - f_k)^2/\sigma_k^2$, is a good measure of consistency, with degrees of freedom $\nu = 14(N - 1)$. Large χ^2 is thus entirely due to inconsistency among detectors. We reject days with probability $P(\chi^2, \nu) < 5\%$.

2.7. *Data Products at the CGRO Science Support Center*

Programs and data products currently archived at the COSSC include the following:

1. The cosmic source count rates and uncertainties, in 16 energy channels (note: only the inner 14 channels are used in this catalog), in ASCII "SOURCE" files, one per LAD per day for the first three phases of the mission, covering the period between 1991 May 17 and 1994 October 3 (TJD 8393–9628). Days bounding VPs, in which there is a spacecraft maneuver, are not yet included in the database.

2. For each VP, a small ASCII file containing estimated systematic errors for each LAD and each energy channel.

3. Software to generate LAD response information in XSPEC-compatible files.

4. Software to read the SOURCE files and systematic error files, and write XSPEC-compatible .pha files, with total uncertainties estimated according to § 2.4.

5. Software to read the XSPEC output history (.xhs) files, and write a two-dimensional energy/time MULSCN compatible ".mulpha" or ".hist" files, for spectral and time series presentation of the data, respectively.

6. Software to plot, print, and manipulate spectra and time series produced by XSPEC.

3. RESULTS

3.1. *Flux Histories*

Figure 7 shows flux histories with 1 day resolution of the 35–200 keV broadband energy for each of the 34 sources covering the first three phases of the *CGRO* mission. Error bars are our best estimate of the total uncertainty, Poisson and residual systematic, as described in § 2.4.4. The vertical dashed lines mark the boundaries of the three 400 day periods over which average spectra shown in Table 3 and Figure 8 were obtained.

3.2. *Spectra*

Table 3 and Figure 8 show spectra integrated over three separate periods of ~400 days each, spanning the total ~1200 day period reported here, plus spectra for selected shorter intervals in which significant or interesting variability was observed. Units are keV for the energies and photons $cm^{-2}\ s^{-1}\ keV^{-1}$ for flux and errors. Once again, errors bars are our best estimate of the total uncertainties, as described in § 2.4.4. The spectra in the table are generally arranged with the three 400 day periods (denoted periods 1, 2, and 3 in the plots of Fig. 8), across the page, followed by supplementary panels of spectra for shorter periods for some sources. Many panels in Figure 8 also show a representative power-law fit to the Crab Nebula spectrum measured by BATSE, overlaid as a reference. Also included in some panels are selected spectra measured by OSSE, COMPTEL, SIGMA, and *HEAO 1* to be compared with the BATSE results. Some of these comparisons are discussed in § 4.

Examination of the results in Figure 8 and Table 3 indicates two particular areas where some of the results may be anomalous; (1) the appearance of features in the 429–595 keV channel containing the 511 keV positron annihilation line (e.g., 1E 1740−29), and (2) high-energy fluxes (above the 511 keV line) in some sources (e.g., EXO 1846−31).

Regarding the 500 keV region, we believe that in most cases this effect is due to the Galactic diffuse 511 keV emission masquerading as a discrete source effect. The EBOP analysis has focused on point source monitoring, and the linear model (§ 2.4) has no terms for any cosmic diffuse source except for the cosmological isotropic component. Thus, if there is diffuse emission which is strongly peaked near (a few degrees) a source in the catalog, it is inevitable that the present analysis will attach some of that diffuse flux to the source, depending on the presence of other sources, their number, distance, and geometry. The Galactic center annihilation line, in particular, is strongly peaked spatially, based on OSSE mapping observations (Purcell et al. 1996), and a number of catalog sources are located in its immediate vicinity. Thus, for example, 1E 1740−29, the black-hole candidate in the Galactic center region, shows a 511 keV feature in the three 400 day spectra, which must surely contain contributions from the Galactic diffuse emission (Purcell et al. 1996; Skibo, Ramaty, & Purcell 1996). Other sources showing the excess 511 keV feature also tend to lie in the vicinity of the Galactic center.

Deconvolution of occultation data to measure a mixture of point and diffuse fluxes is clearly a more difficult problem than the discrete source monitoring EBOP was devised to perform. In retrospect, it seems that the effective "aperture" of the Earth-occultation method is probably rather well matched to the diffuse source distribution, so that this effect

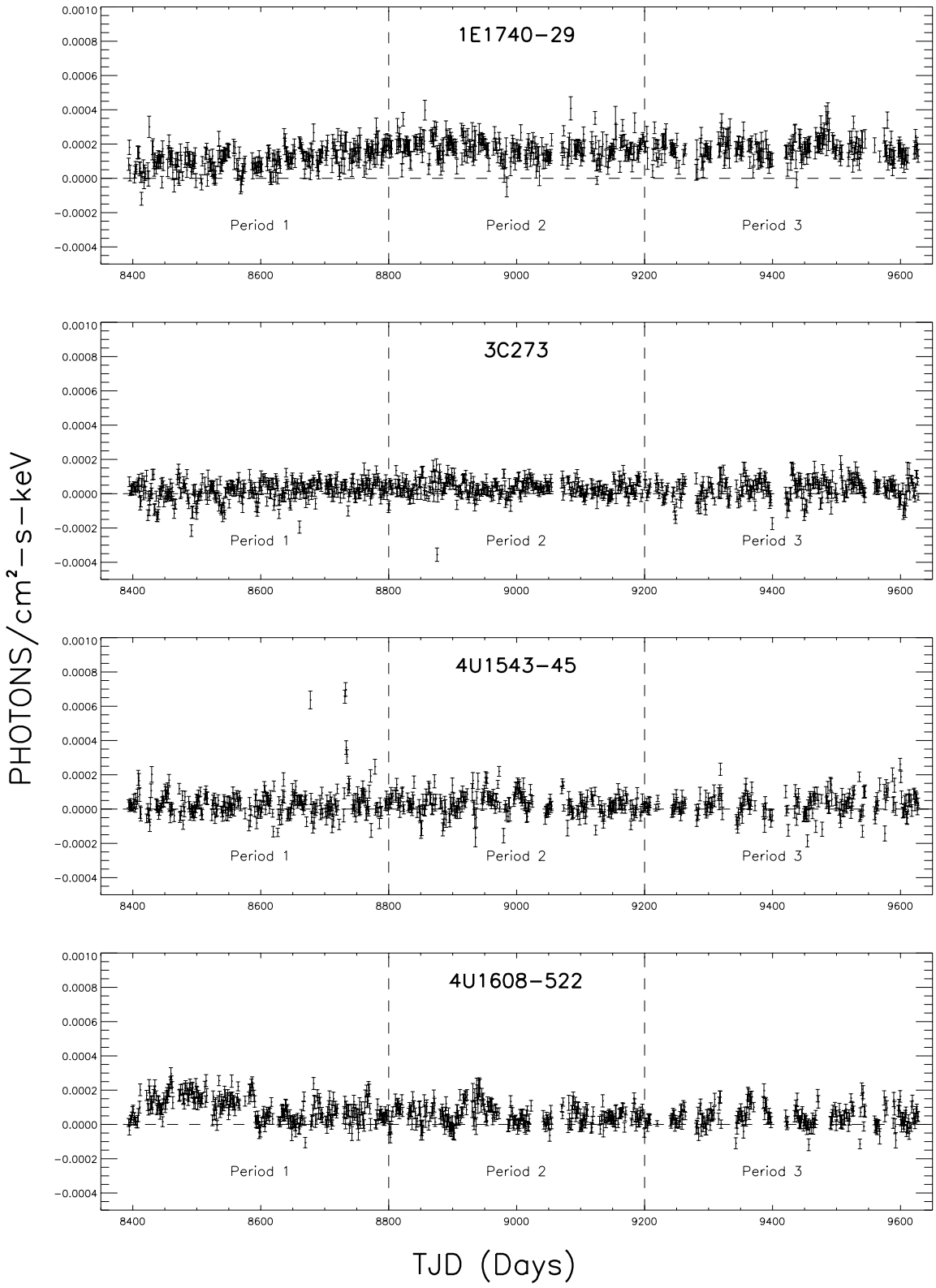

FIG. 7.—Light curves of the 35–200 keV flux in 1 day resolution for each of the 34 gamma-ray sources included in this catalog. See § 2.4.4 for a discussion of the error bars.

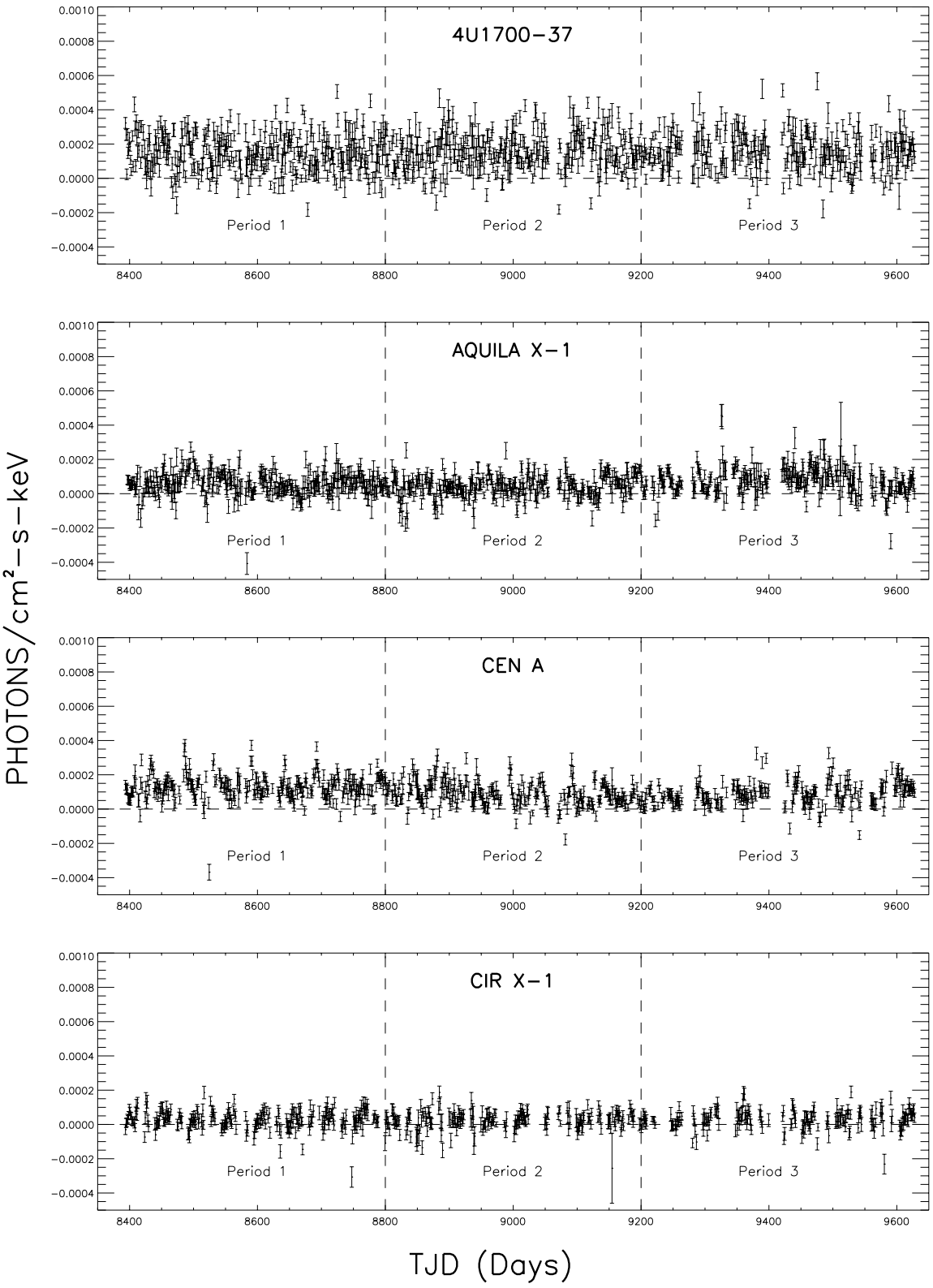

FIG. 7.—*Continued*

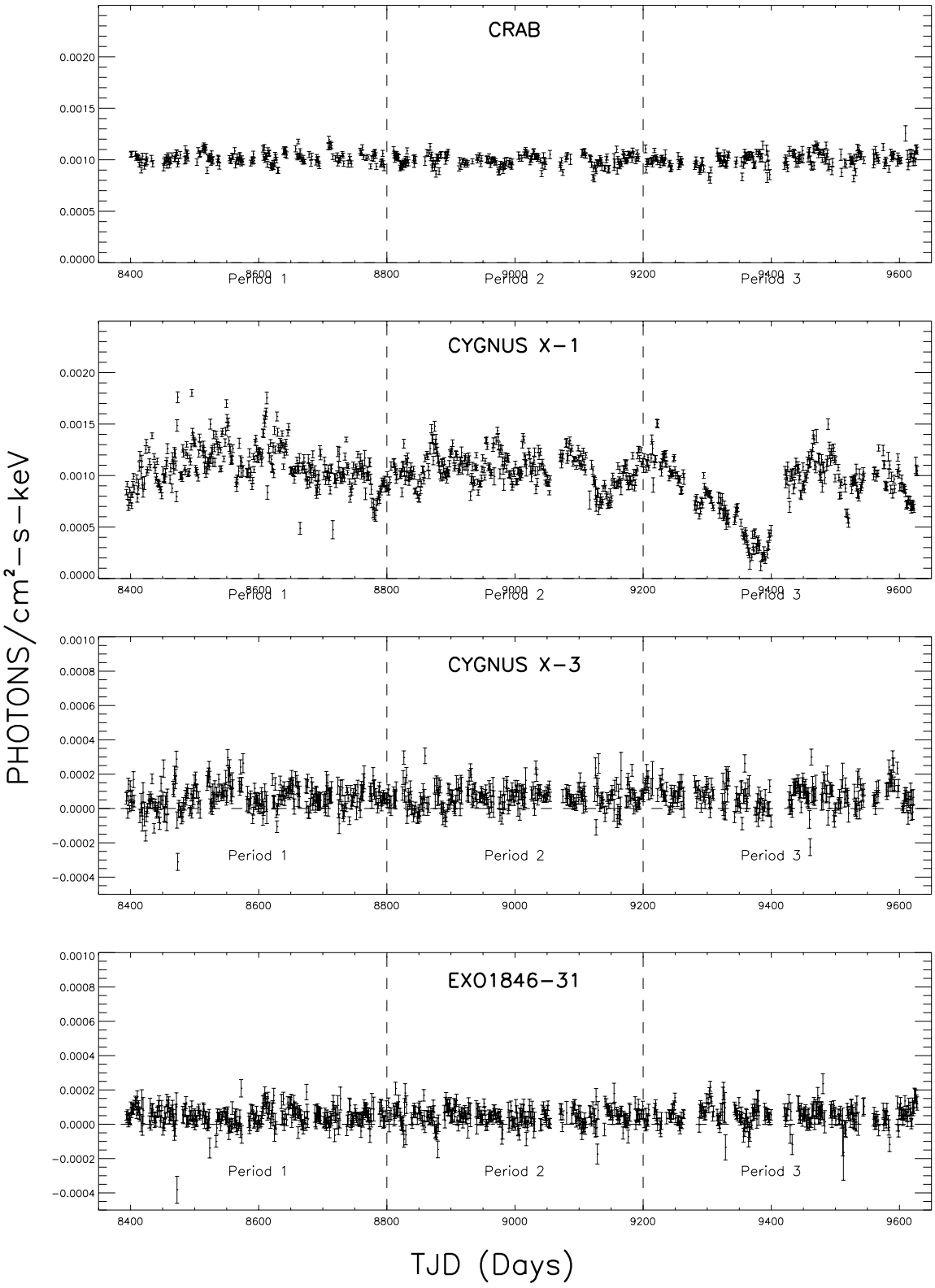

FIG. 7.—*Continued*

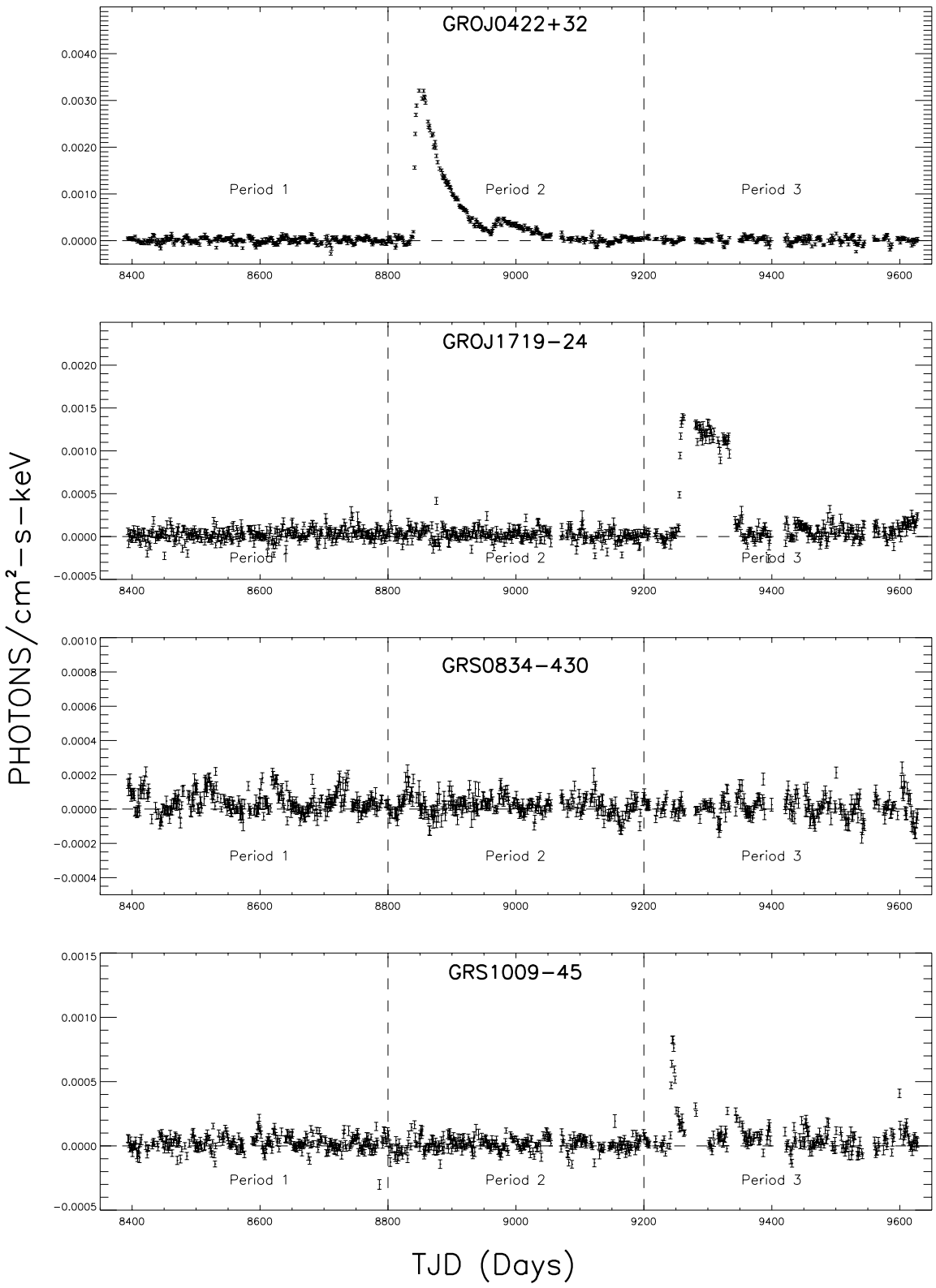

FIG. 7.—*Continued*

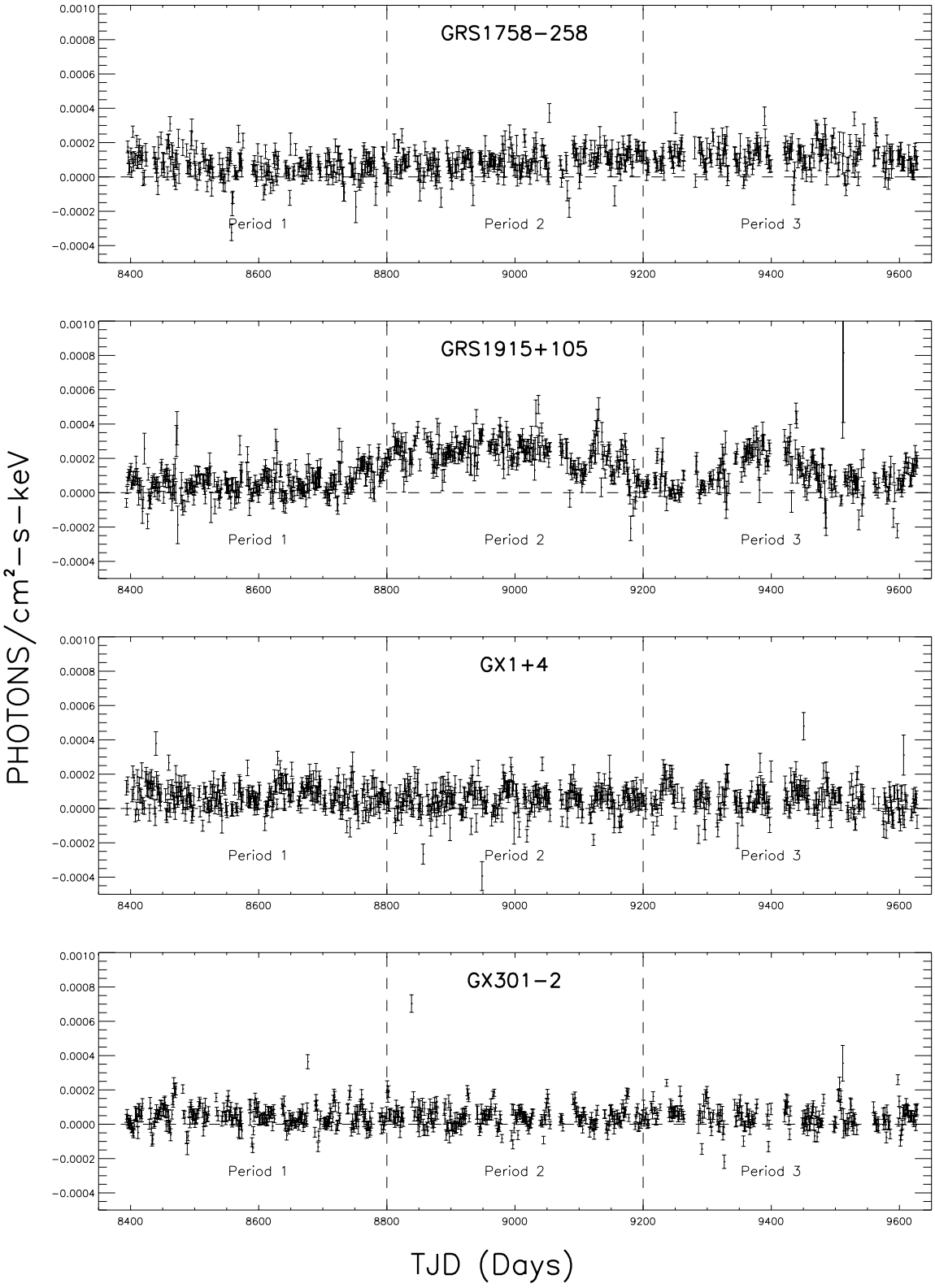

FIG. 7.—*Continued*

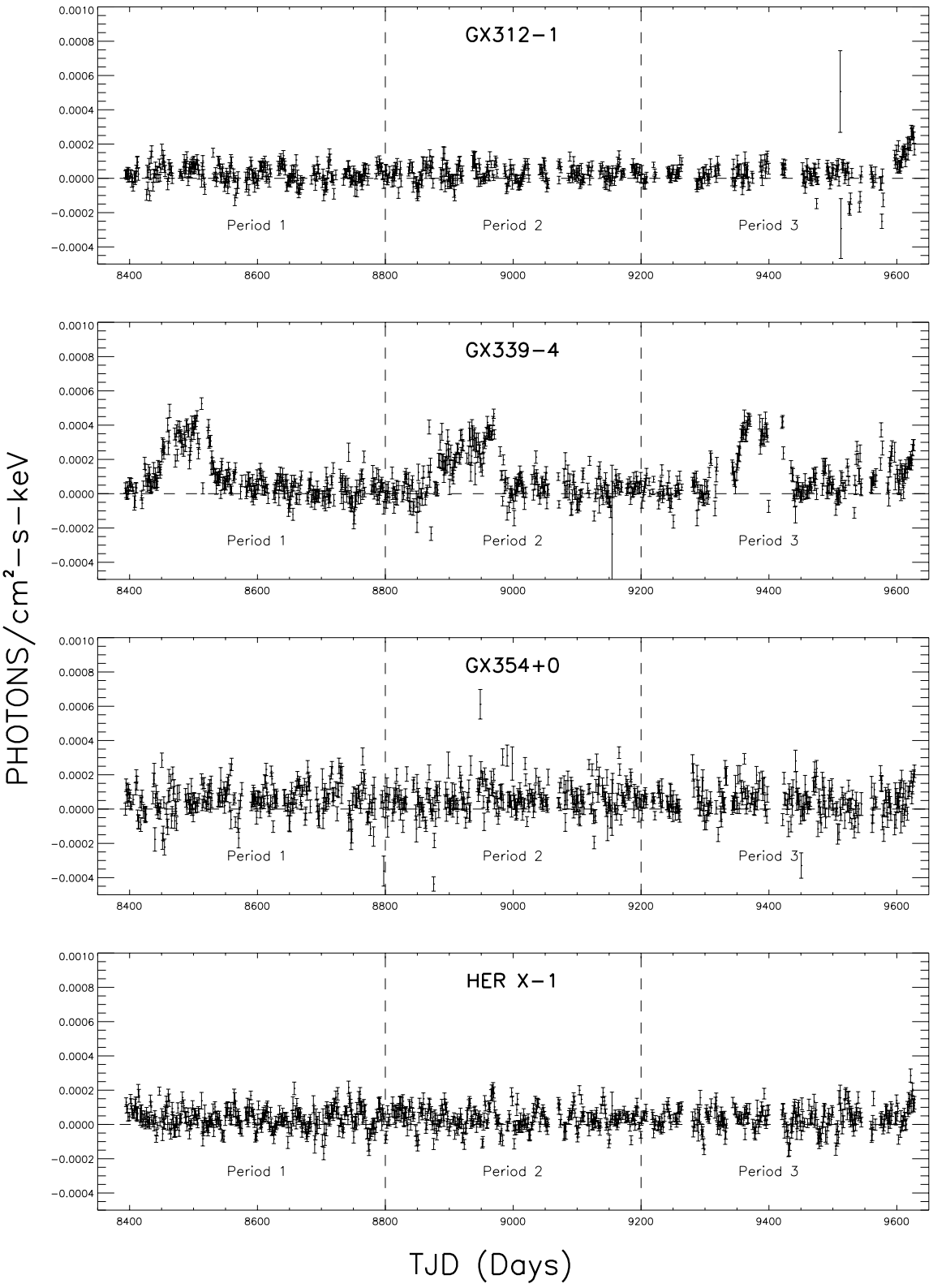

FIG. 7.—*Continued*

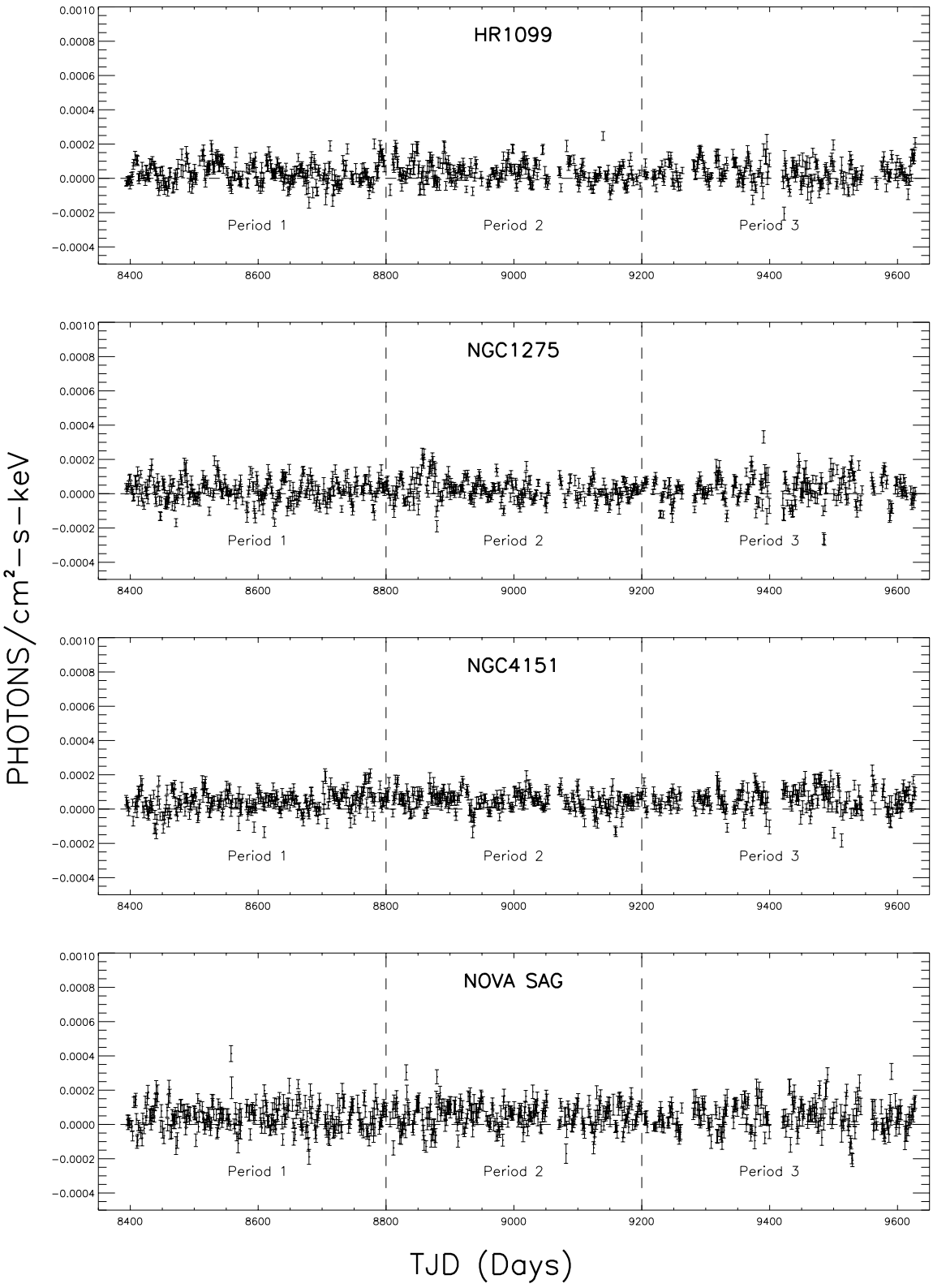

FIG. 7.—*Continued*

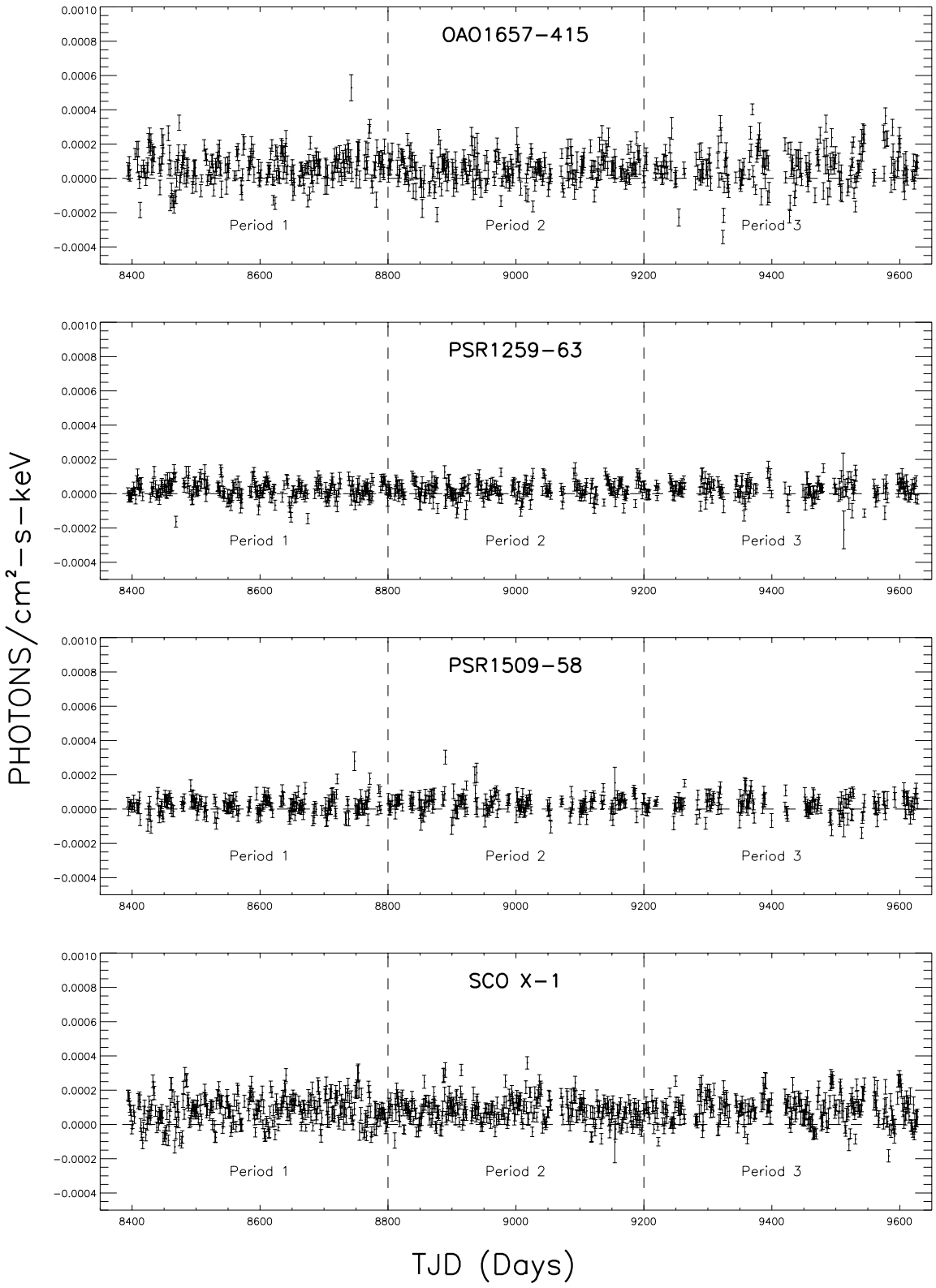

FIG. 7.—*Continued*

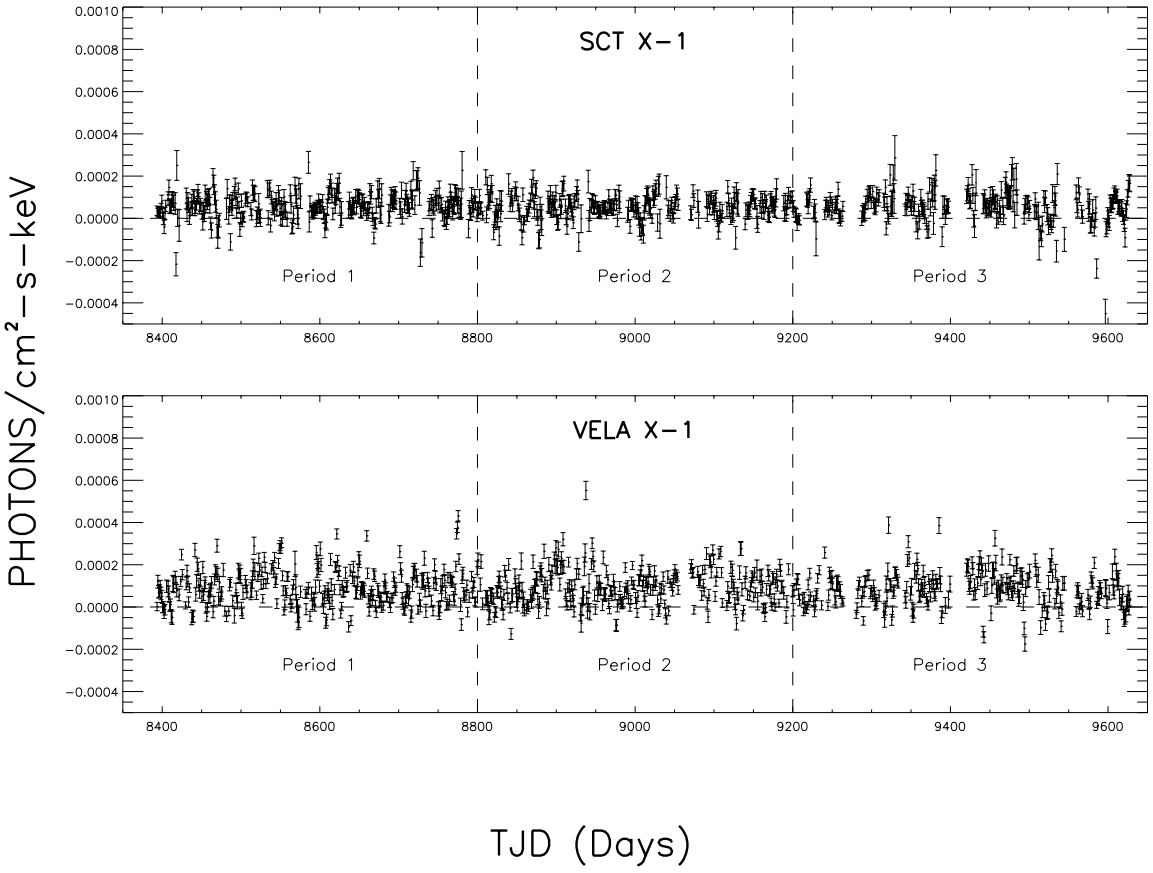

FIG. 7.—*Continued*

might have been anticipated. In any event, the unexpected strength of the diffuse 511 keV line suggests that the Earth-occultation method, probably using a tomographic approach (Zhang et al. 1993; Dixon et al. 1997), has the ability to locate unknown discrete sources and map the diffuse sources with good spatial resolution and sensitivity.

The strong high-energy (>500 keV) fluxes observed for several sources are interesting, but the cause is not so clear. In the EBOP analysis described in § 2, the source flux was determined independently for each detector daily over a variable background that was very different for different detectors. In order to pass our internal checks, the flux must be consistent among all the LADs viewing the source. The fact that many of these sources (e.g., NGC 1275, panel 62; SCTX-1, panel 74; etc.) show also consistent high-energy fluxes over several 400 day period seems to rule out most known background effects. For the best-studied sources, namely the Crab Nebula (Much et al. 1995) and Cygnus X-1 (Ling et al. 1987; Philips et al. 1996; Ling et al. 1997), where extensive cross-checking with other experiments is possible due to the good availability of comparable published observations, EBOP results have been especially well confirmed.

For other sources such as NGC 1275 and SCT X-1, etc., readers are advised to treat the high-energy fluxes with caution. Although any of these may be largely or entirely real, there are also noncosmic possibilities that may explain all or part of the effect. In particular, because EBOP is based on a catalog of known sources, it is vulnerable to effects due to sources omitted from the catalog. A number of possible solutions are possible, ranging from enlarging the catalog to the exploitation of the tomographic method mentioned above.

Other possibilities include model errors such as those mentioned in § 2.4.3 and occasional high-energy flaring by cataloged or unknown sources. Because Earth remains completely opaque and sharp-edged to the highest energies, further development of the occultation method incorporating improvements of the background model, an improved catalog, and better means for detecting and locating uncataloged sources appears uniquely promising for extending our understanding of the sky above 500 keV.

4. COMPARISON OF BATSE RESULTS WITH OTHER MEASUREMENTS

Comparison of BATSE/EBOP results with other measurements is critical for establishing reliable information about the source. Using a relatively stable spectrum such as the Crab's for such comparison, it would be an important check on the EBOP technique as well. Figure 8, panels 12 and 13, show direct comparisons of the Crab spectra measured simultaneously by BATSE, OSSE (Much et al. 1995) and COMPTEL (Much et al. 1995) for VPs 213 and 221, respectively. The BATSE results were derived using both the JPL EBOP system, and the MSFC method. The latter were published earlier in a joint paper with the OSSE and COMPTEL results (Much et al. 1995). For both VP 213 and VP 221, the BATSE/EBOP and BATSE/MSFC fluxes are consistent to within the 1 σ level throughout the entire 0.03–1.8 MeV range. However, they are both higher than those of OSSE by $\sim$30% in the 55–74 keV range and

TABLE 3

TIME AVERAGED FLUXES OF 14 CHANNEL SPECTRA FOR EACH OF THE 34 GAMMA-RAY SOURCES

		1E 1740−29: FLUX ± σ (photons cm^{-2} s^{-1} keV^{-1})					
NUMBER	ENERGY (keV)	TJD: 8393–8800 Fig. 8, Panel (1-P1)	σ	TJD: 8800–9200 Fig. 8, Panel (1-P2)	σ	TJD: 9200–9628 Fig. 8, Panel (1-P3)	σ
1	35–40	6.556E−04	2.47E−05	9.531E−04	2.62E−05	9.139E−04	2.75E−05
2	40–45	4.918E−04	1.94E−05	6.986E−04	1.94E−05	7.008E−04	2.22E−05
3	45–55	3.126E−04	1.26E−05	5.049E−04	1.30E−05	5.038E−04	1.45E−05
4	55–73	1.769E−04	6.67E−06	2.916E−04	6.98E−06	2.897E−04	7.64E−06
5	73–98	8.642E−05	3.87E−06	1.622E−04	4.06E−06	1.569E−04	4.49E−06
6	98–123	4.792E−05	2.50E−06	8.961E−05	2.65E−06	9.193E−05	3.01E−06
7	123–162	2.704E−05	1.60E−06	5.087E−05	1.70E−06	5.197E−05	1.96E−06
8	162–230	1.494E−05	1.00E−06	2.405E−05	1.05E−06	2.515E−05	1.23E−06
9	230–313	9.234E−00	7.33E−07	1.241E−05	7.82E−07	1.280E−05	9.36E−07
10	313–429	6.147E−06	5.46E−07	6.605E−06	5.97E−07	6.244E−06	7.02E−07
11	429–595	5.061E−06	5.37E−07	4.573E−06	5.85E−07	5.959E−06	7.04E−07
12	595–766	2.025E−06	3.79E−07	1.493E−06	4.15E−07	1.843E−06	4.60E−07
13	766–1104	1.522E−06	2.83E−07	1.112E−06	3.17E−07	1.557E−06	3.70E−07
14	1104–1700	1.322E−06	1.90E−07	3.682E−07	2.27E−07	1.210E−06	2.64E−07
		3C 273: FLUX ± σ (photons cm^{-2} s^{-1} keV^{-1})					
NUMBER	ENERGY (keV)	TJD: 8394–8800 Fig. 8, Panel (2 & 3-P1)	σ	TJD: 8800–9197 Fig. 8, Panel (2-P2)	σ	TJD: 9200–9628 Fig. 8, Panel (2-P3)	σ
1	35–40	7.370E−05	1.46E−05	1.304E−04	1.45E−05	1.175E−04	1.68E−05
2	40–45	6.358E−05	1.19E−05	1.121E−04	1.13E−05	8.116E−05	1.36E−05
3	45–55	4.598E−05	8.21E−06	8.459E−05	8.00E−06	6.533E−05	9.47E−06
4	55–73	2.703E−05	4.76E−06	5.456E−05	4.56E−06	4.388E−05	5.33E−06
5	73–98	1.952E−05	2.83E−06	2.958E−05	2.67E−06	2.929E−05	3.14E−06
6	98–123	1.341E−05	1.83E−06	2.027E−05	1.74E−06	1.980E−05	2.07E−06
7	123–162	8.199E−06	1.18E−06	1.179E−05	1.13E−06	1.372E−05	1.36E−06
8	162–230	5.173E−06	6.98E−07	6.603E−06	6.81E−07	7.458E−06	8.52E−07
9	230–313	2.830E−06	4.99E−07	3.119E−06	4.98E−07	3.833E−06	6.16E−07
10	313–429	1.153E−06	3.57E−07	1.711E−06	3.62E−07	1.761E−06	4.49E−07
11	429–595	7.140E−07	3.52E−07	6.586E−07	3.54E−07	7.776E−07	4.55E−07
12	595–766	3.444E−07	2.16E−07	5.030E−07	2.21E−07	1.081E−07	2.74E−07
13	766–1104	3.795E−07	1.68E−07	3.822E−07	1.68E−07	2.042E−09	2.06E−07
14	1104–1700	3.078E−07	1.18E−07	2.788E−07	1.17E−07	1.586E−07	1.45E−07
		4U 1543−45: FLUX ± σ (photons cm^{-2} s^{-1} keV^{-1})					
NUMBER	ENERGY (keV)	TJD: 8393–8800 Fig. 8, Panel (4 & 5-P1)	σ	TJD: 8800–9200 Fig. 8, Panel (4-P2)	σ	TJD: 9200–9628 Fig. 8, Panel (4-P3)	σ
1	35–40	1.513E−04	2.07E−05	1.577E−04	2.17E−05	1.354E−04	2.34E−05
2	40–45	9.896E−05	1.59E−05	1.176E−04	1.67E−05	1.064E−04	1.85E−05
3	45–55	7.129E−05	1.03E−05	9.122E−05	1.09E−05	7.356E−05	1.23E−05
4	55–73	4.124E−05	5.60E−06	6.031E−05	5.83E−06	4.031E−05	6.44E−06
5	73–98	2.308E−05	3.21E−06	3.384E−05	3.37E−06	2.609E−05	3.72E−06
6	98–123	1.600E−05	2.04E−06	1.886E−05	2.18E−06	1.874E−05	2.48E−06
7	123–162	1.015E−05	1.31E−06	1.216E−05	1.40E−06	1.313E−05	1.62E−06
8	162–230	5.281E−06	8.17E−07	6.380E−06	8.54E−07	8.326E−06	1.05E−06
9	230–313	3.517E−06	5.88E−07	3.039E−06	6.32E−07	5.822E−06	7.99E−07
10	313–429	2.772E−06	4.30E−07	2.179E−06	4.57E−07	4.761E−06	5.87E−07
11	429–595	2.254E−06	4.17E−07	2.541E−06	4.50E−07	4.685E−06	5.97E−07
12	595–766	1.047E−06	2.66E−07	1.663E−06	2.86E−07	2.711E−06	3.35E−07
13	766–1104	1.176E−06	1.98E−07	1.370E−06	2.16E−07	2.195E−06	2.69E−07
14	1104–1700	8.277E−07	1.34E−07	1.070E−06	1.48E−07	1.853E−06	1.90E−07
		4U 1608−522: FLUX ± σ (photons cm^{-2} s^{-1} keV^{-1})					
NUMBER	ENERGY (keV)	TJD: 8393–8800 Fig. 8, Panel (6-P1)	σ	TJD: 8800–9200 Fig. 8, Panel (6-P2)	σ	TJD: 9200–9628 Fig. 8, Panel (6-P3)	σ
1	35–40	4.784E−04	2.06E−05	2.711E−04	2.16E−05	1.745E−04	2.21E−05
2	40–45	3.582E−04	1.56E−05	2.166E−04	1.69E−05	1.317E−04	1.79E−05
3	45–55	2.640E−04	1.01E−05	1.557E−04	1.10E−05	9.857E−05	1.19E−05
4	55–73	1.582E−04	5.55E−06	9.138E−05	5.88E−06	6.778E−05	6.21E−06
5	73–98	7.911E−05	3.17E−06	4.531E−05	3.42E−06	4.112E−05	3.59E−06

TABLE 3—*Continued*

		4U 1608−522: Flux ± σ (photons cm^{-2} s^{-1} keV^{-1})					
Number	Energy (keV)	TJD: 8393–8800 Fig. 8, Panel (6-P1)	σ	TJD: 8800–9200 Fig. 8, Panel (6-P2)	σ	TJD: 9200–9628 Fig. 8, Panel (6-P3)	σ
6	98–123	4.348E−05	2.03E−06	3.097E−05	2.21E−06	2.526E−05	2.37E−06
7	123–162	2.659E−05	1.31E−06	1.816E−05	1.43E−06	1.626E−05	1.55E−06
8	162–230	1.472E−05	8.24E−07	1.126E−05	8.83E−07	1.011E−05	9.93E−07
9	230–313	9.611E−06	6.02E−07	7.264E−06	6.58E−07	7.593E−06	7.45E−07
10	313–429	6.844E−06	4.50E−07	4.845E−06	4.78E−07	5.569E−06	5.48E−07
11	429–595	5.993E−06	4.44E−07	4.295E−06	4.77E−07	5.350E−06	5.52E−07
12	595–766	3.239E−06	2.83E−07	2.415E−06	3.03E−07	2.472E−06	3.10E−07
13	766–1104	2.719E−06	2.20E−07	2.023E−06	2.31E−07	2.150E−06	2.49E−07
14	1104–1700	1.991E−06	1.54E−07	1.280E−06	1.60E−07	1.633E−06	1.74E−07
		4U 1700–37: Flux ± σ (photons cm^{-2} s^{-1} keV^{-1})					
Number	Energy (keV)	TJD: 8393–8800 Fig. 8, Panel (7-P1)	σ	TJD: 8800–9200 Fig. 8, Panel (7-P2)	σ	TJD: 9200–9628 Fig. 8, Panel (7-P3)	σ
1	35–40	1.025E−03	2.40E−05	1.128E−03	2.59E−05	1.072E−03	2.57E−05
2	40–45	7.744E−04	1.85E−05	7.902E−04	1.93E−05	8.131E−04	2.03E−05
3	45–55	4.892E−04	1.18E−05	5.389E−04	1.28E−05	5.294E−04	1.31E−05
4	55–73	2.420E−04	6.22E−06	2.428E−04	6.70E−06	2.527E−04	6.77E−06
5	73–98	1.009E−04	3.61E−06	9.384E−05	3.90E−06	1.055E−04	3.96E−06
6	98–123	4.344E−05	2.31E−06	3.990E−05	2.52E−06	4.413E−05	2.68E−06
7	123–162	1.754E−05	1.49E−06	1.319E−05	1.63E−06	1.589E−05	1.77E−06
8	162–230	6.719E−06	9.51E−07	5.795E−06	1.02E−06	6.224E−06	1.14E−06
9	230–313	4.439E−06	7.12E−07	1.698E−06	7.69E−07	3.310E−06	8.96E−07
10	313–429	2.771E−06	5.44E−07	1.036E−07	5.86E−07	2.980E−06	6.79E−07
11	429–595	2.648E−06	5.36E−07	5.647E−07	5.86E−07	1.501E−06	6.93E−07
12	595–766	1.391E−06	3.81E−07	4.914E−07	4.21E−07	1.009E−06	4.55E−07
13	766–1104	1.311E−06	2.91E−07	4.801E−09	3.17E−07	1.543E−06	3.72E−07
14	1104–1700	8.950E−07	1.99E−07	−4.123E−08	2.26E−07	8.433E−07	2.64E−07
		Aquila X-1: Flux ± σ (photons cm^{-2} s^{-1} keV^{-1})					
Number	Energy (keV)	TJD: 8396–8800 Fig. 8, Panel (8-P1)	σ	TJD: 8800–9200 Fig. 8, Panel (8-P2)	σ	TJD: 9200–9628 Fig. 8, Panel (8-P3)	σ
1	35–40	3.544E−04	1.93E−05	2.627E−04	1.94E−05	3.800E−04	2.01E−05
2	40–45	2.558E−04	1.59E−05	2.125E−04	1.51E−05	3.079E−04	1.68E−05
3	45–55	1.773E−04	1.10E−05	1.528E−04	1.06E−05	2.248E−04	1.14E−05
4	55–73	1.004E−04	6.00E−06	8.002E−05	5.91E−06	1.267E−04	6.34E−06
5	73–98	5.046E−05	3.46E−06	4.005E−05	3.49E−06	6.155E−05	3.76E−06
6	98–123	2.660E−05	2.24E−06	1.982E−05	2.27E−06	2.856E−05	2.54E−06
7	123–162	1.385E−05	1.43E−06	1.050E−05	1.46E−06	1.438E−05	1.65E−06
8	162–230	5.972E−06	8.65E−07	5.347E−06	8.81E−07	5.344E−06	1.03E−06
9	230–313	3.615E−06	6.30E−07	3.183E−06	6.50E−07	2.099E−06	7.80E−07
10	313–429	2.117E−06	4.68E−07	2.120E−06	4.83E−07	1.033E−06	5.92E−07
11	429–595	1.420E−06	4.54E−07	1.385E−06	4.65E−07	4.091E−07	5.87E−07
12	595–766	1.095E−06	2.94E−07	9.747E−07	3.05E−07	2.047E−07	3.59E−07
13	766–1104	8.669E−07	2.24E−07	6.747E−07	2.35E−07	4.081E−07	2.85E−07
14	1104–1700	5.605E−07	1.53E−07	6.353E−07	1.61E−07	4.973E−07	2.02E−07
		Cen A: Flux ± σ (photons cm^{-2} s^{-1} keV^{-1})					
Number	Energy (keV)	TJD: 8393–8800 Fig. 8, Panel (9-P1)	σ	TJD: 8800–9200 Fig. 8, Panel (9-P2)	σ	TJD: 9200–9628 Fig. 8, Panel (9-P3)	σ
1	35–40	5.875E−04	1.81E−05	3.450E−04	1.93E−05	3.371E−04	1.97E−05
2	40–45	4.592E−04	1.47E−05	2.723E−04	1.46E−05	2.821E−04	1.55E−05
3	45–55	3.549E−04	9.64E−06	2.166E−04	9.73E−06	2.179E−04	1.05E−05
4	55–73	2.273E−04	5.43E−06	1.472E−04	5.28E−06	1.409E−04	5.60E−06
5	73–98	1.338E−04	3.16E−06	8.873E−05	3.05E−06	8.473E−05	3.30E−06
6	98–123	8.602E−05	2.05E−06	5.227E−05	2.00E−06	5.290E−05	2.20E−06
7	123–162	5.053E−05	1.35E−06	3.131E−05	1.29E−06	3.338E−05	1.46E−06
8	162–230	2.600E−05	8.39E−07	1.677E−05	7.88E−07	1.800E−05	9.59E−07
9	230–313	1.369E−05	6.19E−07	9.646E−06	5.73E−07	1.069E−05	7.17E−07
10	313–429	7.696E−06	4.65E−07	5.199E−06	4.08E−07	7.291E−06	5.25E−07
11	429–595	5.526E−06	4.67E−07	3.556E−06	4.05E−07	6.319E−06	5.24E−07

TABLE 3—*Continued*

		Cen A: Flux ± σ (photons cm^{-2} s^{-1} keV^{-1})					
Number	Energy (keV)	TJD: 8393–8800 Fig. 8, Panel (9-P1)	σ	TJD: 8800–9200 Fig. 8, Panel (9-P2)	σ	TJD: 9200–9628 Fig. 8, Panel (9-P3)	σ
12	595–766	2.720E−06	2.93E−07	2.303E−06	2.54E−07	3.602E−06	3.12E−07
13	766–1104	1.955E−06	2.35E−07	1.926E−06	1.93E−07	3.128E−06	2.36E−07
14	1104–1700	1.743E−06	1.68E−07	1.270E−06	1.34E−07	2.467E−06	1.69E−07

		Cir X-1: Flux ± σ (photons cm^{-2} s^{-1} keV^{-1})					
Number	Energy (keV)	TJD: 8393–8800 Fig. 8, Panel (10-P1)	σ	TJD: 8800–9200 Fig. 8, Panel (10-P2)	σ	TJD: 9200–9628 Fig. 8, Panel (10-P3)	σ
1	35–40	1.291E−04	2.23E−05	1.142E−04	1.80E−05	1.097E−04	1.94E−05
2	40–45	9.961E−05	1.70E−05	8.702E−05	1.80E−05	1.097E−04	1.94E−05
3	45–55	7.866E−05	1.11E−05	7.671E−05	1.21E−05	6.658E−05	1.29E−05
4	55–73	5.428E−05	6.14E−06	4.788E−05	6.53E−06	5.250E−05	6.67E−06
5	73–98	3.448E−05	3.50E−06	2.746E−05	3.84E−06	3.046E−05	3.90E−06
6	98–123	2.481E−05	2.22E−06	1.912E−05	2.44E−06	2.301E−05	2.59E−06
7	123–162	1.660E−05	1.42E−06	1.273E−05	1.57E−06	1.555E−05	1.71E−06
8	162–230	1.010E−05	8.82E−07	8.157E−06	9.67E−07	9.623E−06	1.10E−06
9	230–313	6.618E−06	6.46E−07	4.989E−06	7.18E−07	7.179E−06	8.37E−07
10	313–429	4.326E−06	4.80E−07	3.838E−06	5.29E−07	5.499E−06	6.12E−07
11	429–595	4.266E−06	4.58E−07	2.710E−06	5.25E−07	5.577E−06	6.13E−07
12	595–766	2.411E−06	2.94E−07	1.229E−06	3.32E−07	2.875E−06	3.36E−07
13	766–1104	2.345E−06	2.22E−07	1.221E−06	2.47E−07	2.369E−06	2.68E−07
14	1104–1700	1.132E−06	1.51E−07	8.981E−07	1.70E−07	1.680E−06	1.87E−07

		Crab: Flux ± σ (photons cm^{-2} s^{-1} keV^{-1})					
Number	Energy (keV)	TJD: 8400–8796 Fig. 8, Panel (11-P1)	σ	TJD: 8810–9193 Fig. 8, Panel (11-P2)	σ	TJD: 9203–9628 Fig. 8, Panel (11-P3)	σ
1	35–40	5.434E−03	1.96E−05	5.118E−03	1.83E−05	5.283E−03	1.98E−05
2	40–45	3.923E−03	1.56E−05	4.073E−03	1.55E−05	3.992E−03	1.58E−05
3	45–55	3.099E−03	1.15E−05	2.935E−03	1.11E−05	3.051E−03	1.19E−05
4	55–73	1.803E−03	6.78E−06	1.778E−03	6.37E−06	1.784E−03	6.99E−06
5	73–98	9.874E−04	4.06E−06	9.791E−04	3.78E−06	9.822E−04	4.16E−06
6	98–123	5.558E−04	2.71E−06	5.531E−04	2.58E−06	5.596E−04	2.81E−06
7	123–162	3.174E−04	1.70E−06	3.111E−04	1.66E−06	3.163E−04	1.85E−06
8	162–230	1.479E−04	1.00E−06	1.470E−04	1.01E−06	1.494E−04	1.16E−06
9	230–313	6.955E−05	7.49E−07	7.014E−05	7.55E−07	6.910E−05	8.67E−07
10	313–429	3.173E−05	5.60E−07	3.235E−05	5.68E−07	3.195E−05	6.47E−07
11	429–595	1.657E−05	5.82E−07	1.689E−05	5.76E−07	1.704E−05	6.59E−07
12	595–766	7.983E−06	3.97E−07	7.919E−06	4.03E−07	7.987E−06	4.36E−07
13	766–1104	4.597E−06	3.11E−07	4.661E−06	3.26E−07	4.786E−06	3.52E−07
14	1104–1700	2.109E−06	2.30E−07	2.321E−06	2.32E−07	2.368E−06	2.58E−07

		Crab: Flux ± σ (photons cm^{-2} s^{-1} keV^{-1})			
Number	Energy (keV)	TJD: 9070–9074 Fig. 8, Panel (12)	σ	TJD: 9121–9130 Fig. 8, Panel (13)	σ
1	35–40	4.777E−03	1.43E−04	4.768E−03	1.02E−04
2	40–45	3.993E−03	1.15E−04	3.982E−03	8.40E−05
3	45–55	2.700E−03	8.62E−05	2.576E−03	5.31E−05
4	55–73	1.659E−03	4.56E−05	1.621E−03	2.80E−05
5	73–98	9.294E−04	2.78E−05	9.145E−04	1.68E−05
6	98–123	5.099E−04	1.81E−05	5.102E−04	1.11E−05
7	123–162	2.953E−04	1.18E−05	2.927E−04	6.90E−06
8	162–230	1.324E−04	7.14E−06	1.374E−04	3.92E−06
9	230–313	6.146E−05	5.01E−06	6.371E−05	2.71E−06
10	313–429	3.346E−05	3.78E−06	2.988E−05	2.01E−06
11	429–595	1.492E−05	3.41E−06	1.712E−05	1.98E−06
12	595–766	4.969E−06	2.05E−06	6.734E−06	1.38E−06
13	766–1104	1.037E−06	1.91E−06	3.968E−06	1.05E−06
14	1104–1700	1.320E−06	1.13E−06	1.553E−06	7.38E−07

TABLE 3—*Continued*

		Cygnus X-1: Flux ± σ (photons cm^{-2} s^{-1} keV^{-1})					
Number	Energy (keV)	TJD: 8393–8800 Fig. 8, Panel (14-P1)	σ	TJD: 8800–9200 Fig. 8, Panel (14-P2)	σ	TJD: 9200–9628 Fig. 8, Panel (14-P3)	σ
1	35–40	4.805E−03	1.92E−05	4.837E−03	1.81E−05	4.174E−03	2.17E−05
2	40–45	3.923E−03	1.58E−05	3.758E−03	1.43E−05	3.314E−03	1.77E−05
3	45–55	3.034E−03	1.10E−05	3.015E−03	1.00E−05	2.526E−03	1.22E−05
4	55–73	1.986E−03	6.21E−06	1.923E−03	5.89E−06	1.569E−03	6.75E−06
5	73–98	1.197E−03	3.65E−06	1.122E−03	3.54E−06	8.827E−04	4.06E−06
6	98–123	7.066E−04	2.38E−06	6.493E−04	2.37E−06	5.010E−04	2.72E−06
7	123–162	3.972E−04	1.54E−06	3.578E−04	1.56E−06	2.675E−04	1.77E−06
8	162–230	1.733E−04	9.31E−07	1.520E−04	9.41E−07	1.153E−04	1.12E−06
9	230–313	6.894E−05	6.74E−07	6.009E−05	7.00E−07	4.464E−05	8.38E−07
10	313–429	2.463E−05	5.00E−07	2.033E−05	5.23E−07	1.695E−05	6.28E−07
11	429–595	9.118E−06	4.96E−07	7.717E−06	5.34E−07	6.676E−06	6.22E−07
12	595–766	3.206E−06	3.30E−07	2.636E−06	3.55E−07	2.619E−06	4.01E−07
13	766–1104	1.657E−06	2.61E−07	1.205E−06	2.86E−07	1.596E−06	3.17E−07
14	1104–1700	1.058E−06	1.86E−07	5.758E−07	2.05E−07	8.799E−07	2.38E−07

		Cygnus X-1: Flux ± σ (photons cm^{-2} s^{-1} keV^{-1})	
Number	Energy (keV)	TJD: 8407–9545 Fig. 8, Panel (15)	σ
1	24–31	8.427E−03	8.05E−05
2	31–41	5.313E−03	3.58E−05
3	41–55	3.078E−03	1.81E−05
4	55–73	1.840E−03	1.00E−05
5	73–98	1.097E−03	6.03E−06
6	98–123	6.514E−04	4.12E−06
7	123–162	3.634E−04	2.76E−06
8	162–230	1.607E−04	1.70E−06
9	230–313	5.754E−05	1.22E−06
10	313–429	2.035E−05	9.34E−07
11	429–595	6.130E−06	8.51E−07
12	595–766	2.494E−06	6.15E−07
13	766–1104	7.332E−07	4.38E−07
14	1104–1700	1.743E−07	1.96E−07

		Cygnus X-1: Flux ± σ (photons cm^{-2} s^{-1} keV^{-1})			
Number	Energy (keV)	TJD: 8407–8414 Fig. 8, Panel (16)	σ	TJD: 8416–8421 Fig. 8, Panel (17)	σ
1	35–40	3.969E−03	1.88E−04	4.389E−03	2.30E−04
2	40–45	3.473E−03	1.50E−04	3.416E−03	2.01E−04
3	45–55	2.442E−03	9.84E−05	2.466E−03	1.43E−04
4	55–73	1.699E−03	5.25E−05	1.601E−03	8.79E−05
5	73–98	1.061E−03	2.98E−05	9.566E−04	5.38E−05
6	98–123	6.316E−04	1.89E−05	5.959E−04	3.50E−05
7	123–162	3.796E−04	1.29E−05	3.516E−04	2.18E−05
8	162–230	1.810E−04	7.86E−06	1.527E−04	1.33E−05
9	230–313	7.132E−05	5.55E−06	5.719E−05	1.36E−05
10	313–429	2.407E−05	4.20E−06	2.342E−05	8.99E−06
11	429–595	1.745E−06	4.08E−06	9.086E−06	9.42E−06
12	595–766	1.795E−06	2.93E−06	−8.251E−07	7.06E−06
13	766–1104	2.405E−07	2.21E−06	8.617E−07	4.62E−06
14	1104–1700	−1.208E−07	1.04E−06	3.170E−06	2.71E−06

		Cygnus X-1: Flux ± σ (photons cm^{-2} s^{-1} keV^{-1})			
Number	Energy (keV)	TJD: 8477–8482 Fig. 8, Panel (18)	σ	TJD: 8589–8601 Fig. 8, Panel (19)	σ
1	35–40	4.476E−03	1.63E−04	4.806E−03	8.62E−05
2	40–45	3.999E−03	1.29E−04	4.296E−03	6.89E−05
3	45–55	2.792E−03	7.70E−05	3.000E−03	4.55E−05
4	55–73	1.937E−03	4.11E−05	2.102E−03	2.51E−05
5	73–98	1.195E−03	2.60E−05	1.312E−03	1.50E−05
6	98–123	7.336E−04	1.71E−05	7.911E−04	9.83E−06
7	123–162	4.128E−04	1.18E−05	4.568E−04	6.34E−06

TABLE 3—*Continued*

		Cygnus X-1: Flux ± σ (photons cm^{-2} s^{-1} keV^{-1})			
Number	Energy (keV)	TJD: 8477–8482 Fig. 8, Panel (18)	σ	TJD: 8589–8601 Fig. 8, Panel (19)	σ
8	162–230	1.903E−04	8.13E−06	2.126E−04	4.13E−06
9	230–313	7.376E−05	5.39E−06	8.182E−05	2.72E−06
10	313–429	2.826E−05	3.57E−06	3.100E−05	1.93E−06
11	429–595	6.658E−06	3.62E−06	1.186E−05	1.95E−06
12	595–766	2.607E−06	2.56E−06	4.617E−06	1.30E−06
13	766–1104	1.071E−06	1.71E−06	2.952E−06	8.88E−07
14	1104–1700	3.984E−07	8.27E−07	1.226E−06	4.98E−07

		Cygnus X-1: Flux ± σ (photons cm^{-2} s^{-1} keV^{-1})					
Number	Energy (keV)	TJD: 8972–8977 Fig. 8, Panel (20)	σ	TJD: 9028–9039 Fig. 8, Panel (21)	σ	TJD: 9056–9068 Fig. 8, Panel (22)	σ
1	35–40	5.554E−03	1.69E−04	4.812E−03	1.30E−04	4.322E−03	1.52E−04
2	40–45	4.874E−03	1.36E−04	4.296E−03	1.06E−04	4.059E−03	1.29E−04
3	45–55	3.433E−03	8.64E−05	2.940E−03	6.84E−05	2.764E−03	8.02E−05
4	55–73	2.352E−03	4.80E−05	2.052E−03	3.40E−05	1.928E−03	3.89E−05
5	73–98	1.446E−03	2.88E−05	1.231E−03	1.93E−05	1.176E−03	2.24E−05
6	98–123	8.404E−04	1.88E−05	7.250E−04	1.31E−05	7.033E−04	1.43E−05
7	123–162	4.838E−04	1.23E−05	3.962E−04	8.83E−06	3.915E−04	1.02E−05
8	162–230	2.067E−04	7.90E−06	1.816E−04	5.93E−06	1.842E−04	5.34E−06
9	230–313	7.443E−05	5.73E−06	7.739E−05	4.01E−06	6.964E−05	4.01E−06
10	313–429	2.337E−05	4.28E−06	2.843E−05	3.00E−06	2.739E−05	2.97E−06
11	429–595	1.090E−05	3.82E−06	1.197E−05	2.81E−06	9.639E−06	2.70E−06
12	595–766	9.547E−06	2.90E−06	2.518E−06	2.23E−06	2.837E−06	2.08E−06
13	766–1104	3.158E−06	2.06E−06	−1.284E−06	1.48E−06	1.350E−06	1.55E−06
14	1104–1700	2.145E−06	7.92E−07	−1.196E−07	9.07E−07	9.307E−08	7.41E−07

		Cygnus X-1: Flux ± σ (photons cm^{-2} s^{-1} keV^{-1})					
Number	Energy (keV)	TJD: 9121–9130 Fig. 8, Panel (23)	σ	TJD: 9139–9140 Fig. 8, Panel (24)	σ	TJD: 9253–9260 Fig. 8, Panel (25)	σ
1	35–40	4.068E−03	1.44E−04	3.814E−03	2.63E−04	4.915E−03	1.43E−04
2	40–45	3.285E−03	1.23E−04	3.547E−03	2.17E−04	3.548E−03	1.01E−04
3	45–55	2.437E−03	8.32E−05	2.294E−03	1.05E−04	2.807E−03	7.37E−05
4	55–73	1.501E−03	4.93E−05	1.618E−03	4.42E−05	1.684E−03	3.71E−05
5	73–98	9.405E−04	2.87E−05	9.907E−04	3.23E−05	9.597E−04	2.07E−05
6	98–123	5.870E−04	2.00E−05	6.175E−04	3.00E−05	5.305E−04	1.61E−05
7	123–162	3.340E−04	1.32E−05	3.557E−04	1.90E−05	2.724E−04	9.88E−06
8	162–230	1.506E−04	7.91E−06	1.607E−04	1.14E−05	1.120E−04	5.58E−06
9	230–313	5.875E−05	6.90E−06	6.597E−05	8.71E−06	4.279E−05	4.30E−06
10	313–429	2.085E−05	5.61E−06	3.033E−05	7.03E−06	1.537E−05	3.86E−06
11	429–595	1.125E−05	5.78E−06	1.372E−05	6.68E−06	6.386E−06	3.11E−06
12	595–766	7.442E−06	4.50E−06	7.566E−06	4.32E−06	3.114E−06	2.71E−06
13	766–1104	−4.090E−06	3.05E−06	2.554E−06	3.38E−06	1.405E−06	1.98E−06
14	1104–1700	−2.712E−06	1.79E−06	2.439E−06	2.16E−06	1.445E−06	9.48E−07

		Cygnus X-1: Flux ± σ (photons cm^{-2} s^{-1} keV^{-1})					
Number	Energy (keV)	TJD: 9262–9263 Fig. 8, Panel (26)	σ	TJD: 9385–9390 Fig. 8, Panel (27)	σ	TJD: 9497–9502 Fig. 8, Panel (28)	σ
1	35–40	5.413E−03	3.19E−04	1.567E−03	1.72E−04	5.060E−03	1.95E−04
2	40–45	4.241E−03	2.55E−04	1.049E−03	1.31E−04	4.407E−03	1.48E−04
3	45–55	3.204E−03	1.94E−04	6.831E−04	8.26E−05	3.124E−03	1.05E−04
4	55–73	1.832E−03	9.30E−05	3.497E−04	4.38E−05	2.028E−03	5.57E−05
5	73–98	9.839E−04	5.73E−05	1.925E−04	2.75E−05	1.253E−03	3.67E−05
6	98–123	5.343E−04	4.15E−05	9.501E−05	1.95E−05	7.448E−04	2.37E−05
7	123–162	2.877E−04	2.75E−05	3.536E−05	1.33E−05	4.027E−04	1.59E−05
8	162–230	8.641E−05	1.42E−05	2.657E−05	9.21E−06	1.696E−04	1.09E−05
9	230–313	4.468E−05	1.27E−05	8.413E−06	6.34E−06	5.308E−05	6.48E−06
10	313–429	1.906E−06	1.11E−05	5.648E−06	4.74E−06	1.853E−05	4.67E−06
11	429–595	8.777E−06	9.16E−06	2.973E−06	4.84E−06	6.700E−06	4.51E−06
12	595–766	4.004E−06	6.30E−06	6.401E−07	3.62E−06	1.005E−06	2.57E−06
13	766–1104	−2.805E−06	7.23E−06	2.041E−06	3.17E−06	−1.373E−06	1.81E−06
14	1104–1700	−1.148E−06	2.03E−06	1.899E−06	2.22E−06	−1.744E−07	7.94E−07

TABLE 3—*Continued*

		Cygnus X-1: Flux ± σ (photons cm^{-2} s^{-1} keV^{-1})					
Number	Energy (keV)	TJD: 9262–9263 Fig. 8, Panel (26)	σ	TJD: 9385–9390 Fig. 8, Panel (27)	σ	TJD: 9497–9502 Fig. 8, Panel (28)	σ
		Cygnus X-1: Flux ± σ (photons cm^{-2} s^{-1} keV^{-1})					
Number	Energy (keV)	TJD: 9511–9512 Fig. 8, Panel (29)	σ	TJD: 9522–9537 Fig. 8, Panel (30)	σ	TJD: 9539–9544 Fig. 8, Panel (31)	σ
1	35–40	2.726E−03	3.88E−04	4.308E−03	1.21E−04	4.220E−03	1.81E−04
2	40–45	2.551E−03	3.31E−04	3.934E−03	9.51E−05	2.563E−03	8.78E−05
3	45–55	1.652E−03	1.99E−04	2.573E−03	6.59E−05	2.563E−03	8.78E−05
4	55–73	1.206E−03	1.64E−04	1.749E−03	3.37E−05	1.779E−03	4.18E−05
5	73–98	7.390E−04	6.95E−05	1.004E−03	2.10E−05	1.036E−03	2.57E−05
6	98–123	4.302E−04	5.27E−05	5.608E−04	1.38E−05	5.972E−04	1.70E−05
7	123–162	2.365E−04	3.54E−05	2.903E−04	9.51E−06	3.239E−04	1.21E−05
8	162–230	9.433E−05	1.37E−05	1.275E−04	7.07E−06	1.459E−04	8.04E−06
9	230–313	3.307E−05	8.19E−06	4.646E−05	5.64E−06	5.731E−05	5.29E−06
10	313–429	8.799E−06	6.84E−06	1.529E−05	4.05E−06	3.188E−05	3.98E−06
11	429–595	2.375E−06	4.72E−06	6.607E−06	3.74E−06	1.741E−05	4.12E−06
12	595–766	6.106E−06	6.16E−06	2.883E−06	3.17E−06	7.686E−06	3.26E−06
13	766–1104	4.552E−06	3.06E−06 -	1.814E−06	1.96E−06	5.908E−06	2.46E−06
14	1104–1700	1.785E−06	1.80E−06	1.806E−07	1.03E−06	4.962E−06	1.65E−06
		Cygnus X-3: Flux ± σ (photons cm^{-2} s^{-1} keV^{-1})					
Number	Energy (keV)	TJD: 8393–8800 Fig. 8, Panel (32 & 33-P1)	σ	TJD: 8800–9200 Fig. 8, Panel (32-P2)	σ	TJD: 9200–9622 Fig. 8, Panel (32-P3)	σ
1	35–40	4.651E−04	1.95E−05	4.741E−04	1.96E−05	5.217E−04	2.28E−05
2	40–45	3.327E−04	1.64E−05	2.952E−04	1.54E−05	3.565E−04	1.85E−05
3	45–55	2.052E−04	1.15E−05	2.007E−04	1.09E−05	2.359E−04	1.29E−05
4	55–73	8.451E−05	6.53E−06	8.994E−05	6.38E−06	1.016E−04	7.21E−06
5	73–98	2.783E−05	3.85E−06	3.098E−05	3.85E−06	3.224E−05	4.32E−06
6	98–123	8.549E−06	2.51E−06	1.306E−05	2.58E−06	1.484E−05	2.87E−06
7	123–162	3.277E−06	1.62E−06	6.208E−06	1.69E−06	8.900E−06	1.86E−06
8	162–230	1.260E−06	9.81E−07	2.514E−06	1.03E−06	1.775E−06	1.17E−06
9	230–313	2.300E−07	7.15E−07	6.367E−07	7.74E−07	1.732E−06	8.52E−07
10	313–429	3.975E−07	5.26E−07	8.171E−07	5.79E−07	1.281E−06	6.28E−07
11	429–595	4.160E−07	5.16E−07	−8.712E−07	5.79E−07	7.765E−07	6.12E−07
12	595–766	1.828E−07	3.39E−07	−1.728E−08	3.82E−07	5.176E−08	3.75E−07
13	766–1104	3.121E−07	2.62E−07	−1.486E−07	2.97E−07	3.514E−07	2.94E−07
14	1104–1700	2.277E−07	1.78E−07	1.880E−07	2.12E−07	1.877E−07	2.08E−07
		EXO 1846−31: Flux ± σ (photons cm^{-2} s^{-1} keV^{-1})					
Number	Energy (keV)	TJD: 8393–8800 Fig. 8, Panel (34-P1)	σ	TJD: 8801–9200 Fig. 8, Panel (34-P2)	σ	TJD: 9200–9628 Fig. 8, Panel (34-P3)	σ
1	35–40	2.611E−04	2.06E−05	2.466E−04	2.11E−05	2.767E−04	2.13E−05
2	40–45	1.996E−04	1.65E−05	1.935E−04	1.63E−05	2.155E−04	1.77E−05
3	45–55	1.342E−04	1.14E−05	1.414E−04	1.13E−05	1.630E−04	1.20E−05
4	55–73	8.538E−05	6.19E−06	7.985E−05	6.19E−06	9.403E−05	6.61E−06
5	73–98	4.154E−05	3.56E−06	4.034E−05	3.64E−06	4.400E−05	3.88E−06
6	98–123	2.375E−05	2.28E−06	2.164E−05	2.34E−06	2.461E−05	2.61E−06
7	123–162	1.158E−05	1.45E−06	1.244E−05	1.51E−06	1.337E−05	1.69E−06
8	162–230	6.294E−06	8.81E−07	7.073E−06	9.14E−07	6.626E−06	1.04E−06
9	230–313	3.515E−06	6.38E−07	3.664E−06	6.69E−07	3.958E−06	7.81E−07
10	313–429	1.950E−06	4.69E−07	2.065E−06	4.95E−07	1.830E−06	5.87E−07
11	429–595	1.357E−06	4.53E−07	1.729E−06	4.72E−07	1.560E−06	5.75E−07
12	595–766	9.425E−07	2.94E−07	8.824E−07	3.08E−07	8.650E−07	3.45E−07
13	766–1104	6.260E−07	2.25E−07	7.224E−07	2.38E−07	6.643E−07	2.76E−07
14	1104–1700	4.701E−07	1.47E−07	4.849E−07	1.62E−07	5.919E−07	1.96E−07
		GRO J0422+32: Flux ± σ (photons cm^{-2} s^{-1} keV^{-1})					
Number	Energy (keV)	TJD: 8393–8800 Fig. 8, Panel (35-P1)		TJD: 8800–9200 Fig. 8, Panel (35-P2)		TJD: 9203–9628 Fig. 8, Panel (35-P3)	
1	35–40	1.838E−05	1.23E−05	1.323E−03	1.32E−05	3.622E−05	1.45E−05
2	40–45	2.714E−05	1.02E−05	1.066E−03	1.09E−05	1.428E−05	1.21E−05

TABLE 3—*Continued*

		GRO J0422+32: Flux ± σ (photons cm^{-2} s^{-1} keV^{-1})					
	Energy	TJD: 8393–8800		TJD: 8800–9200		TJD: 9203–9628	
Number	(keV)	Fig. 8, Panel (35-P1)		Fig. 8, Panel (35-P2)		Fig. 8, Panel (35-P3)	
3	45–55	2.247E−05	7.63E−06	8.716E−04	8.01E−06	1.800E−05	9.16E−06
4	55–73	1.170E−05	4.58E−06	5.218E−04	4.73E−06	1.508E−05	5.56E−06
5	73–98	8.512E−06	2.71E−06	3.129E−04	2.84E−06	9.566E−06	3.27E−06
6	98–123	6.164E−06	1.75E−06	1.943E−04	1.91E−06	6.894E−06	2.15E−06
7	123–162	3.283E−06	1.09E−06	1.058E−04	1.22E−06	2.382E−06	1.39E−06
8	162–230	1.730E−06	6.18E−07	4.972E−05	7.12E−07	9.371E−07	8.33E−07
9	230–313	1.018E−06	4.35E−07	1.943E−05	5.09E−07	7.357E−07	5.91E−07
10	313–429	2.641E−07	3.08E−07	6.149E−06	3.66E−07	4.382E−08	4.10E−07
11	429–595	3.767E−07	3.01E−07	2.218E−06	3.65E−07	−6.456E−08	4.02E−07
12	595–766	1.820E−07	1.80E−07	2.201E−07	2.35E−07	−1.937E−07	2.39E−07
13	766–1104	1.466E−07	1.40E−07	−3.909E−08	1.89E−07	−2.130E−07	1.76E−07
14	1104–1700	3.135E−07	9.64E−08	1.505E−07	1.32E−07	−1.832E−07	1.28E−07

		GRO J0422+32: Flux ± σ (photons cm^{-2} s^{-1} keV^{-1})					
	Energy	TJD: 8847–8853		TJD: 8855–8860		TJD: 8867–8881	
Number	(keV)	Fig. 8, Panel (36)	σ	Fig. 8, Panel (37)	σ	Fig. 8, Panel (38)	σ
1	35–40	1.351E−02	2.27E−04	1.302E−02	1.82E−04	8.109E−03	1.13E−04
2	40–45	1.137E−02	1.90E−04	1.199E−02	1.48E−04	7.080E−03	9.81E−05
3	45–55	8.488E−03	1.41E−04	8.082E−03	1.02E−04	5.160E−03	6.92E−05
4	55–73	5.761E−03	7.52E−05	5.827E−03	5.30E−05	3.537E−03	3.73E−05
5	73–98	3.522E−03	4.60E−05	3.563E−03	3.49E−05	2.218E−03	2.15E−05
6	98–123	2.030E−03	2.97E−05	2.048E−03	2.30E−05	1.338E−03	1.51E−05
7	123–162	1.077E−03	1.86E−05	1.071E−03	1.42E−05	7.574E−04	1.03E−05
8	162–230	4.362E−04	1.07E−05	4.432E−04	8.09E−06	3.289E−04	6.30E−06
9	230–313	1.330E−04	6.14E−06	1.400E−04	5.83E−06	1.156E−04	3.68E−06
10	313–429	3.389E−05	3.68E−06	5.331E−05	4.53E−06	3.791E−05	2.44E−06
11	429–595	1.295E−06	3.82E−06	1.337E−05	3.68E−06	9.747E−06	2.22E−06
12	595–766	−6.263E−07	2.09E−06	5.582E−06	3.64E−06	2.123E−06	1.32E−06
13	766–1104	−2.551E−06	1.40E−06	3.350E−06	1.82E−06	5.795E−07	1.04E−06
14	1104–1700	−1.307E−06	5.40E−07	1.518E−06	8.11E−07	−1.847E−07	4.63E−07

		GRO J0422+32: Flux ± σ (photons cm^{-2} s^{-1} keV^{-1})	
	Energy	TJD: 8853–8891	
Number	(keV)	Fig. 8, Panel (39)	σ
1	24–31	1.772E−02	1.60E−04
2	31–41	1.023E−02	6.31E−05
3	41–55	6.171E−03	3.59E−05
4	55–73	3.752E−03	2.10E−05
5	73–98	2.272E−03	1.25E−05
6	98–123	1.318E−03	8.17E−06
7	123–162	7.272E−04	5.28E−06
8	162–230	3.034E−04	2.90E−06
9	230–313	1.073E−04	2.01E−06
10	313–429	3.817E−05	1.47E−06
11	429–595	1.267E−05	1.50E−06
12	595–766	4.526E−06	9.78E−07
13	766–1104	2.288E−06	8.07E−07
14	1104–1700	1.379E−06	6.09E−07

		GRO J1719−24: Flux ± σ (photons cm^{-2} s^{-1} keV^{-1})					
	Energy	TJD: 8393–8800		TJD: 8800–9200		TJD: 9200–9628	
Number	(keV)	Fig. 8, Panel (40-P1)	σ	Fig. 8, Panel (40 & 41-P2)	σ	Fig. 8, Panel (40-P3)	σ
1	35–40	1.381E−04	2.12E−05	9.033E−05	2.10E−05	8.146E−04	2.37E−05
2	40–45	1.060E−04	1.66E−05	6.242E−05	1.60E−05	7.324E−04	1.89E−05
3	45–55	6.195E−05	1.08E−05	4.354E−05	1.09E−05	5.593E−04	1.23E−05
4	55–73	2.584E−05	5.80E−06	2.476E−05	5.93E−06	3.638E−04	6.52E−06
5	73–98	6.872E−06	3.34E−06	1.299E−05	3.41E−06	2.089E−04	3.81E−06
6	98–123	1.230E−06	2.14E−06	5.906E−06	2.20E−06	1.096E−04	2.53E−06
7	123–162	−4.880E−07	1.36E−06	3.395E−06	1.38E−06	5.113E−05	1.65E−06
8	162–230	−6.339E−07	8.34E−07	2.680E−06	8.13E−07	1.850E−05	1.02E−06
9	230–313	−6.764E−07	6.06E−07	1.467E−06	5.82E−07	6.336E−06	7.64E−07

TABLE 3—*Continued*

		GRO J1719−24: Flux ± σ (photons cm^{-2} s^{-1} keV^{-1})					
		TJD: 8393–8800		TJD: 8800–9200		TJD: 9200–9628	
Number	Energy (keV)	Fig. 8, Panel (40-P1)	σ	Fig. 8, Panel (40 & 41-P2)	σ	Fig. 8, Panel (40-P3)	σ
10	313–429	−7.156E−07	4.45E−07	4.442E−07	4.19E−07	1.836E−06	5.57E−07
11	429–595	−8.948E−07	4.27E−07	6.129E−08	3.93E−07	8.628E−07	5.43E−07
12	595–766	−9.119E−07	2.83E−07	1.323E−08	2.57E−07	−8.090E−07	3.31E−07
13	766–1104	−7.417E−07	2.09E−07	−2.642E−07	1.89E−07	−1.859E−07	2.62E−07
14	1104–1700	−5.598E−07	1.40E−07	−4.502E−08	1.30E−07	−2.065E−07	1.77E−07

		GRO J1719−24: Flux ± σ (photons cm^{-2} s^{-1} keV^{-1})	
		TJD: 9257–9332	
Number	Energy (keV)	Fig. 8, Panel (41)	σ
1	35–40	6.085E−03	7.64E−05
2	40–45	5.137E−03	5.83E−05
3	45–55	3.613E−03	3.60E−05
4	55–73	2.269E−03	1.82E−05
5	73–98	1.238E−03	1.03E−05
6	98–123	6.469E−04	6.94E−06
7	123–162	3.095E−04	4.59E−06
8	162–230	1.112E−04	2.88E−06
9	230–313	3.671E−05	2.21E−06
10	313–429	1.269E−05	1.66E−06
11	429–595	6.541E−06	1.63E−06
12	595–766	1.876E−06	1.22E−06
13	766–1104	1.094E−06	8.54E−07
14	1104–1700	1.310E−06	6.15E−07

		GRS 0834−430: Flux ± σ (photons cm^{-2} s^{-1} keV^{-1})					
		TJD: 8393–8800		TJD: 8800–9200		TJD: 9200–9628	
Number	Energy (keV)	Fig. 8, Panel (42-P1)	σ	Fig. 8, Panel (42-P2)	σ	Fig. 8, Panel (42-P3)	σ
1	35–40	3.848E−04	1.52E−05	2.152E−04	1.56E−05	2.853E−05	1.54E−05
2	40–45	2.506E−04	1.19E−05	1.334E−04	1.22E−05	1.799E−05	1.34E−05
3	45–55	1.500E−04	8.49E−06	7.363E−05	8.01E−06	2.073E−05	9.32E−06
4	55–73	4.695E−05	4.65E−06	1.683E−05	4.41E−06	2.382E−05	5.24E−06
5	73–98	3.240E−06	2.76E−06	1.655E−06	2.61E−06	9.881E−06	3.12E−06
6	98–123	2.147E−06	1.83E−06	2.444E−06	1.70E−06	8.872E−06	2.05E−06
7	123–162	1.877E−06	1.17E−06	2.996E−06	1.12E−06	8.274E−06	1.35E−06
8	162–230	2.856E−06	7.16E−07	3.955E−06	6.86E−07	5.823E−06	8.46E−07
9	230–313	1.905E−06	5.19E−07	3.302E−06	4.99E−07	4.313E−06	6.26E−07
10	313–429	1.160E−06	3.77E−07	2.253E−06	3.63E−07	2.680E−06	4.58E−07
11	429–595	8.692E−07	3.70E−07	2.295E−06	3.67E−07	2.252E−06	4.53E−07
12	595–766	5.162E−07	2.33E−07	1.080E−06	2.28E−07	1.119E−06	2.60E−07
13	766–1104	5.576E−07	1.83E−07	1.130E−06	1.74E−07	1.165E−06	2.13E−07
14	1104–1700	4.643E−07	1.27E−07	8.177E−07	1.23E−07	9.440E−07	1.45E−07

		GRS 1009−45: Flux ± σ (photons cm^{-2} s^{-1} keV^{-1})					
		TJD: 8393–8800		TJD: 8800–9200		TJD: 9200–9628	
Number	Energy (keV)	Fig. 8, Panel (43-P1)	σ	Fig. 8, Panel (43-P2)	σ	Fig. 8, Panel (43-P3)	σ
1	35–40	8.395E−05	1.50E−05	4.956E−05	1.66E−05	2.816E−04	1.78E−05
2	40–45	6.594E−05	1.20E−05	3.774E−05	1.27E−05	2.574E−04	1.49E−05
3	45–55	5.854E−05	8.43E−06	3.765E−05	8.40E−06	1.854E−04	1.03E−05
4	55–73	4.145E−05	4.66E−06	2.757E−05	4.59E−06	1.182E−04	5.74E−06
5	73–98	2.505E−05	2.76E−06	1.234E−05	2.71E−06	6.486E−05	3.36E−06
6	98–123	1.566E−05	1.80E−06	1.063E−05	1.77E−06	3.416E−05	2.24E−06
7	123–162	8.904E−06	1.17E−06	5.486E−06	1.17E−06	2.041E−05	1.48E−06
8	162–230	4.531E−06	7.13E−07	2.196E−06	7.12E−07	9.292E−06	9.50E−07
9	230–313	3.765E−06	5.16E−07	1.185E−06	5.14E−07	3.367E−06	6.99E−07
10	313–429	2.523E−06	3.72E−07	9.352E−07	3.71E−07	8.943E−07	5.14E−07
11	429–595	1.891E−06	3.61E−07	3.029E−07	3.72E−07	5.755E−07	5.13E−07
12	595–766	1.067E−06	2.21E−07	2.712E−07	2.30E−07	1.775E−07	2.84E−07
13	766–1104	9.849E−07	1.69E−07	5.845E−07	1.71E−07	6.091E−07	2.27E−07
14	1104–1700	8.398E−07	1.16E−07	2.791E−07	1.20E−07	6.068E−07	1.66E−07

TABLE 3—*Continued*

		GRS 1009−45: Flux ± σ (photons cm^{-2} s^{-1} keV^{-1})					
Number	Energy (keV)	TJD: 8393–8800 Fig. 8, Panel (43-P1)	σ	TJD: 8800–9200 Fig. 8, Panel (43-P2)	σ	TJD: 9200–9628 Fig. 8, Panel (43-P3)	σ
1	35–40	4.005E−04	2.53E−05	5.905E−04	2.64E−05	6.937E−04	2.65E−05
2	40–45	2.937E−04	1.98E−05	4.016E−04	1.95E−05	5.004E−04	2.14E−05
3	45–55	1.661E−04	1.30E−05	2.773E−04	1.32E−05	3.303E−04	1.39E−05
4	55–73	8.759E−05	6.84E−06	1.504E−04	7.02E−06	1.738E−04	7.29E−06
5	73–98	3.699E−05	3.95E−06	7.401E−05	4.09E−06	9.331E−05	4.28E−06
6	98–123	2.028E−05	2.52E−06	4.034E−05	2.65E−06	5.205E−05	2.86E−06
7	123–162	1.180E−05	1.61E−06	2.228E−05	1.70E−06	3.077E−05	1.88E−06
8	162–230	7.861E−06	1.00E−06	1.114E−05	1.04E−06	1.353E−05	1.16E−06
9	230–313	3.078E−06	7.27E−07	4.383E−06	7.75E−07	6.899E−06	8.84E−07
10	313–429	1.637E−06	5.43E−07	2.516E−06	5.89E−07	3.264E−06	6.64E−07
11	429–595	1.741E−06	5.19E−07	2.049E−06	5.77E−07	8.227E−07	6.62E−07
12	595–766	9.954E−08	3.61E−07	2.832E−07	4.01E−07	−2.373E−08	4.29E−07
13	766–1104	1.551E−07	2.64E−07	4.663E−07	3.08E−07	1.923E−07	3.40E−07
14	1104–1700	−1.675E−07	1.76E−07	2.212E−07	2.16E−07	−7.291E−08	2.39E−07
		GRS 1915+105: Flux ± σ (photons cm^{-2} s^{-1} keV^{-1})					
Number	Energy (keV)	TJD: 8393–8800 Fig. 8, Panel (46-P1)	σ	TJD: 8800–9200 Fig. 8, Panel (46-P2)	σ	TJD: 9200–9628 Fig. 8, Panel (46-P3)	σ
1	35–40	2.612E−04	1.94E−05	1.423E−03	2.18E−05	5.987E−04	2.15E−05
2	40–45	2.154E−04	1.58E−05	1.015E−03	1.68E−05	4.592E−04	1.81E−05
3	45–55	1.585E−04	1.11E−05	7.307E−04	1.17E−05	3.037E−04	1.23E−05
4	55–73	9.745E−05	6.11E−06	3.913E−04	6.54E−06	1.534E−04	6.76E−06
5	73–98	5.156E−05	3.52E−06	1.830E−04	3.90E−06	7.268E−05	4.03E−06
6	98–123	2.832E−05	2.26E−06	8.787E−05	2.58E−06	3.573E−05	2.72E−06
7	123–162	1.583E−05	1.45E−06	4.113E−05	1.69E−06	1.884E−05	1.77E−06
8	162–230	9.096E−06	8.75E−07	1.697E−05	1.03E−06	9.474E−06	1.10E−06
9	230–313	4.270E−06	6.32E−07	7.215E−06	7.67E−07	4.488E−06	8.43E−07
10	313–429	2.660E−06	4.68E−07	4.614E−06	5.76E−07	2.104E−06	6.42E−07
11	429–595	2.450E−06	4.50E−07	3.938E−06	5.81E−07	1.849E−06	6.38E−07
12	595–766	9.736E−07	2.90E−07	2.024E−06	3.92E−07	1.042E−06	3.78E−07
13	766–1104	1.016E−06	2.19E−07	1.813E−06	3.24E−07	1.181E−06	3.10E−07
14	1104–1700	9.000E−07	1.50E−07	1.325E−06	2.31E−07	1.019E−06	2.21E−07
		GX 1+4: Flux ± σ (photons cm^{-2} s^{-1} keV^{-1})					
Number	Energy (keV)	TJD: 8393–8800 Fig. 8, Panel (47-P1)	σ	TJD: 8800–9200 Fig. 8, Panel (47-P2)	σ	TJD: 9200–9628 Fig. 8, Panel (47-P3)	σ
1	35–40	4.689E−04	2.47E−05	3.038E−04	2.50E−05	3.135E−04	2.65E−05
2	40–45	3.683E−04	1.92E−05	2.340E−04	1.85E−05	2.284E−04	2.11E−05
3	45–55	2.463E−04	1.25E−05	1.735E−04	1.26E−05	1.539E−04	1.39E−05
4	55–73	1.222E−04	6.62E−06	8.061E−05	6.76E−06	8.415E−05	7.40E−06
5	73–98	4.759E−05	3.85E−06	2.965E−05	3.93E−06	2.689E−05	4.32E−06
6	98–123	1.533E−05	2.49E−06	1.092E−05	2.56E−06	1.232E−05	2.87E−06
7	123–162	4.278E−06	1.59E−06	4.611E−06	1.64E−06	4.934E−06	1.87E−06
8	162–230	2.169E−06	9.87E−07	2.306E−06	1.00E−06	1.437E−06	1.16E−06
9	230–313	1.119E−06	7.32E−07	1.015E−06	7.40E−07	7.424E−07	8.72E−07
10	313–429	6.667E−07	5.49E−07	5.819E−07	5.63E−07	2.682E−08	6.41E−07
11	429–595	2.239E−07	5.34E−07	7.078E−07	5.45E−07	−6.054E−07	6.31E−07
12	595–766	−7.976E−07	3.80E−07	−9.352E−07	3.80E−07	−3.180E−07	4.01E−07
13	766–1104	−6.847E−07	2.80E−07	−4.325E−07	2.85E−07	−6.277E−07	3.11E−07
14	1104–1700	−5.703E−07	1.90E−07	−4.017E−07	1.90E−07	−1.671E−07	2.12E−07
		GX 1+4: Flux ± σ (photons cm^{-2} s^{-1} keV^{-1})					
Number	Energy (keV)	TJD: 8715–8720 Fig. 8, Panel (48)	σ	TJD: 8722–8727 Fig. 8, Panel (49)	σ	TJD: 8729–8734 Fig. 8, Panel (50)	σ
1	35–40	4.152E−04	2.03E−04	5.439E−04	2.20E−04	3.817E−04	2.05E−04
2	40–45	3.680E−04	1.67E−04	5.130E−04	1.84E−04	3.558E−04	1.61E−04
3	45–55	1.992E−04	8.50E−05	3.082E−04	1.00E−04	2.282E−04	1.14E−04
4	55–73	8.680E−05	4.12E−05	2.023E−04	4.27E−05	1.085E−04	5.29E−05
5	73–98	2.867E−05	2.73E−05	7.582E−05	2.59E−05	4.440E−05	3.02E−05
6	98–123	1.528E−05	1.74E−05	2.771E−05	1.45E−05	1.903E−05	2.08E−05

TABLE 3—*Continued*

		GX 1+4: Flux ± σ (photons cm^{-2} s^{-1} keV^{-1})					
Number	Energy (keV)	TJD: 8715–8720 Fig. 8, Panel (48)	σ	TJD: 8722–8727 Fig. 8, Panel (49)	σ	TJD: 8729–8734 Fig. 8, Panel (50)	σ
7	123–162	2.745E−06	1.03E−05	1.494E−05	1.05E−05	−4.166E−06	1.28E−05
8	162–230	−5.769E−06	7.55E−06	3.449E−06	7.14E−06	1.614E−05	9.20E−06
9	230–313	−3.703E−06	4.99E−06	5.988E−07	5.25E−06	−1.564E−06	7.39E−06
10	313–429	−1.563E−06	4.16E−06	1.621E−06	4.29E−06	5.913E−07	5.76E−06
11	429–595	−3.204E−06	3.93E−06	5.134E−06	4.32E−06	1.266E−08	6.11E−06
12	595–766	−3.424E−06	4.19E−06	2.924E−06	4.16E−06	1.330E−06	5.76E−06
13	766–1104	−4.825E−06	2.60E−06	1.692E−06	2.93E−06	3.265E−07	3.93E−06
14	1104–1700	−5.231E−06	2.29E−06	1.385E−06	1.68E−06	2.009E−06	2.78E−06
		GX 301−2: Flux ± σ (photons cm^{-2} s^{-1} keV^{-1})					
Number	Energy (keV)	TJD: 8393–8800 Fig. 8, Panel (51 & 52-P1)	σ	TJD: 8800–9200 Fig. 8, Panel (51-P2)	σ	TJD: 9200–9628 Fig. 8, Panel (51-P3)	σ
1	35–40	5.355E−04	1.89E−05	5.738E−04	2.04E−05	4.819E−04	2.13E−05
2	40–45	3.082E−04	1.48E−05	3.466E−04	1.56E−05	3.220E−04	1.73E−05
3	45–55	1.503E−04	9.89E−06	1.602E−04	1.01E−05	1.455E−04	1.15E−05
4	55–73	3.910E−05	5.37E−06	2.527E−05	5.38E−06	4.430E−05	5.99E−06
5	73–98	6.302E−06	3.13E−06	−7.988E−07	3.18E−06	1.200E−05	3.50E−06
6	98–123	1.517E−06	2.01E−06	−5.218E−06	2.08E−06	2.989E−06	2.34E−06
7	123–162	−1.416E−06	1.32E−06	−4.462E−06	1.36E−06	1.642E−06	1.54E−06
8	162–230	−4.895E−07	8.32E−07	−3.056E−06	8.59E−07	−6.773E−07	1.02E−06
9	230–313	−5.469E−07	6.10E−07	−2.067E−06	6.34E−07	−3.132E−07	7.80E−07
10	313–429	−1.603E−07	4.58E−07	−1.213E−06	4.71E−07	−2.082E−07	5.89E−07
11	429–595	−9.062E−08	4.68E−07	−2.791E−07	4.92E−07	5.456E−08	6.03E−07
12	595–766	1.059E−07	2.96E−07	−2.107E−08	3.16E−07	1.230E−07	3.53E−07
13	766–1104	1.145E−07	2.40E−07	3.695E−07	2.42E−07	2.790E−07	2.86E−07
14	1104–1700	2.222E−08	1.68E−07	1.176E−07	1.75E−07	1.729E−07	2.10E−07
		GX 312−1: Flux ± σ (photons cm^{-2} s^{-1} keV^{-1})					
Number	Energy (keV)	TJD: 8393–8800 Fig. 8, Panel (53-P1)	σ	TJD: 8800–9200 Fig. 8, Panel (53-P2)	σ	TJD: 9200–9628 Fig. 8, Panel (53-P3)	σ
1	35–40	1.379E−04	1.78E−05	1.299E−04	1.98E−05	2.075E−04	2.13E−05
2	40–45	9.475E−05	1.40E−05	1.070E−04	1.54E−05	1.801E−04	1.76E−05
3	45–55	7.880E−05	9.29E−06	8.547E−05	9.98E−06	1.250E−04	1.16E−05
4	55–73	4.885E−05	5.17E−06	5.014E−05	5.42E−06	6.941E−05	6.06E−06
5	73–98	2.450E−05	2.98E−06	2.177E−05	3.17E−06	2.760E−05	3.55E−06
6	98–123	1.235E−05	1.89E−06	1.167E−05	2.04E−06	1.346E−05	2.36E−06
7	123–162	7.654E−06	1.24E−06	5.388E−06	1.33E−06	6.607E−06	1.54E−06
8	162–230	3.732E−06	7.59E−07	2.259E−06	8.25E−07	2.935E−06	1.00E−06
9	230–313	2.949E−06	5.43E−07	5.928E−07	5.94E−07	2.551E−06	7.63E−07
10	313–429	1.245E−06	3.97E−07	2.735E−07	4.32E−07	1.595E−06	5.61E−07
11	429–595	1.405E−06	3.87E−07	4.600E−07	4.30E−07	1.717E−06	5.58E−07
12	595–766	8.453E−07	2.33E−07	4.900E−07	2.60E−07	9.942E−07	3.13E−07
13	766–1104	7.469E−07	1.79E−07	3.176E−07	1.95E−07	4.056E−07	2.49E−07
14	1104–1700	4.249E−07	1.25E−07	−1.350E−07	1.40E−07	5.675E−07	1.83E−07
		GX 339−4 (Low State): Flux ± σ (photons cm^{-2} s^{-1} keV^{-1})					
Number	Energy (keV)	TJD: 8550–8800 Fig. 8, Panel (54-P1)	σ	TJD: 9000–9200 Fig. 8, Panel (54-P2)	σ	TJD: 9200–9300 Fig. 8, Panel (54-P3)	σ
1	35–40	1.373E−04	2.73E−05	2.065E−04	3.20E−05	7.329E−05	3.94E−05
2	40–45	1.059E−04	2.14E−05	1.519E−04	2.34E−05	4.859E−05	3.09E−05
3	45–55	9.229E−05	1.39E−05	1.118E−04	1.59E−05	3.947E−05	2.06E−05
4	55–73	6.160E−05	7.28E−06	5.525E−05	8.79E−06	3.095E−05	1.05E−05
5	73–98	3.468E−05	4.18E−06	2.419E−05	5.09E−06	2.340E−05	6.15E−06
6	98–123	1.855E−05	2.72E−06	1.268E−05	3.33E−06	1.069E−05	4.07E−06
7	123–162	1.491E−05	1.68E−06	5.835E−06	2.12E−06	1.136E−05	2.67E−06
8	162–230	9.597E−06	1.04E−06	3.023E−06	1.29E−06	6.685E−06	1.61E−06
9	230–313	6.980E−06	7.49E−07	2.994E−06	9.93E−07	3.872E−06	1.23E−06
10	313–429	5.335E−06	5.58E−07	2.897E−06	7.19E−07	2.339E−06	8.82E−07
11	429–595	4.869E−06	5.33E−07	2.016E−06	6.95E−07	1.754E−06	7.65E−07
12	595–766	2.662E−06	3.47E−07	1.676E−06	4.25E−07	1.592E−06	5.14E−07

TABLE 3—*Continued*

		GX 339−4 (Low State): Flux ± σ (photons cm^{-2} s^{-1} keV^{-1})					
Number	Energy (keV)	TJD: 8550–8800 Fig. 8, Panel (54-P1)	σ	TJD: 9000–9200 Fig. 8, Panel (54-P2)	σ	TJD: 9200–9300 Fig. 8, Panel (54-P3)	σ
13	766–1104	2.248E−06	2.59E−07	1.144E−06	3.45E−07	4.073E−07	3.57E−07
14	1104–1700	1.713E−06	1.73E−07	9.247E−07	2.37E−07	2.519E−07	2.47E−07
		GX 339−4 (High State): Flux ± σ (photons cm^{-2} s^{-1} keV^{-1})					
Number	Energy (keV)	TJD: 8460–8515 Fig. 8, Panel (55 & 56-P1)	σ	TJD: 8880–8980 Fig. 8, Panel (55-P2)	σ	TJD: 9360–9418 Fig. 8, Panel (55-P3)	σ
1	35–40	1.762E−03	6.27E−05	1.252E−03	5.05E−05	1.799E−03	6.97E−05
2	40–45	1.424E−03	4.84E−05	1.106E−03	3.98E−05	1.431E−03	4.97E−05
3	45–55	1.023E−03	3.05E−05	7.632E−04	2.38E−05	1.110E−03	3.37E−05
4	55–73	6.462E−04	1.62E−05	4.855E−04	1.20E−05	7.007E−04	1.91E−05
5	73–98	3.482E−04	9.74E−06	2.708E−04	7.05E−06	3.814E−04	1.04E−05
6	98–123	1.781E−04	6.20E−06	1.505E−04	4.41E−06	2.025E−04	7.02E−06
7	123–162	8.816E−05	4.23E−06	7.888E−05	2.94E−06	9.731E−05	4.45E−06
8	162–230	3.260E−05	2.64E−06	3.504E−05	1.89E−06	4.491E−05	3.29E−06
9	230–313	1.307E−05	1.92E−06	1.497E−05	1.43E−06	2.273E−05	2.71E−06
10	313–429	8.533E−06	1.41E−06	7.880E−06	1.05E−06	1.345E−05	2.06E−06
11	429–595	6.498E−06	1.42E−06	6.843E−06	1.04E−06	1.268E−05	2.18E−06
12	595–766	3.118E−06	1.01E−06	3.126E−06	7.44E−07	5.042E−06	9.90E−07
13	766–1104	2.924E−06	7.74E−07	2.931E−06	5.17E−07	4.218E−06	8.71E−07
14	1104–1700	1.711E−06	5.40E−07	1.588E−06	3.77E−07	3.218E−06	7.46E−07
		GX 339−4: Flux ± σ (photons cm^{-2} s^{-1} keV^{-1})					
Number	Energy (keV)	TJD: 8505–8510 Fig. 8, Panel (57)	σ				
1	35–40	1.772E−03	1.59E−04				
2	40–45	1.606E−03	1.22E−04				
3	45–55	1.075E−03	7.11E−05				
4	55–73	7.179E−04	3.58E−05				
5	73–98	3.590E−04	2.26E−05				
6	98–123	1.800E−04	1.40E−05				
7	123–162	7.536E−05	1.03E−05				
8	162–230	2.420E−05	6.42E−06				
9	230–313	1.438E−05	4.43E−06				
10	313–429	7.515E−06	2.90E−06				
11	429–595	5.376E−06	2.49E−06				
12	595–766	4.588E−06	2.05E−06				
13	766–1104	4.315E−06	1.38E−06				
14	1104–1700	2.528E−06	9.20E−07				
		GX 354+0: Flux ± σ (photons cm^{-2} s^{-1} keV^{-1})					
Number	Energy (keV)	TJD: 8393–8800 Fig. 8, Panel (58-P1)	σ	TJD: 8800–9200 Fig. 8, Panel (58-P2)	σ	TJD: 9200–9628 Fig. 8, Panel (58-P3)	σ
1	35–40	3.369E−04	2.39E−05	3.794E−04	2.50E−05	2.766E−04	2.50E−05
2	40–45	2.565E−04	1.90E−05	2.756E−04	1.87E−05	2.189E−04	2.03E−05
3	45–55	1.784E−04	1.23E−05	1.998E−04	1.26E−05	1.392E−04	1.33E−05
4	55–73	1.030E−04	6.57E−06	1.013E−04	6.72E−06	7.328E−05	6.99E−06
5	73–98	5.320E−05	3.80E−06	3.907E−05	3.90E−06	4.206E−05	4.09E−06
6	98–123	2.699E−05	2.42E−06	1.900E−05	2.51E−06	2.054E−05	2.74E−06
7	123–162	1.609E−05	1.54E−06	8.171E−06	1.59E−06	1.183E−05	1.78E−06
8	162–230	9.155E−06	9.57E−07	2.572E−06	9.74E−07	7.155E−06	1.11E−06
9	230–313	6.589E−06	7.02E−07	1.765E−06	7.22E−07	5.956E−06	8.49E−07
10	313–429	5.243E−06	5.23E−07	1.636E−06	5.42E−07	4.944E−06	6.31E−07
11	429–595	5.276E−06	4.99E−07	1.196E−06	5.22E−07	4.920E−06	6.20E−07
12	595–766	2.524E−06	3.32E−07	1.415E−07	3.60E−07	2.726E−06	3.77E−07
13	766–1104	2.323E−06	2.51E−07	3.089E−07	2.64E−07	2.711E−06	3.01E−07
14	1104–1700	1.907E−06	1.68E−07	2.356E−07	1.81E−07	1.595E−06	2.09E−07

TABLE 3—*Continued*

		Her X-1: Flux ± σ (photons cm^{-2} s^{-1} keV^{-1})					
Number	Energy (keV)	TJD: 8394–8798 Fig. 8, Panel (59 & 60-P1)	σ	TJD: 8800–9200 Fig. 8, Panel (59-P2)	σ	TJD: 9200–9628 Fig. 8, Panel (59-P3)	σ
1	35–40	1.678E−04	1.62E−05	2.187E−04	1.53E−05	2.123E−04	1.80E−05
2	40–45	1.381E−04	1.32E−05	1.542E−04	1.24E−05	1.644E−04	1.47E−05
3	45–55	9.070E−05	9.25E−06	9.225E−05	8.63E−06	9.674E−05	1.01E−05
4	55–73	5.279E−05	5.24E−06	4.735E−05	5.06E−06	4.945E−05	5.65E−06
5	73–98	2.366E−05	3.08E−06	2.054E−05	3.00E−06	2.267E−05	3.36E−06
6	98–123	1.483E−05	1.97E−06	1.370E−05	1.95E−06	1.488E−05	2.23E−06
7	123–162	1.017E−05	1.26E−06	6.736E−06	1.28E−06	8.972E−06	1.45E−06
8	162–230	4.747E−06	7.30E−07	3.556E−06	7.63E−07	4.581E−06	9.04E−07
9	230–313	3.039E−06	5.08E−07	2.943E−06	5.36E−07	3.969E−06	6.54E−07
10	313–429	2.337E−06	3.57E−07	1.781E−06	3.81E−07	2.610E−06	4.57E−07
11	429–595	1.877E−06	3.50E−07	1.841E−06	3.76E−07	2.533E−06	4.49E−07
12	595–766	1.214E−06	2.11E−07	8.483E−07	2.30E−07	1.850E−06	2.64E−07
13	766–1104	1.123E−06	1.65E−07	1.245E−06	1.82E−07	1.652E−06	2.01E−07
14	1104–1700	8.014E−07	1.13E−07	8.428E−07	1.25E−07	1.182E−06	1.40E−07
		HR 1099: Flux ± σ (photons cm^{-2} s^{-1} keV^{-1})					
Number	Energy (keV)	TJD: 8393–8798 Fig. 8, Panel (61-P1)	σ	TJD: 8806–9198 Fig. 8, Panel (61-P2)	σ	TJD: 9203–9628 Fig. 8, Panel (61-P3)	σ
1	35–40	9.374E−05	1.31E−05	1.048E−04	1.26E−05	1.065E−04	1.29E−05
2	40–45	8.980E−05	1.09E−05	9.840E−05	1.11E−05	9.346E−05	1.15E−05
3	45–55	7.891E−05	8.26E−06	8.587E−05	8.08E−06	8.469E−05	8.57E−06
4	55–73	4.816E−05	4.94E−06	5.368E−05	4.84E−06	5.179E−05	5.36E−06
5	73–98	2.661E−05	2.88E−06	3.016E−05	2.85E−06	3.389E−05	3.15E−06
6	98–123	1.534E−05	1.87E−06	1.767E−05	1.89E−06	2.003E−05	2.09E−06
7	123–162	8.961E−06	1.18E−06	9.192E−06	1.21E−06	1.102E−05	1.34E−06
8	162–230	2.392E−06	6.86E−07	3.831E−06	7.03E−07	4.796E−06	8.03E−07
9	230–313	8.037E−07	4.93E−07	1.213E−06	5.07E−07	2.608E−06	5.99E−07
10	313–429	2.424E−07	3.62E−07	1.954E−07	3.57E−07	1.551E−06	4.22E−07
11	429–595	2.899E−07	3.60E−07	1.057E−07	3.58E−07	1.713E−06	4.29E−07
12	595–766	2.489E−07	2.25E−07	−2.551E−07	2.22E−07	7.075E−07	2.52E−07
13	766–1104	3.650E−07	1.75E−07	−3.203E−08	1.74E−07	5.817E−07	2.01E−07
14	1104–1700	5.237E−07	1.22E−07	2.755E−07	1.22E−07	5.596E−07	1.40E−07
		NGC 1275: Flux ± σ (photons cm^{-2} s^{-1} keV^{-1})					
Number	Energy (keV)	TJD: 8393–8800 Fig. 8, Panel (62 & 63-P1)	σ	TJD: 8800–9198 Fig. 8, Panel (62-P2)	σ	TJD: 9200–9628 Fig. 8, Panel (62-P3)	σ
1	35–40	5.966E−05	1.21E−05	8.040E−05	1.24E−05	6.924E−05	1.35E−05
2	40–45	5.096E−05	9.96E−06	7.303E−05	1.02E−05	6.639E−05	1.13E−05
3	45–55	4.594E−05	7.48E−06	5.806E−05	7.53E−06	5.824E−05	8.56E−06
4	55–73	2.891E−05	4.55E−06	3.963E−05	4.58E−06	4.156E−05	5.19E−06
5	73–98	1.976E−05	2.70E−06	2.486E−05	2.73E−06	2.640E−05	3.06E−06
6	98–123	1.258E−05	1.72E−06	1.455E−05	1.84E−06	1.696E−05	2.02E−06
7	123–162	8.334E−06	1.07E−06	8.999E−06	1.16E−06	1.054E−05	1.31E−06
8	162–230	4.759E−06	6.13E−07	5.296E−06	6.57E−07	5.570E−06	7.93E−07
9	230–313	4.196E−06	4.31E−07	3.743E−06	4.59E−07	3.599E−06	5.73E−07
10	313–429	2.721E−06	3.03E−07	2.386E−06	3.17E−07	2.964E−06	4.03E−07
11	429–595	2.651E−06	2.93E−07	2.250E−06	3.13E−07	2.657E−06	4.02E−07
12	595–766	1.627E−06	1.76E−07	1.383E−06	1.89E−07	1.989E−06	2.36E−07
13	766–1104	1.384E−06	1.34E−07	1.076E−06	1.49E−07	1.380E−06	1.83E−07
14	1104–1700	1.230E−06	9.48E−08	1.007E−06	1.01E−07	1.169E−06	1.33E−07
		NGC 4151: Flux ± σ (photons cm^{-2} s^{-1} keV^{-1})					
Number	Energy (keV)	TJD: 8393–8800 Fig. 8, Panel (64 & 65-P1)	σ	TJD: 8800–9200 Fig. 8, Panel (64-P2)	σ	TJD: 9200–9628 Fig. 8, Panel (64-P3)	σ
1	35–40	1.730E−04	1.36E−05	1.857E−04	1.33E−05	2.743E−04	1.55E−05
2	40–45	1.236E−04	1.07E−05	1.660E−04	1.07E−05	2.043E−04	1.26E−05
3	45–55	9.929E−05	7.79E−06	1.213E−04	7.73E−06	1.611E−04	9.08E−06
4	55–73	6.673E−05	4.62E−06	7.318E−05	4.49E−06	9.419E−05	5.44E−06
5	73–98	3.853E−05	2.76E−06	4.002E−05	2.70E−06	5.209E−05	3.28E−06
6	98–123	2.309E−05	1.77E−06	2.176E−05	1.75E−06	2.876E−05	2.15E−06
7	123–162	1.357E−05	1.11E−06	1.145E−05	1.13E−06	1.692E−05	1.40E−06

TABLE 3—*Continued*

		NGC 4151: Flux ± σ (photons cm^{-2} s^{-1} keV^{-1})					
Number	Energy (keV)	TJD: 8393–8800 Fig. 8, Panel (64 & 65-P1)	σ	TJD: 8800–9200 Fig. 8, Panel (64-P2)	σ	TJD: 9200–9628 Fig. 8, Panel (64-P3)	σ
8	162–230	6.117E−06	6.39E−07	5.192E−06	6.64E−07	7.647E−06	8.54E−07
9	230–313	3.504E−06	4.45E−07	2.694E−06	4.61E−07	4.082E−06	6.17E−07
10	313–429	2.003E−06	3.14E−07	1.776E−06	3.22E−07	1.909E−06	4.45E−07
11	429–595	1.411E−06	3.14E−07	1.481E−06	3.13E−07	2.039E−06	4.50E−07
12	595–766	8.008E−07	1.88E−07	9.617E−07	1.94E−07	1.536E−06	2.64E−07
13	766–1104	6.366E−07	1.46E−07	9.649E−07	1.54E−07	1.01E−06	2.06E−07
14	1104–1700	5.249E−07	1.05E−07	7.978E−07	1.04E−07	7.439E−07	1.44E−07

		NGC 4151: Flux ± σ (photons cm^{-2} s^{-1} keV^{-1})	
Number	Energy (keV)	TJD: 8722–8727 Fig. 8, Panel (66)	σ
1	35–40	1.561E−04	9.11E−05
2	40–45	1.307E−04	8.48E−05
3	45–55	1.047E−04	6.26E−05
4	55–73	8.069E−05	3.21E−05
5	73–98	5.995E−05	1.85E−05
6	98–123	3.892E−05	1.33E−05
7	123–162	2.493E−05	7.79E−06
8	162–230	1.106E−05	4.50E−06
9	230–313	8.436E−06	3.99E−06
10	313–429	3.537E−06	2.92E−06
11	429–595	−5.922E−07	3.45E−06
12	595–766	−1.020E−06	1.60E−06
13	766–1104	−1.673E−07	1.62E−06
14	1104–1700	−9.249E−07	1.28E−06

		Nova Sag: Flux ± σ (photons cm^{-2} s^{-1} keV^{-1})					
Number	Energy (keV)	TJD: 8395–8800 Fig. 8, Panel (67-P1)	σ	TJD: 8800–9200 Fig. 8, Panel (67-P2)	σ	TJD: 9204–9628 Fig. 8, Panel (67-P3)	σ
1	35–40	3.022E−04	2.23E−05	3.074E−04	2.25E−05	2.438E−04	2.40E−05
2	40–45	2.132E−04	1.76E−05	2.109E−04	1.71E−05	1.830E−04	1.98E−05
3	45–55	1.213E−04	1.16E−05	1.387E−04	1.16E−05	1.108E−04	1.30E−05
4	55–73	6.282E−05	6.16E−06	7.035E−05	6.28E−06	5.872E−05	6.81E−06
5	73–98	3.600E−05	3.56E−06	3.686E−05	3.65E−06	3.267E−05	4.02E−06
6	98–123	1.812E−05	2.29E−06	2.138E−05	2.34E−06	1.946E−05	2.67E−06
7	123–162	1.143E−05	1.46E−06	1.215E−05	1.49E−06	1.200E−05	1.73E−06
8	162–230	6.935E−06	8.96E−07	6.754E−06	9.02E−07	8.103E−06	1.06E−06
9	230–313	5.343E−06	6.53E−07	3.959E−06	6.51E−07	5.077E−06	8.00E−07
10	313–429	4.218E−06	4.81E−07	2.345E−06	4.85E−07	3.892E−06	5.89E−07
11	429–595	3.261E−06	4.68E−07	1.234E−06	4.59E−07	3.450E−06	5.81E−07
12	595–766	1.356E−06	3.16E−07	3.912E−07	3.05E−07	1.663E−06	3.55E−07
13	766–1104	8.471E−07	2.31E−07	1.971E−07	2.20E−07	1.082E−06	2.76E−07
14	1104–1700	7.877E−07	1.56E−07	8.869E−08	1.53E−07	1.112E−06	1.91E−07

		OAO 1657−415: Flux ± σ (photons cm^{-2} s^{-1} keV^{-1})					
Number	Energy (keV)	TJD: 8393–8795 Fig. 8, Panel (68-P1)	σ	TJD: 8800–9200 Fig. 8, Panel (68-P2)	σ	TJD: 9200–9628 Fig. 8, Panel (68-P3)	σ
1	35–40	4.335E−04	2.66E−05	3.693E−04	2.57E−05	4.363E−04	2.88E−05
2	40–45	3.195E−04	2.07E−05	2.534E−04	1.91E−05	3.344E−04	2.33E−05
3	45–55	1.974E−04	1.35E−05	1.589E−04	1.31E−05	2.214E−04	1.52E−05
4	55–73	9.979E−05	7.11E−06	6.611E−05	7.13E−06	9.852E−05	8.05E−06
5	73–98	3.334E−05	4.14E−06	3.072E−05	4.13E−06	3.653E−05	4.78E−06
6	98–123	7.127E−06	2.68E−06	1.054E−05	2.69E−06	1.249E−05	3.20E−06
7	123–162	4.357E−06	1.70E−06	4.766E−06	1.71E−06	4.561E−06	2.09E−06
8	162–230	1.940E−06	1.06E−06	1.389E−06	1.04E−06	2.307E−06	1.32E−06
9	230–313	1.288E−06	7.91E−07	1.370E−06	7.81E−07	1.317E−06	1.02E−06
10	313–429	1.297E−06	5.93E−07	1.448E−06	5.89E−07	−1.620E−07	7.55E−07
11	429–595	1.402E−06	5.76E−07	9.780E−07	5.62E−07	1.310E−07	7.53E−07
12	595–766	7.885E−07	4.06E−07	7.487E−07	3.98E−07	2.673E−07	4.81E−07
13	766–1104	1.066E−06	2.93E−07	4.211E−07	2.78E−07	−2.779E−07	3.76E−07
14	1104–1700	8.878E−07	1.93E−07	5.047E−07	1.89E−07	1.195E−07	2.59E−07

TABLE 3—*Continued*

		PSR 1259−63: Flux ± σ (photons cm^{-2} s^{-1} keV^{-1})					
Number	Energy (keV)	TJD: 8393–8800 Fig. 8, Panel (69-P1)	σ	TJD: 8800–9200 Fig. 8, Panel (69-P2)	σ	TJD: 9200–9628 Fig. 8, Panel (69-P3)	σ
1	35–40	1.263E−04	1.78E−05	1.067E−04	1.92E−05	1.149E−04	2.03E−05
2	40–45	8.776E−05	1.41E−05	8.337E−05	1.49E−05	7.926E−05	1.66E−05
3	45–55	6.932E−05	9.44E−06	5.947E−05	9.73E−06	6.773E−05	1.11E−05
4	55–73	4.511E−05	5.23E−06	4.095E−05	5.26E−06	4.104E−05	5.86E−06
5	73–98	2.325E−05	3.04E−06	2.037E−05	3.12E−06	1.967E−05	3.43E−06
6	98–123	1.226E−05	1.94E−06	1.163E−05	2.02E−06	1.123E−05	2.28E−06
7	123–162	7.237E−06	1.27E−06	4.440E−06	1.31E−06	3.357E−06	1.48E−06
8	162–230	3.445E−06	7.84E−07	1.382E−06	8.12E−07	1.382E−06	9.76E−07
9	230–313	2.015E−06	5.66E−07	3.808E−08	5.88E−07	2.067E−06	7.37E−07
10	313–429	1.492E−06	4.17E−07	5.780E−07	4.26E−07	1.676E−06	5.48E−07
11	429–595	1.301E−06	4.14E−07	1.115E−07	4.28E−07	1.445E−06	5.42E−07
12	595–766	1.260E−06	2.49E−07	−8.597E−09	2.63E−07	7.248E−07	3.06E−07
13	766–1104	9.882E−07	1.94E−07	8.001E−09	1.97E−07	4.358E−07	2.39E−07
14	1104–1700	7.382E−07	1.35E−07	−1.090E−07	1.41E−07	6.544E−07	1.72E−07
		PSR 1509−58: Flux ± σ (photons cm^{-2} s^{-1} keV^{-1})					
Number	Energy (keV)	TJD: 8393–8789 Fig. 8, Panel (70 & 71-P1)	σ	TJD: 8800–9200 Fig. 8, Panel (70-P2)	σ	TJD: 9200–9628 Fig. 8, Panel (70-P3)	σ
1	35–40	8.136E−05	2.27E−05	1.571E−04	2.47E−05	7.117E−05	2.47E−05
2	40–45	5.338E−05	1.73E−05	1.269E−04	1.89E−05	6.972E−05	2.03E−05
3	45–55	5.232E−05	1.14E−05	8.770E−05	1.26E−05	7.323E−05	1.34E−05
4	55–73	4.205E−05	6.30E−06	6.475E−05	6.78E−06	5.408E−05	6.91E−06
5	73–98	2.465E−05	3.60E−06	3.976E−05	3.99E−06	3.028E−05	4.05E−06
6	98–123	1.475E−05	2.27E−06	2.608E−05	2.54E−06	2.038E−05	2.70E−06
7	123–162	9.750E−06	1.45E−06	1.656E−05	1.65E−06	1.295E−05	1.78E−06
8	162–230	6.411E−06	9.01E−07	9.193E−06	1.03E−06	6.555E−06	1.15E−06
9	230–313	4.479E−06	6.59E−07	5.966E−06	7.70E−07	5.057E−06	8.85E−07
10	313–429	2.773E−06	4.89E−07	3.449E−06	5.78E−07	3.640E−06	6.51E−07
11	429–595	2.400E−06	4.69E−07	3.450E−06	5.79E−07	3.320E−06	6.47E−07
12	595–766	1.542E−06	2.95E−07	2.005E−06	3.74E−07	1.395E−06	3.60E−07
13	766–1104	9.856E−07	2.26E−07	1.386E−06	2.85E−07	1.283E−06	2.92E−07
14	1104–1700	8.929E−07	1.55E−07	7.926E−07	1.98E−07	9.376E−07	2.06E−07
		Sco X-1: Flux ± σ (photons cm^{-2} s^{-1} keV^{-1})					
Number	Energy (keV)	TJD: 8393–8800 Fig. 8, Panel (72 & 73-P1)	σ	TJD: 8800–9200 Fig. 8, Panel (72-P2)	σ	TJD: 9200–9628 Fig. 8, Panel (72-P3)	σ
1	35–40	9.708E−04	2.15E−05	1.064E−03	2.25E−05	1.077E−03	2.39E−05
2	40–45	5.389E−04	1.63E−05	4.873E−04	1.63E−05	5.658E−04	1.77E−05
3	45–55	1.775E−04	1.04E−05	2.035E−04	1.09E−05	1.926E−04	1.16E−05
4	55–73	4.934E−05	5.53E−06	5.804E−05	5.71E−06	5.160E−05	6.03E−06
5	73–98	1.457E−05	3.19E−06	1.804E−05	3.30E−06	1.540E−05	3.52E−06
6	98–123	5.388E−06	2.05E−06	7.108E−06	2.15E−06	6.967E−06	2.32E−06
7	123–162	1.813E−07	1.33E−06	4.771E−06	1.40E−06	1.908E−06	1.55E−06
8	162–230	−5.509E−07	8.31E−07	2.174E−06	8.71E−07	−6.575E−07	9.93E−07
9	230–313	−9.148E−07	6.05E−07	5.719E−07	6.46E−07	−3.397E−07	7.38E−07
10	313–429	−6.190E−07	4.47E−07	2.152E−07	4.70E−07	−1.149E−06	5.40E−07
11	429–595	−1.496E−06	4.44E−07	−1.491E−08	4.85E−07	−8.100E−07	5.45E−07
12	595–766	−1.107E−06	2.94E−07	2.252E−07	3.33E−07	−5.557E−07	3.35E−07
13	766–1104	−8.507E−07	2.28E−07	3.488E−07	2.56E−07	−6.551E−07	2.73E−07
14	1104–1700	−5.269E−07	1.55E−07	2.098E−07	1.86E−07	−3.718E−07	1.89E−07
		Sct X-1: Flux ± σ (photons cm^{-2} s^{-1} keV^{-1})					
Number	Energy (keV)	TJD: 8393–8800 Fig. 8, Panel (74 & 75-P1)	σ	TJD: 8800–9200 Fig. 8, Panel (74-P2)	σ	TJD: 9200–9628 Fig. 8, Panel (74-P3)	σ
1	35–40	3.404E−04	2.06E−05	3.035E−04	2.17E−05	3.165E−04	2.16E−05
2	40–45	2.549E−04	1.65E−05	2.392E−04	1.66E−05	2.191E−04	1.79E−05
3	45–55	1.657E−04	1.13E−05	1.668E−04	1.14E−05	1.532E−04	1.20E−05
4	55–73	9.378E−05	6.13E−06	8.461E−05	6.20E−06	7.774E−05	6.59E−06
5	73–98	4.958E−05	3.52E−06	4.788E−05	3.63E−06	4.043E−05	3.84E−06

TABLE 3—*Continued*

		Sct X-1: Flux ± σ (photons cm^{-2} s^{-1} keV^{-1})					
Number	Energy (keV)	TJD: 8393–8800 Fig. 8, Panel (74 & 75-P1)	σ	TJD: 8800–9200 Fig. 8, Panel (74-P2)	σ	TJD: 9200–9628 Fig. 8, Panel (74-P3)	σ
6	98–123	2.909E−05	2.23E−06	2.625E−05	2.34E−06	2.309E−05	2.56E−06
7	123–162	1.643E−05	1.43E−06	1.537E−05	1.51E−06	1.425E−05	1.65E−06
8	162–230	8.672E−06	8.73E−07	7.188E−06	9.08E−07	6.969E−06	1.00E−06
9	230–313	5.499E−06	6.34E−07	4.544E−06	6.59E−07	4.262E−06	7.43E−07
10	313–429	3.536E−06	4.69E−07	3.246E−06	4.86E−07	2.603E−06	5.48E−07
11	429–595	3.186E−06	4.50E−07	2.586E−06	4.66E−07	2.413E−06	5.31E−07
12	595–766	1.877E−06	2.88E−07	1.293E−06	2.98E−07	1.208E−06	3.12E−07
13	766–1104	1.282E−06	2.24E−07	1.026E−06	2.33E−07	1.039E−06	2.49E−07
14	1104–1700	7.415E−07	1.49E−07	7.276E−07	1.58E−07	9.543E−07	1.72E−07
		Vela X-1: Flux ± σ (photons cm^{-2} s^{-1} keV^{-1})					
Number	Energy (keV)	TJD: 8393–8800 Fig. 8, Panel (76-P1)	σ	TJD: 8800–9200 Fig. 8, Panel (76 & 77-P2)	σ	TJD: 9200–9628 Fig. 8, Panel (76-P3)	σ
1	35–40	1.033E−03	1.57E−05	9.926E−04	1.66E−05	8.587E−04	1.67E−05
2	40–45	6.105E−04	1.21E−05	6.305E−04	1.29E−05	5.903E−04	1.42E−05
3	45–55	3.392E−04	8.57E−06	3.262E−04	8.29E−06	2.915E−04	9.63E−06
4	55–73	8.424E−05	4.61E−06	8.628E−05	4.44E−06	6.930E−05	5.24E−06
5	73–98	1.423E−05	2.74E−06	1.505E−05	2.63E−06	1.029E−05	3.12E−06
6	98–123	2.251E−06	1.82E−06	5.065E−07	1.73E−06	−2.492E−07	2.08E−06
7	123–162	6.872E−07	1.18E−06	−7.693E−07	1.15E−06	−1.031E−06	1.38E−06
8	162–230	1.623E−06	7.35E−07	−4.956E−07	7.22E−07	2.522E−08	9.11E−07
9	230–313	1.564E−06	5.39E−07	1.801E−07	5.38E−07	3.611E−08	6.89E−07
10	313–429	9.611E−07	3.97E−07	−1.139E−07	4.01E−07	−6.913E−07	5.23E−07
11	429–595	1.411E−06	3.99E−07	−4.593E−07	4.19E−07	−7.035E−07	5.46E−07
12	595–766	5.402E−07	2.60E−07	−5.455E−07	2.84E−07	−8.280E−07	3.17E−07
13	766–1104	6.636E−07	2.05E−07	−3.112E−07	2.22E−07	−5.533E−07	2.73E−07
14	1104–1700	2.279E−07	1.47E−07	−2.735E−07	1.64E−07	−3.312E−07	2.03E−07

Note.—See § 2.4.4. for a discussion of the errors included.

∼18% in the 123–164 keV range. Similar differences between BATSE and OSSE have been detected in other source spectra as well as those shown in other panels of Figure 8. The causes may be due to systematic effects associated with the calibration of the two instruments. Above 150 keV, the BATSE/EBOP Crab fluxes are consistent with those of OSSE and COMPTEL to within the 2 σ level. Figure 8 panel 11 shows direct comparison of three consecutive 400 day averaged spectra derived by EBOP. The three spectra are nearly indistinguishable. The reasonably good agreement of the Crab spectra with those measured by others, and the consistency and repeatability of the long-term Crab spectra over 3 years provide us the confidence in the EBOP methodology in producing reliable and stable results over time.

In addition to the Crab's comparison, Figure 8 contains comparison of 39 other BATSE spectra with corresponding source spectra measured by OSSE, COMPTEL, SIGMA, and *HEAO 1* A-4 that we have collected to date. These are shown for 3C 273 (panel 3), 4U 1543−45 (panel 5), Crab (panels 12 & 13), Cygnus X-1 (panels 15–31), Cygnus X-3 (panel 33), GRO J0422+32 (panels 36–39), GRS 1758−258 (panel 45), GX 1+4 (panels 48–50), GX 301−2 (panel 52), GX 339−4 (panels 56–57), Her X-1 (panel 60), NGC 1275 (panel 63), NGC 4151 (panels 65–66), PSR 1509−58 (panel 71), SCO X-1 (panel 73), SCTX-1 (panel 75), and Vela X-1 (panel 77), respectively. Of the 39 panels, 24 panels [Cygnus X-1 (panels 15–31; Ling et al. 1997; Philips et al. 1996; McConnell et al. 1997, 1999), GRO J0422+32 (panels 36–39; Roques et al. 1994; Van Dijk et al. 1995), GX 1+4 (panels 49–50), and GX 339−4 (panel 57)] show direct comparison of spectra measured simultaneously by BATSE and others. OSSE's spectra and associated Poisson errors were taken primarily from the OSSE public archive in 1996–1997. Fluxes measured by *HEAO 1* A-4 were published in the *HEAO 1* A-4 catalog (Levine et al. 1984). Spectra measured by COMPTEL (Cygnus X-1 spectrum, panel 15, McConnell et al. 1997; GRO J0422+32, panel 36, Van Dijk et al. 1995), and by SIGMA (GRO J0422+32, panel 39, Roques et al. 1994), were from figures shown in their published papers. For weak sources such as 3C 273 or Cygnus X-3, which were only marginally detected by BATSE over a single viewing period, a 400 day average spectrum for these sources is also included for comparison. These appear in the remaining 15 of the 39 panels shown in Figure 8. Of the 24 direct comparisons, 17 sets are on Cygnus X-1, which include one with COMPTEL and 16 with OSSE. For the former (see panel 15), BATSE fluxes in the 0.6–2 MeV region integrated over the same 17 observational periods of Cygnus X-1 by COMPTEL for a total of ∼125 days agree very well with the corresponding fluxes measured by COMPTEL. For the latter (see panels 16–31), BATSE's fluxes are generally consistent with OSSE's to within the 2 σ level above 600 keV. Below 600 keV, the BATSE's fluxes are mostly higher by ∼5%–30% in different spectral regions and from spectrum to spectrum. Of the

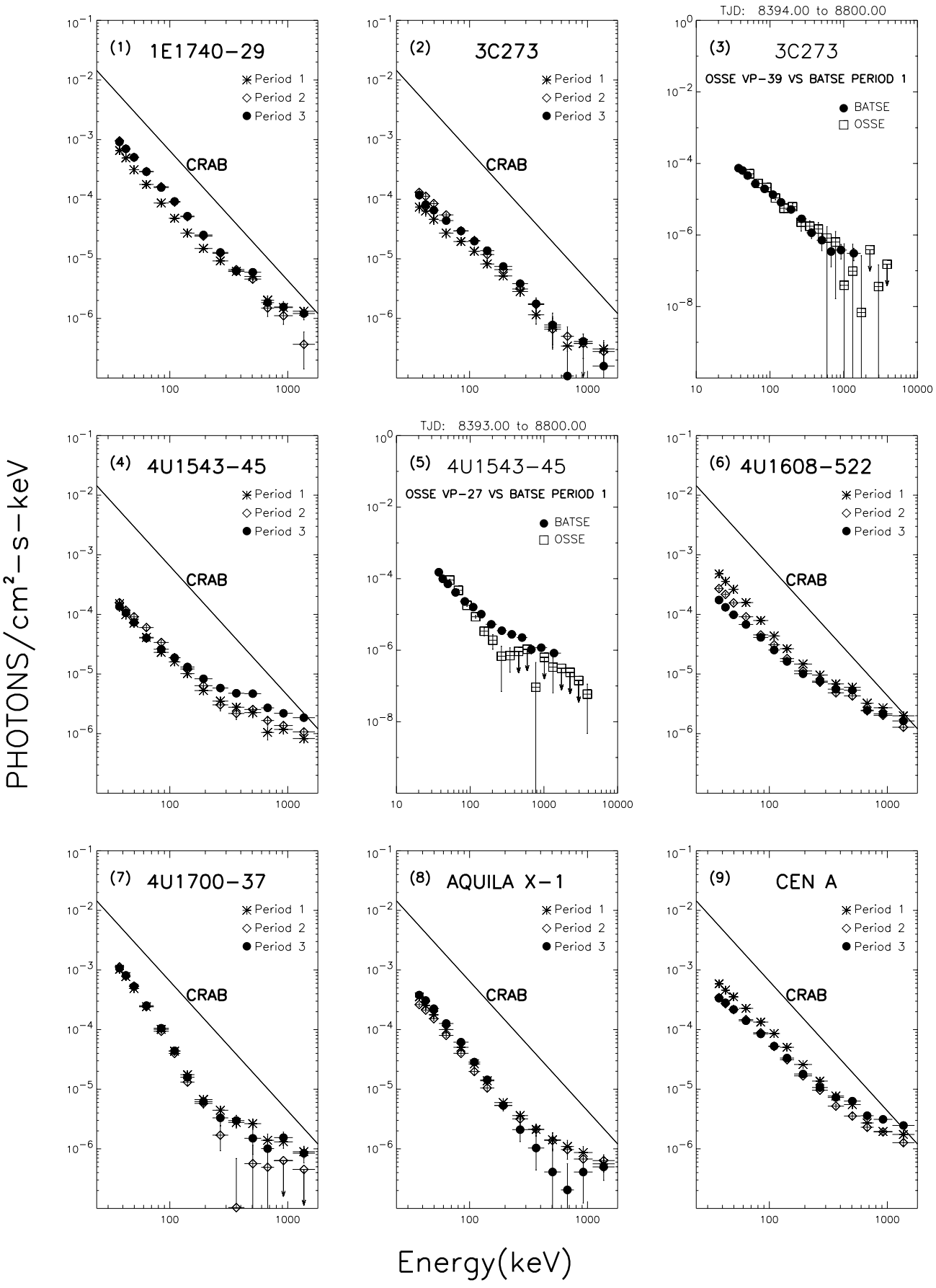

FIG. 8.—Spectral plots corresponding to the fluxes shown in Table 3. See § 2.4.4 for a discussion of the error bars

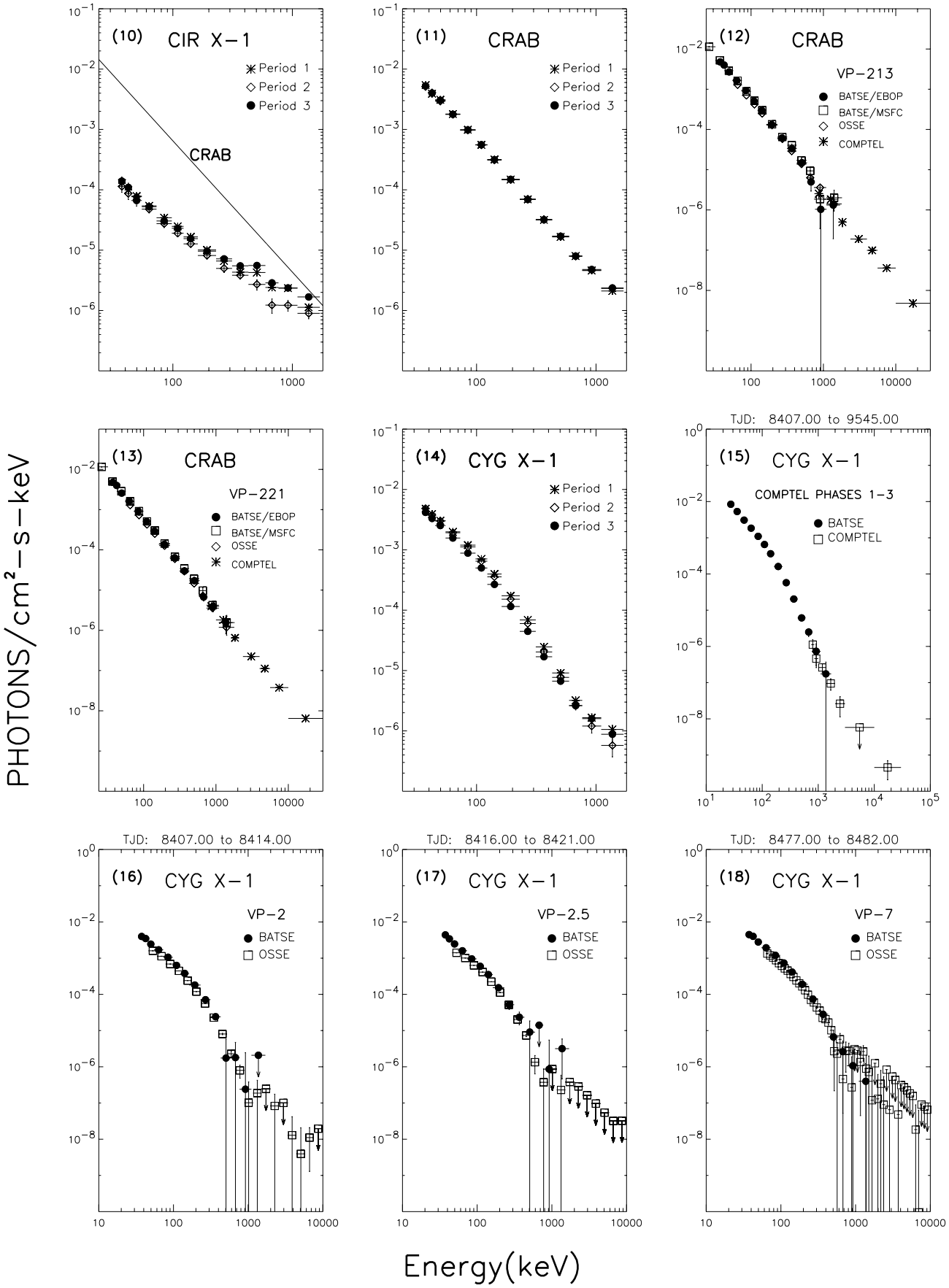

FIG. 8.—*Continued*

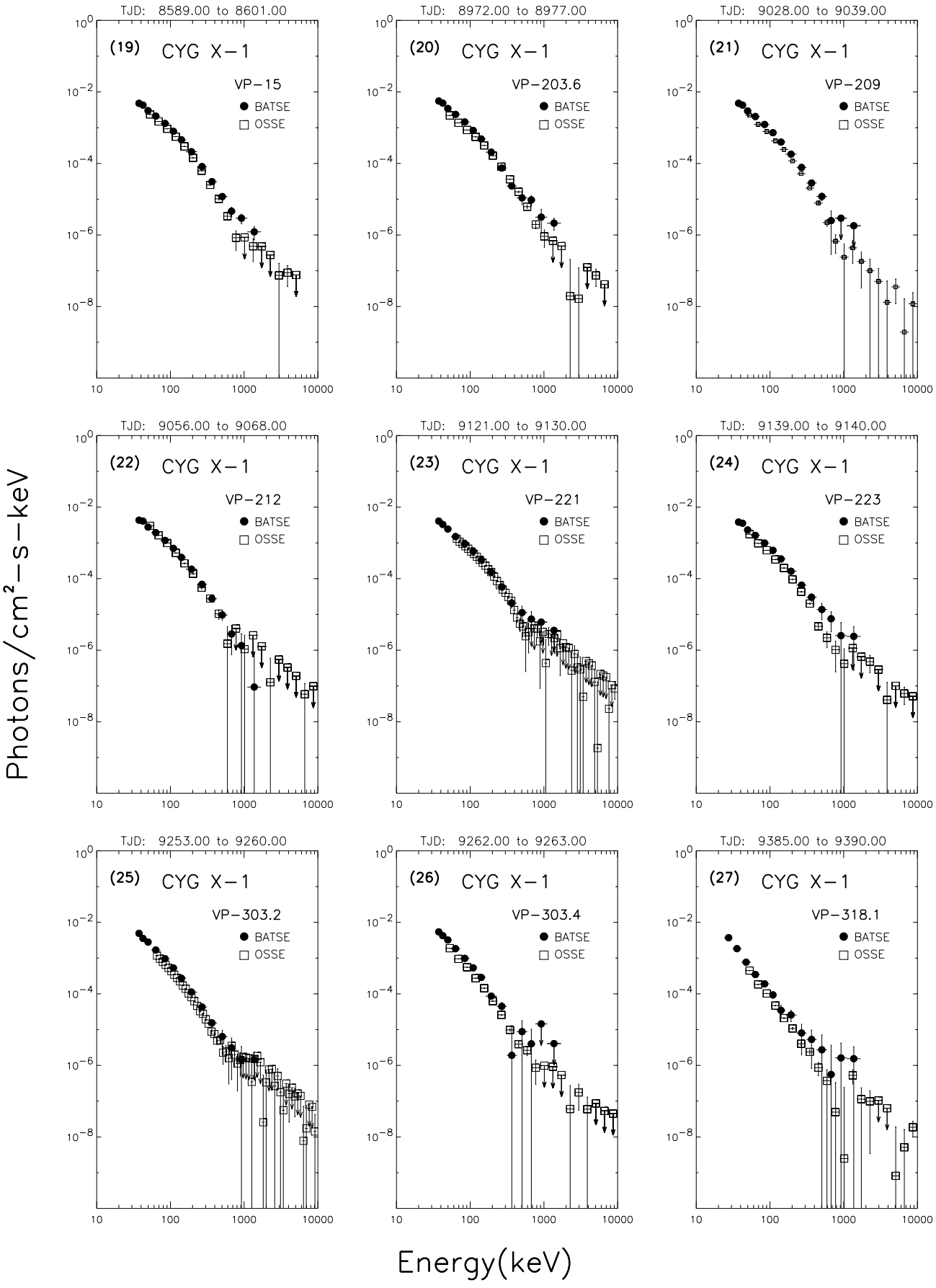

FIG. 8.—*Continued*

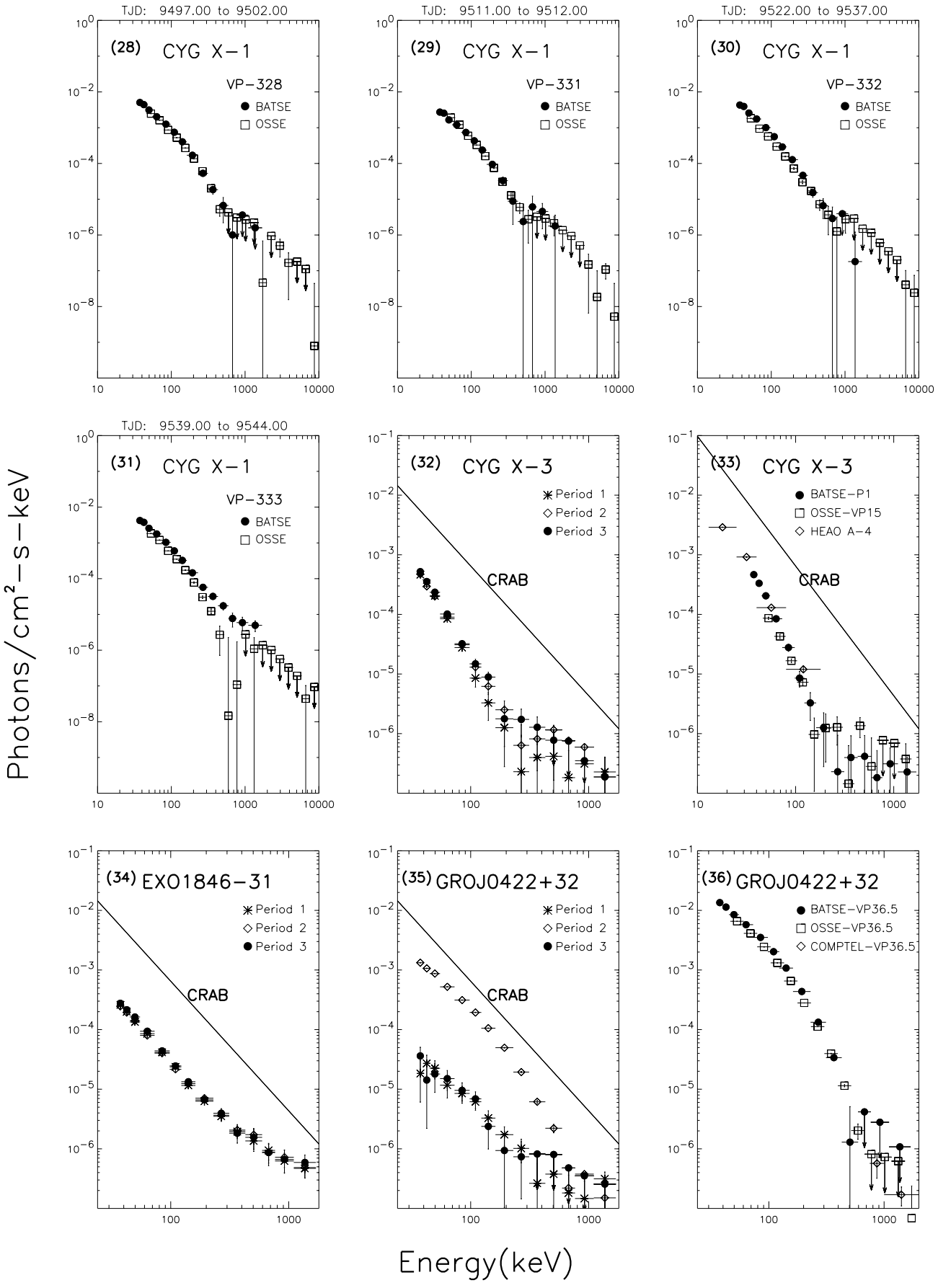

FIG. 8.—*Continued*

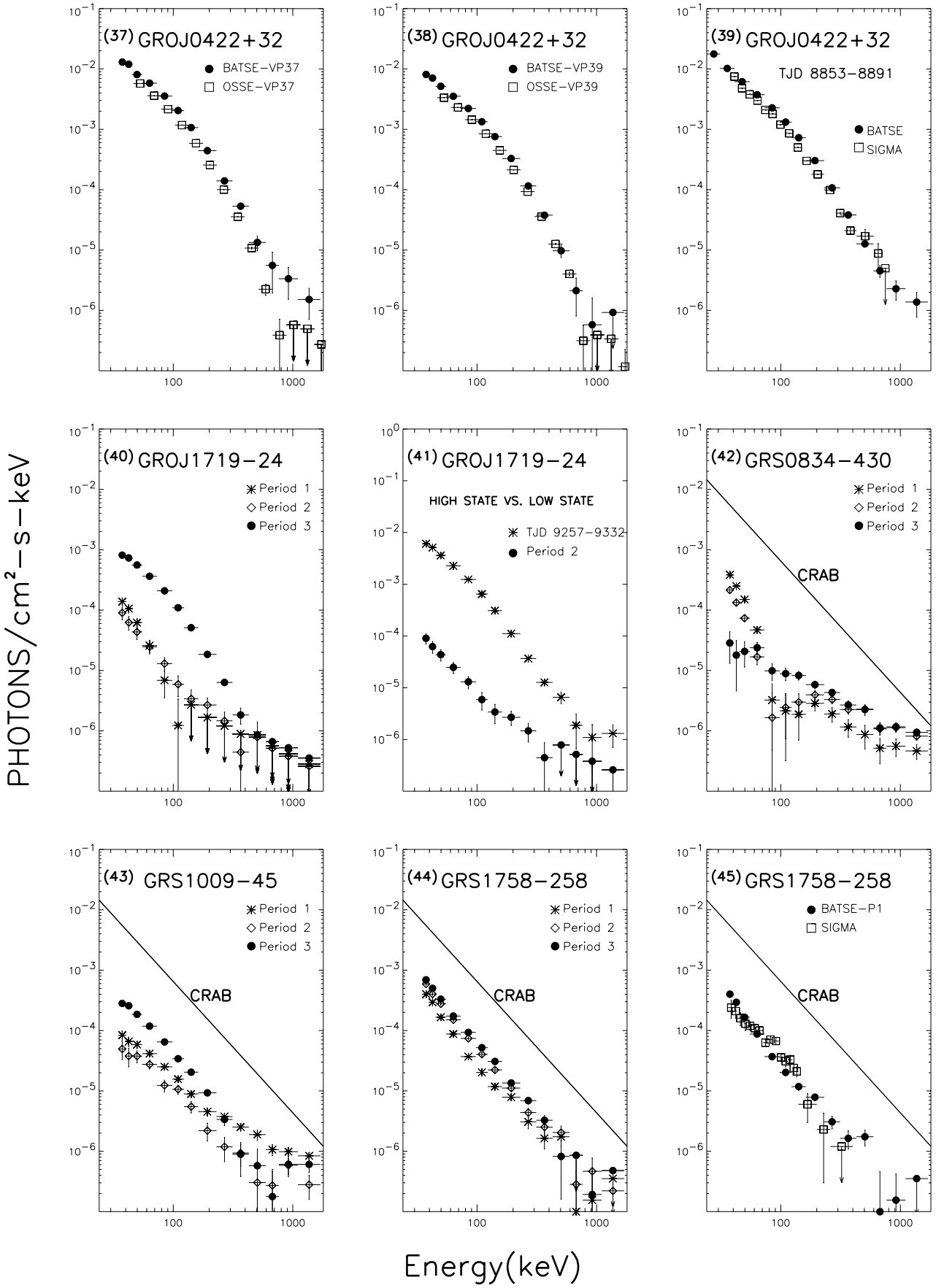

FIG. 8.—*Continued*

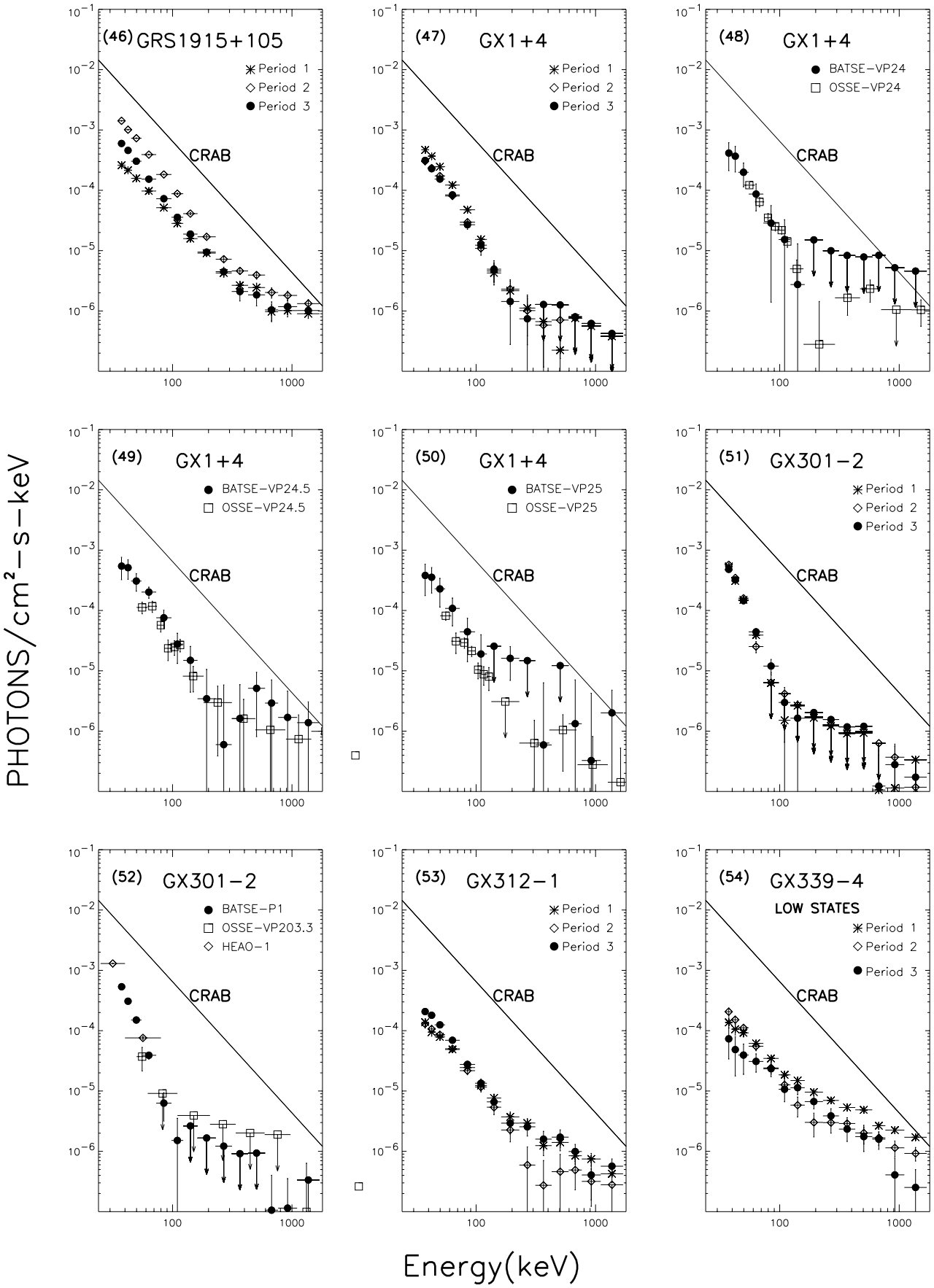

FIG. 8.—*Continued*

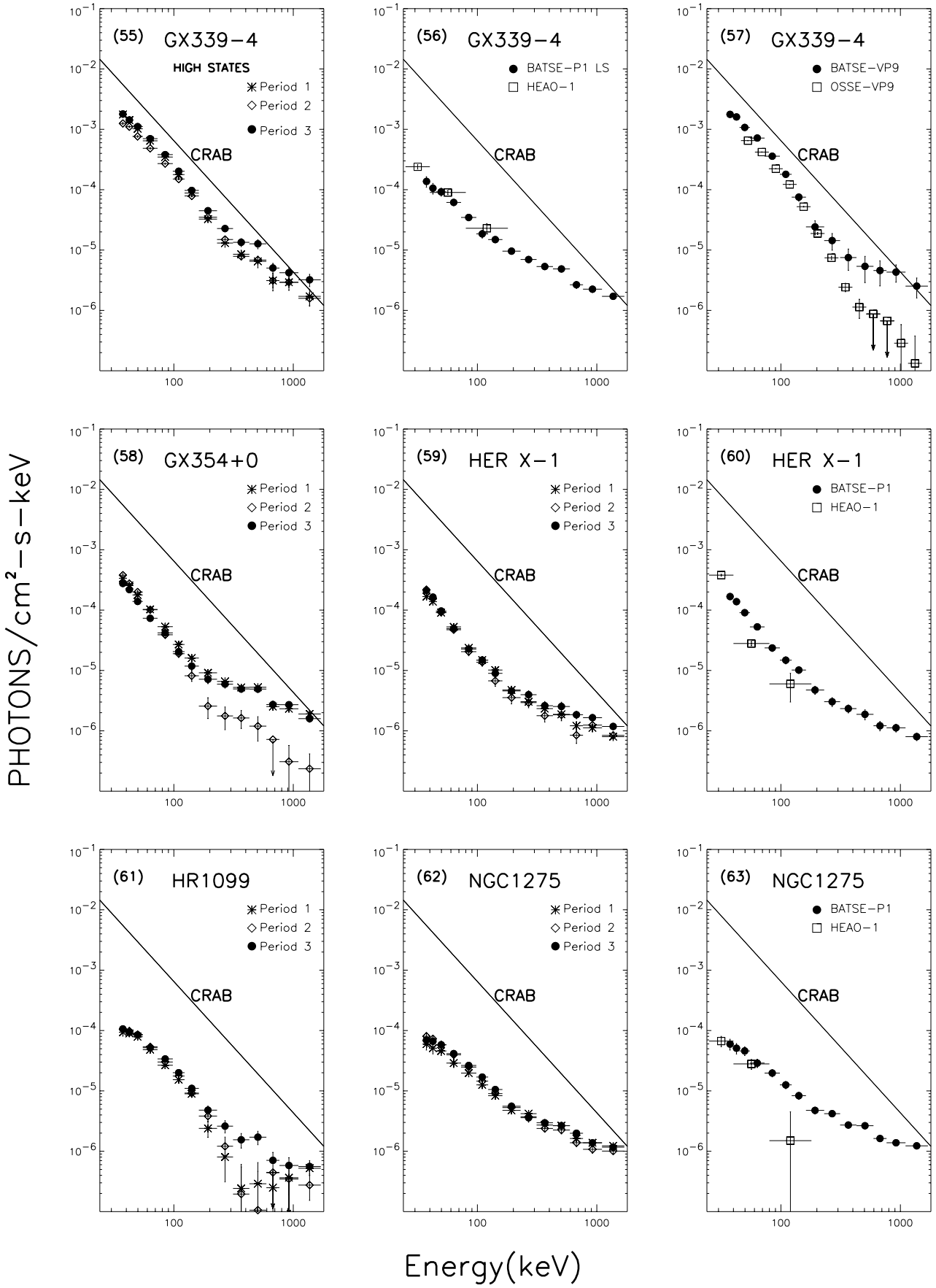

FIG. 8.—*Continued*

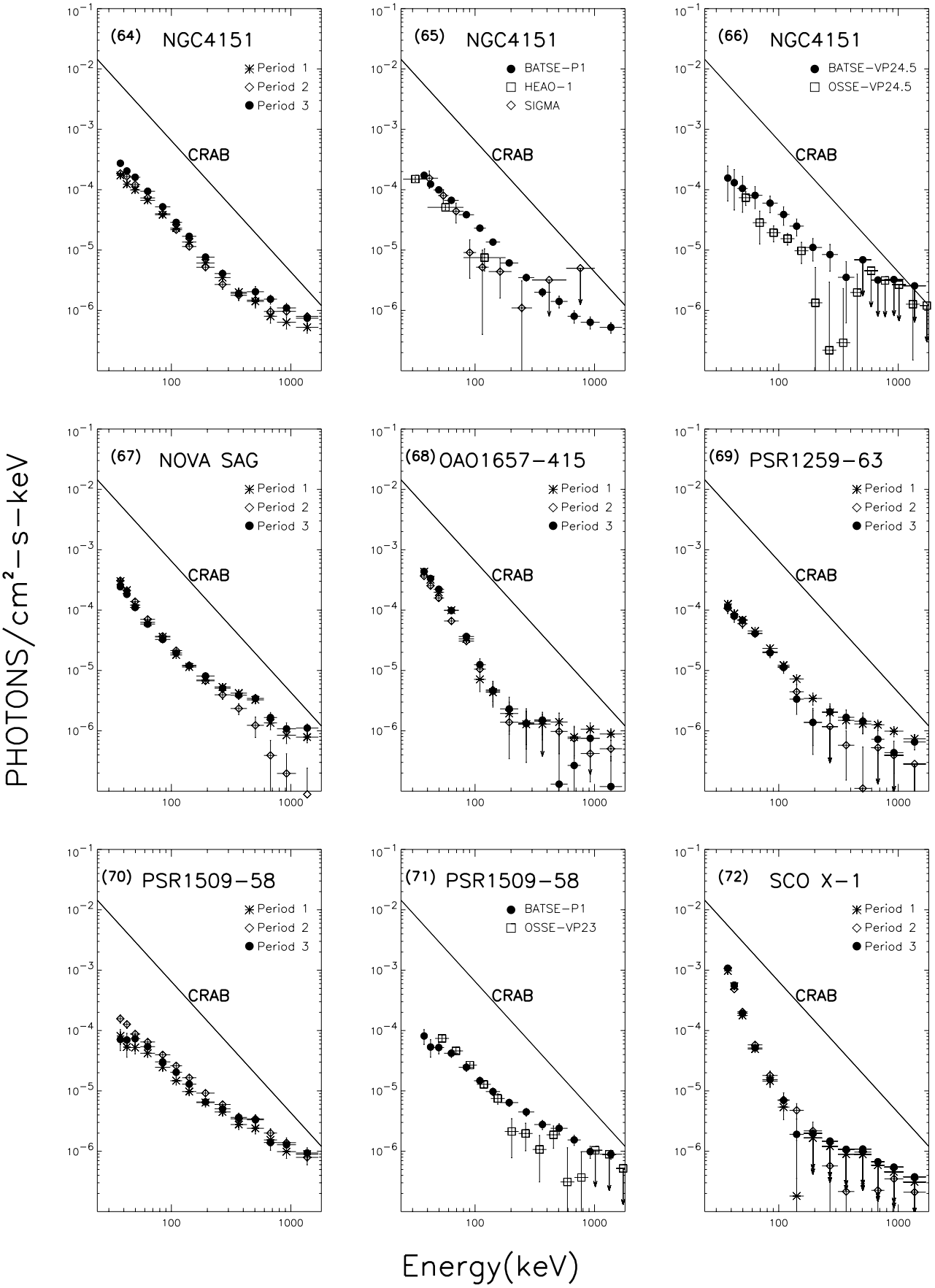

FIG. 8.—*Continued*

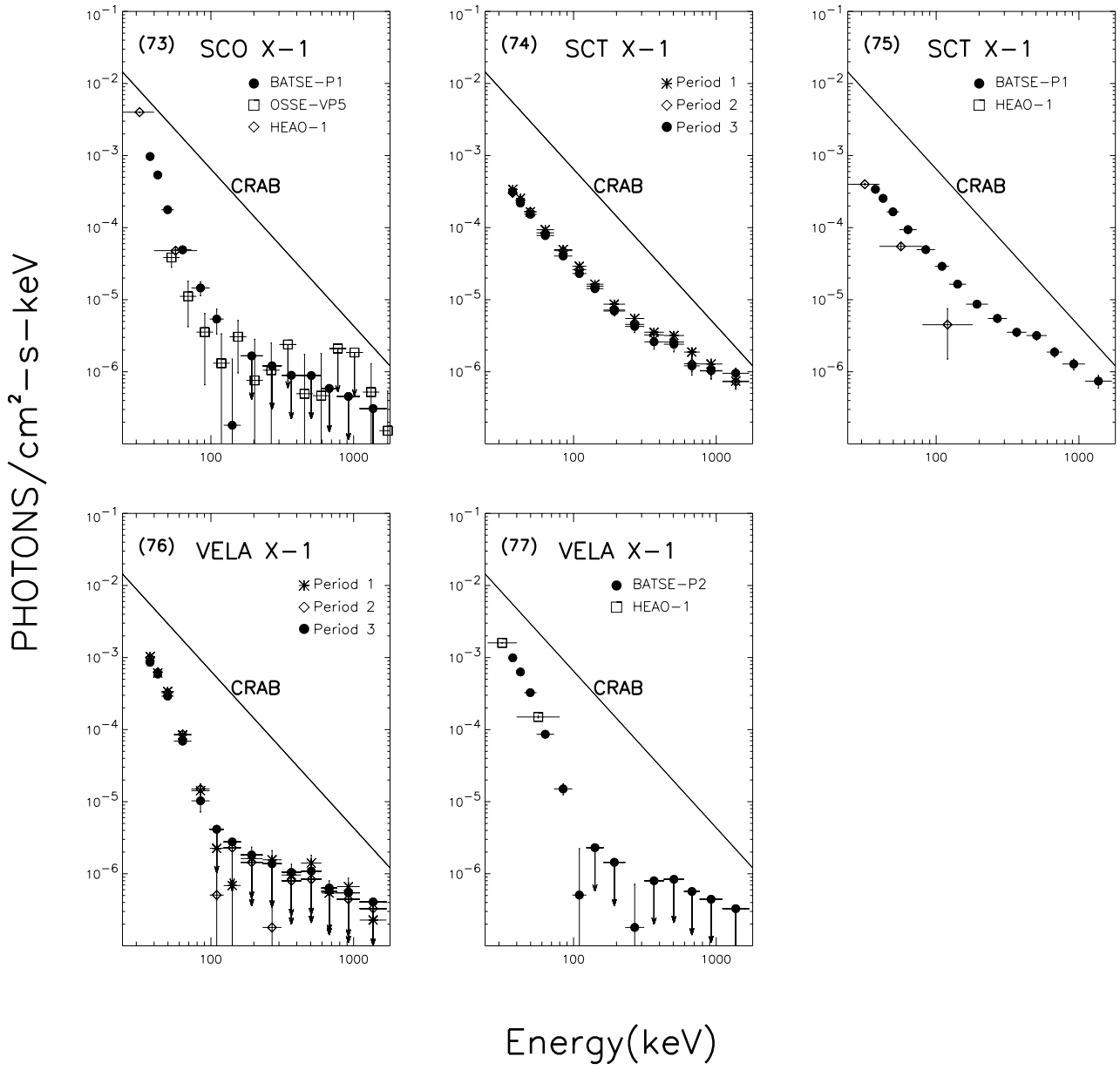

FIG. 8.—*Continued*

remaining seven direct comparisons, four on GRO J0422+32 (panels 36–39), two on GX 1+4 (panels 49–50) and one on GX 339−4 (panel 57), the most significant conflict is shown in the GX 339−4 spectra in regions above 200 keV measured by BATSE and OSSE during VP-9. The causes for the discrepancy are not known at this time.

Comparison of individual observations of OSSE and SIGMA, as well as *HEAO 1* A-4 with BATSE long-term averages is more difficult to interpret because of possible source variability. Overall, BATSE results agree well with most of *HEAO 1* A-4 and SIGMA spectra, as well as with most of the OSSE spectra. In summary, because of the long-term monitoring capability of a large number of sources which can only be occasionally seen by other experiments, BATSE results presented in this catalog provide an excellent cross check with simultaneous observations made by COMPTEL, OSSE, SIGMA, *XTE*, and *ASCA*.

5. SUMMARY

This catalog is the first of its kind in the history of this field for: (1) providing a comprehensive discussion of issues related to gamma-ray data analysis, and the EBOP methodology to deal with these issues, and (2) documenting the temporal and spectral information of gamma-ray sources (34) covering the period between 1991 May and 1994 October. The latter contains light curves of the 35–200 keV flux, with 1 day resolution, and time-averaged spectra in 14 energy channels, for each of the 34 moderately strong sources measured during this period. Daily count rates of 64 sources produced by EBOP, including 30 weak sources, in 16 energy channels and their Poisson and systematic errors for each of the eight LADS, for a total of ~150,000 spectra were archived at the COSSC in 1996. A more comprehensive 300 page catalog that contained three broad-band light curves, 35–200 keV, 200–500 keV and 500–1500 keV, respectively, and individual VP spectra, ~120 for each of the 34 sources, was also compiled and archived at COSSC in 1997. This catalog is a modified condensed version of the 1997 catalog. The primary objective of this catalog is to summarize such vast amount of information

into a single document that serves as a reference and guide for those using the EBOP database in pursuing a wide variety of research investigations.

This work was supported by a grant funded under the Compton Observatory Guest Investigator Program between 1991 and 1996. We congratulate Gerald Fishman and his BATSE team for conceiving, designing, and implementing such a simple and powerful experiment that has produced all the results included in this catalog. We wish to thank especially A. Harmon, Wm. Paciesas, and G. Pendleton of the P. I. team for their generous support throughout the years, C. Moustakas and B. Barris, undergraduate students at Caltech, for processing the data and producing the results shown in this catalog, and G. Case of U. C. Riverside for contributing to the BATSE data analysis program as part of his thesis investigation. T. Skelton and P. Wallyn participated in this program as National Research Council Resident Research Associates. The work described in this paper was carried out by the Jet Propulsion Laboratory, California Institute of Technology, under contract with the National Aeronautics and Space Administration.

REFERENCES

Arnaud, K. A. 1996, in ASP Conf. Proc. 101, Astronomical Data Analysis Software and Systems V, ed. G. Jacoby & J. Barnes (San Francisco: ASP), 17
Dixon, D. D., Kolaczyk, E. D., Samimi, J., & Saunders, M. A. 1997, in AIP Conf. Proc. 410, Fourth Compton Symposium, ed. C. Dermer, M. Strickman, & J. Kurfess (New York: AIP), 1601
Fichtel, C. E., et al. 1994, ApJS, 94, 551
Fishman, G. J., et al. 1989, in Proc. *Gamma Ray Observatory* Science Workshop, ed. W. Johnson (Greenbelt: GSFC), 2
Gruber, D. E., Jung, G. V., & Matteson, J. 1989, in High-Energy Radiation Background in Space, ed. A. Rester & J. Trombka (New York: AIP), 232
Harmon, B. A., et al. 1992, in The *Compton Observatory* Science Workshop, ed. C. Shrader, N. Gehrels, & B. Pennis (Greenbelt: GSFC), 69
Harmon, B. A., et al. 1996, A&AS, 120, 197
Levine, A. M., et al. 1984, ApJS, 54, 581
Ling, J. C., Mahoney, W. A., Wheaton, Wm. A., & Jacobson, A. S. 1987, ApJ, 321, L117
Ling, J. C., Wheaton, W. A., Mahoney, W. A., Skelton, R. T., Radocinski, R. G., & Wallyn, P. 1996, A&AS, 120, 677
Ling, J. C., et al. 1997, ApJ, 484, 375
Macomb, D. J., & Gehrels, N. 1999, ApJS, 120, 335
Mahoney, W. A., Ling, J. C., & Jacobson, A. S. 1981, J. Geophys. Res., 86, 11098
Mahoney, W. A., Ling, J. C., Wheaton, W. A., & Jacobson, A. S. 1984, ApJ, 286, 578
McConnell, M., et al. 1997, in AIP Conf. Proc. 410, Fourth Compton Symposium, ed. C. Dermer, M. Strickman, & J. Kurfess (New York: AIP), 829
McConnell, M., et al. 1999, Proc. 26th Int. Cosmic Ray Conf. (Salt Lake City), 4, 119
Much, R., et al. 1995, A&A, 299, 435
Pendleton, G. N., et al. 1995, Nucl. Instrum. Methods, 364, 567
Philips, B. F., et al. 1996, ApJ, 465, 907
Press, W. H., Flannery, B. P., Teukolsky, S. A., & Vetterling, W. T. 1986, Numerical Recipes: The Art of Scientific Programming (New York: Cambridge Univ. Press)
Purcell, W. R., et al. 1996, A&AS, 120, 389
Roques, J. P., et al. 1994, ApJS, 92, 451
Schönfelder, V., et al. 1999, A&A, submitted
Skelton, R. T., Ling, J. C., Radocinski, R., & Wheaton, Wm. A. 1994, in AIP Conf. Proc. 304, Second Compton Symposium, ed. C. Fichtel, N. Gehrels, & J. Norris (New York: AIP), 758
Skibo, J. G., Ramaty, R., & Purcell, W. R. 1996, A&AS, 120, 403
Van Dijk, R., et al. 1995, A&A, 296, 33
Wheaton, Wm. A., et al. 1992, in AIP Conf. Proc. 254, Testing the AGN Paradigm, ed. S. Holt, S. Neff, & C. Urry (New York: AIP), 356
Wheaton, Wm. A., Dunklee, A. L., Jacobson, A. S., Ling, J. C., Mahoney, W. A., & Radocinski, R. G. 1995, ApJ, 438, 322
Wheaton, Wm. A., Jacobson, A. S., Ling, J. C., Mahoney, W. A., & Varnell, L. S. 1989, in High-Energy Radiation Background in Space, ed. A. Rester & J. Trombka (New York: AIP), 304
Wheaton, Wm. A., Ling, J. C., Mahoney, W. A., Radocinski, R. G., Skelton, R. T., & Wallyn, P. 1996, A&AS, 120, 545
Zhang, S. N., Fishman, G. J., Harmon, B. A., & Paciesas, W. S. 1993, Nature, 366, 245